UNIVERSITY OF OKLAHOMA

GRADUATE COLLEGE

Single-probe Single Cell Mass Spectrometry Studies: Investigation of Cell Heterogeneity and Quantification of Intracellular Small Molecules

A DISSERTATION

SUBMITTED TO THE GRADUATE FACULTY

in partial fulfillment of the requirements for the

Degree of

DOCTOR OF PHILOSOPHY

By

YUNPENG LAN

Norman, Oklahoma

2023

Single-probe Single Cell Mass Spectrometry Studies: Investigation of Cell Heterogeneity and Quantification of Intracellular Small Molecules

A DISSERTATION APPROVED FOR THE DEPARTMENT OF CHEMISTRY AND BIOCHEMISTRY

BY THE COMMITTEE CONSISTING OF

Dr. Zhibo Yang, Chair

Dr. Yihan Shao

Dr. Luca Fornelli

Dr. Chongle Pan

Dr. Yuchen Qiu

ACKNOWLEDGEMENTS

I extend my sincere appreciation to the those who have played important roles in both my life and research. I could not thank them more for their unstoppable love and help, and I cannot imagine how can I reach this step without them. I am deeply grateful for their contributions to my academic journey:

As a person, I would like to thank my parents for bringing me into this world and my families for their unconditional support. I am particularly thankful to my mother, who diligently worked to provide me with a happy childhood, shielding me from the challenges I faced as a child. Her teachings on discerning right from wrong have been instrumental in shaping my decision-making abilities. To my father, your unwavering support throughout my school years has endowed me with the courage to reach this significant milestone. Your perseverance in securing my admission to a reputable middle and high school (even I did not make it finally), despite my initial academic struggles, remains etched in my memory. Thank you, uncle, as my mom’s brother, it is not your duty to take care of me, but you still do so. I still remember I received the first birthday gift from you ever in my life. Even I broke those robots very fast (sorry about it), but you should know how important it is for a little boy to have a birthday gift. It was you who completed my life. My aunt, though we don’t know each other before you met my uncle, embraced me as part of her family, creating cherished memories with her culinary skills. Heartfelt thanks also go to my grandparents for their constant presence, providing care during my mother's busy times.

Special acknowledgment goes to Tra, whose understanding and kindness eased my transition to life in the United States. Your love has become an integral part of my life, and I am grateful for the bond we share. You aren't my family selected by born but you are my family selected by heart. Life makes us meet and love makes us together. To my parents and sister-in-law, your steadfast support has been instrumental in my journey, and I am indebted to you for standing by my side.

In my capacity as a researcher, I express gratitude to my principal investigator, committee members, colleagues, and collaborators, who have been instrumental in shaping my scientific journey. Dr. Yang, your guidance has been foundational, leading me into the realm of science and imparting invaluable research skills. The time and effort you invested in mentoring me have profoundly influenced the completion of my dissertation. Dr. Shao, your lab provided a conducive environment for learning coding, leading to my first publication—a significant milestone in my research career. Dr. Fornelli, your assistance during crucial moments and engaging conversations during late-night work sessions have been invaluable. Dr. Pan, thank you for your help during the python class. You taught me systematically about python which help me a lot for my research. Dr. Qiu, you are the greatest out of department member. You always asked meaningful questions and kept me on track. I know as a professor, you are busy. Sincerely, I really appreciate all of you for your time and effort.

I also extend my appreciation to those beyond my committee, such as Dr. Foster, whose assistance with CHEM 4033 and inspirational stories provided encouragement during challenging times. It is not your responsibility to manage everything, but you

still provided the best to help us. I really love your story which encouraged me during the hard times.

Finally, I express my gratitude to all colleagues and collaborators who contributed to the completion of this dissertation. Dr. McCall, your support in the infectious disease and soil studies has been instrumental in laying the foundation for my initial research and I am deeply grateful for your service on my committee over the past five years. Dr. Chen and Dr. Li, your substantial contributions to the subpopulation paper and support in other aspects of my research are sincerely appreciated. Tra, your collaborative efforts during late-night experiments were instrumental in the publication of our works. Songyuan, thank you for your assistance in applying to the OU graduate school and your support during my initial days in the US. Thanks to Zongkai for his expertise in instrument repair and skills in calibration, which significantly contributed to the timely completion of my experiments.

In conclusion, my deepest thanks to all who have, in various ways, played a role in my journey. Your collective influence has shaped me into the person I am today, and I am profoundly grateful for each contribution, whether acknowledged here or not.

TABLE OF CONTENTS

List of Tables

List of Figures

List of Abbreviations

Abbreviation	Meaning
MS	Mass spectrometry
MSA	Mass spectrometry analysis
SCMS	Single cell mass spectrometry
LC	Liquid chromatography
PC	Phosphatidylcholine
PBS	Phosphate buffer saline
FBS	Fetal bovine serum

Abstract

Studying cell heterogeneity can provide a deeper understanding of biological activities, but corresponding studies cannot be performed using traditional bulk analysis methods. The development of diverse single cell bioanalysis methods is in urgent need and of great significance. Mass spectrometry (MS) has been recognized as a powerful technique for bioanalysis for its high sensitivity, wide applicability, label-free detection, and capability for quantitative analysis. The paramount significance of single cell mass spectrometry (SCMS) techniques have been recognized, and they are becoming indispensable tools in fundamental research and studies of human diseases such as cancers and infectious disease. My studies consist of two major parts: (1) the development novel method to quantify nitric oxide (NO) using combined chemical reactions and SCMS techniques and (2) the investigation of cell heterogeneity using integrated bioinformatics tools and SCMS methods.

In Chapter one, we reviewed the development of single cell mass spectrometry (SCMS) field and summarized multiple existing SCMS techniques. We also included the methods that have been used for quantitative studies of small molecules in single cells. In particular, we further developed the Single-probe, a microscale device that is ideally suited for SCMS study of live single cells under ambient environment, for molecular quantification in single cells. In Chapter two, the single-probe SCMS was coupled with chemical reactions to detect and quantify nitric oxide (NO) in single cells. We then performed detailed data analysis to study the subpopulations of cells based on their

NO expression levels. In Chapter three, cellular heterogeneity in infectious disease was revealed using the Single-probe SCMS, and we discovered the bystander effect of cells, which are uninfected cells adjacent to infected cells. In Chapter four, we developed a novel data analysis method for assessing the global metabolomic profiles from the SCMS experiments, allowing us to identify subpopulations and determine the number of subpopulations without prior knowledge. Finally, in Chapter five, a new machine learning method was applied to classify cells with different drug resistant levels.

Chapter 1: Single Cell Analysis

1.1 Single cell analysis methods

Limited by the sensitivity of instrument and sampling methods with relatively low spatial resolution in the past, so-called 'bulk analysis' has been the dominating method in the field of mass spectrometry (MS) for bioanalysis. However, traditional bulk analysis has several shortcomings that cannot be easily overlooked. First of all, the results of traditional bulk analysis methods are based upon the measurements of a population of cells, whereas cell heterogeneity, which plays an important role in biological activities and human diseases, is inevitably concealed. Individual responses from single cells might provide unique information that could revolutionize our current understanding. Moreover, bulk analysis methods tend to require a larger number of analytes, while certain samples (e.g., rare cells and limited patient samples) may not be easily obtained in a large quantity. Single-cell analysis, which enables studies on cell heterogeneity and reduces sample consumption, has become an emerging field in MS bioanalysis.

To study molecular changes (e.g., RNA/DNA, proteins, and metabolites) at single-cell level, many techniques, including DNA/RNA sequencing[1, 2], Raman spectroscopy[3, 4], flow cytometry,[5-8] and fluorescence optical microscopy[9-11], have been developed. DNA/RNA sequencing techniques are well established, and these methods have been further developed for single cell study because of their powerful amplification

technologies. Compared with DNA, the high variability of RNA in single cell due to its selective transcription could better represent cell activity, and therefore, single cell RNA sequencing has been widely used in single cell studies.[12, 13] Raman spectroscopy is a non-destructive label-free technique mainly focusing on interactions between cells and drug molecules as well as carrier systems and other nanomaterials.[3, 4] Flow cytometry utilizes fluorescence of antibodies on cell surfaces to characterize the cell population of interest.[5-7, 14] Fluorescence optical microscopy can be used to monitor cellular processes in single cells labeled with dye or fluorescent proteins such as GFP (green fluorescent protein).[9] However, applications of these techniques are largely limited by their intrinsic drawbacks: DNA/RNA sequencing provide genetic information but cannot directly reflect cellular activity; only specific components are Raman or fluorescence active, whereas the majority of cellular species cannot be directly detected.

MS is becoming a powerful bioanalytical method for untargeted analysis of biomolecules in single cells.[15] The wide coverage of different molecules of MS allows for a large amount of biological information to be obtained from a minimal quantify of samples.[16] Among different single cell MS (SCMS) methods, the vacuum-based techniques, including matrix-assisted laser desorption/ionization (MALDI) and secondary ion MS (SIMS), were first developed primarily due to their high spatial resolution for sampling.[17, 18] However, the requirement of high vacuum environment of sampling and ionization and complex sample preparation can limit their applications such as analysis of live cells.[19] With the development of novel sampling and ionization

methods, ambient-based SCMS techniques have been developed.[20] These methods allow for measurement of single cells in their near-native environment with little or no sample preparation.

SCMS analysis can provide broad coverages of molecules to acquire rich molecular information of single cells. Both qualitative and quantitative analyses are critical for better understanding of targets ranging from subcellular changes to biological systems. All SCMS methods are capable of qualitative analysis to obtain molecular compositions, and most of them can be used as semi-quantitative analysis methods to acquire the relative abundances of substances in single cells.[16, 19, 21, 22] However, only a few techniques have been established for quantitative analysis, i.e., to quantify the absolute amounts or concentrations of molecules of interest at cellular level.

Compared with traditional quantitative studies using bulk samples, such as lysates prepared from populations of cells and tissues[23-25], a major limitation of single cell quantitative analysis is the extremely small amounts of analytes in individual cells, and molecules with very low abundances may not be differentiated from background signal or noise detected for confident identification.[26, 27] Other common challenges in SCMS measurements include matrix effect, sample loss, molecular identification, and instrument fluctuation.[26, 27] In this chapter, we first briefly summarize multiple existing SCMS methods, and then focus on methods allowing for quantitative analysis of small molecules.

1.2 Single cell mass spectrometry

1.2.1 Vacuum-based techniques

Ionization is important as it is the first step to convert analytes into ions for MS analysis. Vacuum-based MS methods generally provide high sensitivity and high spatial resolution, making them to be naturally considered for single cell analysis. The SCMS technology development in this category started with secondary ion mass spectrometry (SIMS), followed by matrix-assisted laser desorption/ionization (MALDI), and lastly matrix-free laser desorption/ionization (LDI).

1.2.1.1 Secondary ion mass spectrometry (SIMS)

The first reported SIMS experiment was performed by Herzog and Biehböck in 1949[28], and this technique was further developed for single cell analysis in 1960s[29-31]. SIMS allows for sensitive surface composition analysis by sputtering surface analytes with a focused primary ion beam (e.g., $^{16}O^-$, $^{16}O^{2+}$, $^{40}Ar^+$, Xe^+, SF^{5+}, and Cs^+) to generate secondary ions from surface molecules. These techniques generally provide superior spatial resolution (e.g., nanoSIMS can reach a spatial resolution as high as 50 nm[32]). However, there are several major disadvantages of analyzing small biological samples (e.g., single cells) using these methods. First, the vacuum needed for the instruments is very high (e.g., ~1.9×10^{-9} mbar), requiring powerful pumping systems and careful sample preparation. Because the primary ion beam can also collide with gaseous molecules present between the primary ion source and the surface sample, the produced interfering ions can affect the analysis of cellular

species.[33] In addition, extra care is needed during sample preparation and measurement because the surface of analytes could absorb gas particles during these processes.[21] Second, conventional SIMS ion beams have relatively low ionization efficiencies of biomolecules (e.g., a typical ionization efficiency of 10^{-4}), which aggravate challenges of analyzing single cells.[34, 35] Third, as a hard ionization method, analytes undergo bombardment by high-energy ion beam, resulting in large numbers of fragments that are challenging for data analysis.[35, 36] The chemical damage decreased as atoms in the primary beam carried a smaller share of the incident kinetic energy, leading to the development of a new ion beam known as gas cluster ion beam.[35, 37] In this chapter, we mainly focus on the discussion of two well-established methods, time-of-flight (TOF)-SIMS[21, 34, 38-41] and Nanoscale SIMS (Nanoscale SIMS)[32, 42, 43], and one new technique, gas cluster ion beam secondary ion mass spectrometry (GCIB-SIMS)[37], that have been applied for single cell analysis.

I. TOF-SIMS

TOF-SIMS couples pulsed primary ion beam with a TOF analyzer, which detects ions based on their difference of drift time in field-free region. The utilization of the TOF analyzer enables the analysis of the precursor ions and their fragments at the same time, allowing for better identification abilities and enhanced mass coverage compared with conventional SIMS methods using other types of mass analyzers such as ion microscope analyzer and quadrupole.[15, 17, 44]

TOF-SIMS has been applied to various mass spectrometry imaging (MSI) studies of a broad range of species (e.g., lipids[40, 45, 46], metal ions[47, 48], and metabolites[49]) with

spatial resolutions high enough for SCMS experiments (e.g., as high as 100 nm). MSI can provide spatial distributions of molecules in 2D, and 3D space. Currently, there are two strategies for MSI studies to obtain 3D information: microtomy and ablation. Microtomy has been widely used in nearly all MSI methods to prepare tissue samples.[46, 50, 51] In 3D MSI studies, samples are embedded in a supporting medium, such as nitrocellulose in freezing temperature (~ -20℃).

and sliced into micrometers size films (6-20 um). Multiple 2D MS images from consecutive slices are used to obtain 3D contribution. In single cell studies, microtomy has also been applied to slicing mouse germinal vesicle (GV) oocyte cells into successive section stacks (with 2 μm in thickness), which were then used to reconstruct 3D single cell MS images, as demonstrated by Pogorelov et al.[52] Ablation does not require slicing samples, so this technique not only reduces the sample treatments, but provides a very crucial advantage to handle samples in small sizes such as single cells.[39, 41, 53] Ablation is a combination of dynamic and static SIMS. Dynamic SIMS uses a higher dose of primary ions (sputter beam) to remove several top monolayers of the sample surface, whereas static SIMS utilizes a secondary ion beam (analytical beam) to sputter only the topmost atomic layer.[21] Molecules on sample surface are desorbed and ionized by analytical beam, then a thin layer on the surface is ablated by sputter beam automatically. The ablation depth need to be measured since the ablating efficiency varies and is influenced by surface temperature.[21] Atomic force microscopy (AFM) , scanning electron microscopy (SEM),[38, 54, 55] and multilayer Irganox standard samples[56-58] has been applied to

measuring the ablating efficiencies (depth of each time of ablation). Single cell 3D-MSI-TOF-SIMS has been used in many different studies such as chemotherapeutic drug delivery (Fernandez-Lima et al)[41] and proteins and lipids (Chen et al).[39] However, the depth resolution of ablation methods is normally better than microtomy methods since microtomy depth resolution is limited by the sectioning methods.[22]

II. Nano-SIMS

NanoSIMS provides further improved spatial resolution (e.g., as high as 50 nm) for the detection of elemental and isotopic composition in samples. Although the fundamental principles of nanoSIMS and conventional SIMS techniques are similar, the major differences between them arise from the primary ion beam and mass detector. NanoSIMS usually uses a continuous primary ion beam with the most electropositive (Cs^+ for negative ion mode) or electronegative (O^- or O^{2-} for positive ion mode) to achieve the highest ionization efficiencies. Different from TOF-SIMS, nanoSIMS is equipped with magnetic sector mass analyzer. A high lateral resolution (e.g., as high as 50 nm) can be achieved due to the combination of multiple factors, including the type of primary ion source, optimized ion beam optics, and specially designed mass analyzer.[59] NanoSIMS has become an indispensable tool for analyzing biomaterials and biological samples requiring ultra-high spatial resolution (e.g., sub-cellular) as discussed in recent reviews.[32, 42, 43, 60-63]

III. GCIB-SIMS

Although most SIMS-based techniques are well-known for high spatial resolution but a low mass range (< m/z 1000) measurements, a new generation of ion beam

source, GCIB (gas cluster ion beam), has been developed to shift their capabilities from fragment detection to molecular profiling.[35] The clusters ions in GCIB-SIMS instruments are created through a supersonic expansion where high pressure gas (~10^6 psi; most likely noble gases such as helium or argon) expands and cools in a vacuum (~1 psi).[37] This type of new ion beam sources significantly improved the ionization efficiency and expanded mass range because of the relatively large size and low energy of the clusters, allowing for study of relatively large biomolecules, such as lipids and fatty acid, from single cells with high spatial resolutions (1μm).[35, 45, 64] However, comparing with traditional SIMS, GCIB-SIMS has relatively low spatial resolutions and it is not commercially available for all users.

1.2.1.2 Laser desorption/ionization

Laser desorption/ionization (LDI)-based MS methods use a laser beam at certain wavelength to illuminate on sample surface where certain molecules are desorbed and ionized. After the first laser machine has been developed in 1960 by Maiman, LDI was observed by Honig and Woolston in 1963 that the laser induced emission of different types of charged particles, such as electrons and ions, and neutral atoms from different solid surfaces.[65] However, this technique had not been widely used until the 1980s due to the limited coverage of types of molecules that could be ionized. The energy from the laser beam with certain wavelength can only be absorbed by specific molecules. The major LDI-based techniques include matrix assisted laser desorption/ionization mass spectrometry (MALDI-MS) and matrix-free LDI methods.

I. MALDI-MS.

MALDI-MS was developed in the 1980s. This strategy significantly increased the ionization of larger biomolecules (up to 100k Da) such as proteins and polymers.[66, 67] The application of matrix, usually organic compounds with strong UV absorption, enables efficient absorption of the laser energy and ionization of the applied matrix molecules. The ionized matrix molecules transfer the energy to the analyte molecules for desorption, and the ionization of analytes occurs through interactions with ionized matrix molecules.[68] MALDI-MS measurements generally render high spatial resolutions, providing a great potential for subcellular analysis as reported as early as 1990s.[69-71] High vacuum environment is required for MALDI to avoid the interference of the laser and atmosphere when the laser ionization technique was developed.[17]

However, the pretreatments by matrix and requirement of high-vacuum working environment always draw concern about the alternation of the sample (e.g., delocalization of molecules). In addition, traditional matrix molecules commonly induce interferences with the detection of low-molecular weight compounds (<1,000 m/z), limiting studies of small molecules such as metabolites and drug compounds.[72-74] Atmospheric pressure (AP) MALDI-MS, in which desorption and ionization occur at ambient environment, can simplify the sample pretreatment procedures and increase experiment throughput.[75]

This first MALDI-MS experiment used a 266 nm laser to analyze a mixture of alanine and tryptophan.[76] Then, a variety of different matrices have been developed for detection of different type of analytes. For example, as a popular matrix, α-cyano-4-hydroxycinnamic acid (CHCA)[73] performs well at 337 or 355 nm wavelength for

analyses of peptides, nucleotides, and lipids. Due to its excellent capability of spatially-resolved analysis, MALDI has become one of the most popular ion sources in MSI studies, including at the single-cell level. Based on the nature of different species of interest, detailed procedures of sample preparation for MALDI-MSI experiments may vary, but tissue sectioning and matrix application are generally required prior.[77] With different types of matrix molecules, the coverage of MALDI-MS can be optimized to cover lipids[77, 78], peptides[79], proteins[80], or even polymers[81]. MALDI-MS has become one of the most commonly used in tissue imaging and single cell analysis[78] and was commercialized for general subcellular studies. The quantitative studies on single cells using MALDI-MS are reviewed in the next section.

To date, although most commercial MALDI–MSI instruments enable analysis of samples with reasonably high spatial resolutions (e.g., pixel sizes ranging between 5 and 20 μm), the ion yields are $<10^{-6}$ for many types of analytes[82, 83], limiting their abilities for single cell analysis. Numerous efforts have been devoted to improving the spatial resolution and ionization efficiency, while suppressing matrix interference, to promote single cell studies. The laser-induced post-ionization (MALDI-2) utilizes two pulsed lasers: one for analyte desorption and the other for ionization in the expanding particle plum. MALDI-2 greatly enhanced the ion yields for biomolecules such as lipids and metabolites. Combined with transmission mode (t-) of laser desorption, the t-MALDI-2 technique achieved a small pixel size of 600 nm.[84]

The selection of suitable matrix compounds is crucial for a successful MALDI experiment. Even though numerous efforts have been made to search for matrix

molecules with minimal interference at low m/z range, there is no report of perfect matrix with clean background that can cover the whole mass range. To minimize undesired matrix interference, different strategies have been adopted. First, inorganic materials, including nano cobalt oxide, carbon nanotubes, gold and silver nanoparticles, graphene, and nanostructure-based surfaces, were adopted in place of traditional organic matrices. Second, functionalized surfaces and substrates have been used to replace matrices. For example, self-assembled surfaces (SAMs) have highly organized, reproducible surfaces, where the samples are pretreated with a cationic solution without using any solid matrix.[85] Another approach to surface modification is achieved by desorption ionization on porous silicon (DIOS), introduced by the Siuzdak group in 1999, that can be used for analyte deposition during sample preparation.[86] Many other methods, such as using sol-gels and polymer coatings, have also been developed to modify the surface for sample loading.[87, 88]

II. Matrix-free laser desorption/ionization (LDI)

To eliminate the interference of matrix molecules, matrix-free laser desorption/ionization mass spectrometry (LDI-MS)[89, 90] and label-assisted laser desorption/ionization mass spectrometry (LALDI-MS)[91, 92] have been developed.[74] These techniques have been used for MS studies of relatively large cells such as plant[93] and algae cells[94].

In the LALDI experiments, target molecules (e.g., peptides) need to be labeled with certain functional groups (e.g., fluorophores or polyaromatic) for desorption and ionization by soft lasers with visible wavelengths. Although some of these LDI

approaches are claimed as matrix-free, it is rare for them to completely avoid using any intermediate to analyze biological samples, primarily because of the complexity of biomolecules that require different levels of desorption and ionization energy.[74] In fact, in previous experiments without using any intermediate, such analysis of unicellular microalgae by Pohnert et al.[95] and studies of genus Hypericum by Svatos et al.[93], the molecular coverages are generally lower than MALDI. Hence, an ideal material for universal coverage has not yet been reported.

1.2.2 Ambient techniques

Although the above vacuum-based MS techniques have been well demonstrated for single cell studies, alternation of sample environment, such as matrix application and requirements of high-vacuum, can alter metabolomic profiles of cells compared with those in their living status. To overcome these challenges, numerous ambient SCMS techniques have been designed. Compared with vacuum-based techniques, most ambient-based techniques require less or even no sample preparation, allowing for preservation or minimized alteration of the cell environment. However, in exchange for the simplified sample preparation process, additional time is often needed for single cell sampling; therefore, most ambient-based techniques generally have relatively lower throughput compared with vacuum-based methods. Most of these ambient SCMS techniques generally use physical probes, laser, or charged solvent droplets for analyte sampling and ionization.

1.2.2.1 Probe-based methods

I. Direct probe suction

Since the size of a single cell can be as small as micrometer scale, it is challenging to use regular sampling and preparation methods adopted in bulk analysis. Microprobes stratified the requirements of single cell analysis.

The idea of microprobe was first proposed by Masujima in 1999,[96] whereas the first SCMS experiment was successfully carried out using live single-cell video mass spectrometry (live single-cell MS or Video-MS) in 2008.[97] In their studies, cells were monitored by a video-microscope, and the tip (1-2 μm) of a gold-coated capillary nano-ESI emitter was used as a micropipette for sucking the cell contents (cytoplasm or organelle). The nanoESI emitter was then used as an ion source for MS analysis. The results showed the specific peaks of cytoplasm, organelle, cell culture medium, and solvent could be distinguished through statistical analysis (t-test). Later, Masujima applied the technique to study plant cells, and they also improved the coverage for larger molecules, such as lipids, by sonicating the tips containing single cell.[20, 98, 99] In 2016, the same group reported quantitative analysis using the live single-cell mass spectrometry.[100] To further improve this technique, many efforts have been made such as coupling it with fluorescence imaging[101], laser microscopy[100], and micro-droplet array device[102].

Single cell sampling can be achieved through capillarity, by which cellular contents can be spontaneously drawn into capillaries without a suction force provided by a pump. Vertes' group reported capillary micro-sampling system coupled with ion mobility MS detection for single cell analysis.[103] A glass capillary was pulled to form a sharp tip (~1um), and the tip was inserted into the plant cells. Due to the capillary

action and turgor pressure, the cytoplasm automatically entered the glass capillary. After suction of cellular contents, the capillary was backfilled with 1 μL electrospray solution, and a platinum wire was inserted from the back to contact the electrospray solution. During the MS analysis, an ionization voltage (2 kV) was applied on the platinum wire to induce nanoESI. About 200 peaks were found in the mass spectra, and the application of ion mobility led to resolving 400 different ions from these peaks. Significant differences have been found between trichome and the other two types of cells, but not between pavement and basal cells. In 2015, 22 metabolites and 54 lipids were identified by the same group from human hepatocytes (HepG2/C3A) using similar techniques.[104] In 2018, they also measured peptides in single neurons of the mollusk Lymnaea stagnalis.[105] Cytoplasm and nucleus were separately analyzed by coupling the capillary micro-sampling system with fluorescence microscopy.

Nonami's group introduced cell pressure probe.[106-108] To reduce the sample preparation time, they modified the previous cell pressure probe[109-111] to enable direct injection via the ESI source of a Orbitrap mass spectrometer.[108] Briefly, a high voltage was applied from a metal wire coiled around the capillary tip or an inserted internal wire electrode from the back of the ESI emitter.

More methods have been developed based on similar concepts. For example, micropipette needle, which is a multifunctional device, was developed by the Yang group for SCMS studies.[112] As a sampling device, the micropipette needle is large enough (~15 μm tip size) to extract an intact cell, instead of inserting into a single cell, for sampling single cells. The micropipette needle was also used as the container for

cell lysis (by organic solvents such as acetone and acetonitrile) and Paternò–Büchi (PB) reaction (assisted by UV irradiation) to determine the double-bond position in unsaturated lipids (through analyses of diagnostic MS^2 fragments) at the single-cell level.

The T-probe is another device developed by the Yang group in 2018 for direct suction of contents from single cells for MS studies.[113, 114] In a T-probe, three fused silica capillaries (i.e., solvent-providing capillary, nanoESI emitter, and cell probe) sandwiched by two polycarbonate slides to join together at a T-shaped junction. The solvent is provided through one horizontal channel (liquid providing capillary) and flows towards the other horizontal channel (nanoESI emitter). Unlike other probes for direct suction using mechanical devices, such as a syringe or microinjector, to withdraw analytes from single cells, the T-probe takes advantages of the self-aspiration in nanoESI processes. During the SCMS experiment, ESI induces liquid displacement inside the nanoESI emitter and further generates a suction force in the cell probe, which is inserted into a cell. Cellular contents are extracted by the cell probe, mixed with the solvent from the solvent-providing capillary, and then immediately delivered to the nanoESI emitter for MS analysis.

II. Probe microextraction by solid or liquid phases

In addition to direct, non-separative extraction of cellular contents, microscale extraction can be performed through solid or liquid phases within the device to selectively extract or preconcentrate analytes of interest from the original cellular contents. In these processes, the extraction phase absorbs or dissolves the analytes

during sampling processes. Due to the small sample size for single cell analysis, microextraction needs to be performed using a lower phase ratio of extractant to sample.[115] In SCMS studies, microextraction is operated using modified tips or MS compatible solvents, and experiments are conducted under ambient and open-air conditions.

There are two microextraction-based methods reported in previous studies: solid-phase microextraction (SPME)[116] and liquid-liquid microextraction (LLME)[117]. SPME utilizes a solid needle as the extractant to insert into a single cell, while LLME utilizes organic solvents, such as methanol or acetonitrile, for extraction in ambient conditions. LLME methods usually have no requirement of another solvent for MS analysis, thus tend to have a higher throughput compared with SPME. More detailed explanation for SPME-AMS have been provided in Reyes-Garces' paper.[118]

The sampling process of the SPME based single cell ambient MS (SPME-SC-AMS) is operated by inserting a needle in a single cell to absorb cellular contents onto needle surface. Since molecules in the solvent interacts with the solid sorbent on the probe during SPME-SC-AMS, i.e., selective partitioning between a solid sorbent and a liquid sample, the molecules in single cell are absorbed by the probe for the further MS analysis. However, the extraction efficiency is a primary concern for SPME-SC-AMS. In order to enhance the extraction efficiency, tips were modified or coated with different materials, which could play a significant role in analysis. During MS analysis, the absorbed cellular analytes are released and ionized thought two different strategies. In the first strategy, the absorbed analytes need to be redissolved by

dipping the tips inside an organic solvent, which is then ionized for MS analysis. This concept was first introduced by Hiraoka et al. in 2012. Luan et al. modified this technique by using coated probes, surface-coated probe nanoelectrospray ionization MS (SCP-nanoESI-MS), to enhance the extraction efficiency in studies reported 2014 and 2015.[119-121] Specifically, a tungsten microdissecting needles (~1 μm tip size) coated with silanization (*n*-Octadecyldimethyl[3-(trimethoxysilyl)propyl]ammonium chloride) was inserted into single cell, aiming to enhance the adsorption of cellular contents. The probe was then inserted into a nanoESI emitter, which was preloaded with desorption/spray solvent (1 μL of methanol), for a short period of time (~30 s) to desorb extracted molecules. An ionization voltage was then applied on this nanoESI emitter for ionization and MS analysis. Quantitative analysis of perfluorinated compounds (PFCs) from single egg cells of Daphnia magna was performed using this technique. In the second strategy, the absorbed analytes are ionized with the assistance of solvent spray. As reported by Suzuki et al. in 2007, an ionization voltage was applied on the probe (a rust-free high-quality stainless-steel needle) upon finishing sampling a single cell, and the solvent (normally organic solvent) was then sprayed on the probe. With the assistance of the solvent and high voltage, analytes absorbed on the probe were ionized.[122] Similar desorption and ionization methods were used by the DSP, in which the auxiliary solvent droplets were generated by a piezoelectric inkjet system.[123] Many metabolites, including amino acids and flavonoids, in single plant cells were successfully analyzed using the DSP method. By reducing

the solvent volume and modifying tip surfaces differently, the throughput and sensitivity were further increased.[124]

In LLME-based SCMS studies, organic solvents, such as methanol and acetonitrile, were frequently used as extraction solutions for small molecules due to their ability to break cytomembrane and high extraction efficiency. The basic strategy is to provide a solvent, normally by capillary, for dissolution or extraction of single cell contents, then deliver the solution to mass spectrometers for subsequent analysis. Solvent choice and the way of solvent delivery can dramatically influence the extraction and MS profiling.

Nanospray desorption electrospray ionization (nano-DESI), which used a primary capillary for solvent delivery on sample and a secondary capillary for solution extraction and ionization, was introduced by the Laskin group in 2012 for MS tissue imaging.[125] A spatial resolution of 12 μm with high signal-to-noise ratio in each individual pixel was reached, enabling its functions for SCMS studies. In 2017, Lanekoff et al. detected amino acids and plasmalogens in single cheek cells with nano-DESI.[126]

Droplet-based microextraction was developed by the Zhang group in 2016, and this technique has been used to detect numerous metabolites, such as uridine diphosphate N-acetylglucosamine (UDP-Glc-NAc), glutathione(GSH), and adenosine monophosphates, from breast cancer cells.[127] In 2018, the same group further combined their droplet extraction technique with Pico-ESI-MS (pulsed direct current electrospray ionization mass spectrometry). Compared with nanoESI, the flow rate of

pico-ESI was dramatically reduced, leading to significantly increased ion signal duration (i.e., ~2 mins) and improved molecular identification (>300 phospholipids were identified) from single cells.[128]

In 2014, nanomanipulation-coupled nanospray MS was introduced by Phelps et al.[129] This method used one quartz probe to puncture the cell membrane, and then used a nanoESI emitter to extract analytes from the cell. Using the “two-tip” method can reduce the risk of tip clogging of the nanoESI emitter during cellular analytes extraction. In their studies, a Pd/Au-coated nanoESI emitter was pre-filled with 10 uL solution (chloroform:methonal (2:1, v/v) with 0.1% ammonium acetate). The solvent in the nanoESI emitter was injected into cells at a pressure of ~5 psi for 500 ms to extract analytes, such as triacylglycerol (TAG). The solution was drawn back at a pressure of ~20 psi, and the nanoESI emitter was then transferred to a mass spectrometer for analysis, with a focus on TAG difference between healthy and tumorous adipocytes. In 2015, Phelps et al. used this technique to expand the molecular coverage to cellular lipids.[129]

1.2.2.2 Desorption/ionization

The concept of desorption electrospray ionization (DESI) was introduced by the Cooks group in 2004, focusing on a direct surface analysis.[130] By spraying charged droplets generated by ESI onto the sample surface, molecules on the sample surface are desorbed and ionized in the atmosphere. DESI has been widely used in MSI of lipids[131] and proteins.[132] [133] With improved spatial resolution, this methods was first applied on single cell analysis in 2012 and revealed significant differences in the lipids

of mouse oocytes at different status (unfertilized oocytes, two- and eight-cell embryos).[134]

Lasers can also be a source of energy for the desorption/ionization of sample molecules. The first laser assisted ambient MS technique is laser ablation electrospray ionization (LAESI)[135], which was introduced by Nemes and Vertes in 2007. In this study, an etched optical fiber tip was used to transmit mid-IR laser pulses to sample for ablation. Desorbed molecules were intercepted by the electrospray and delivered to the mass spectrometer. In 2009, the first single cell application of LAESI-MS was reported by Vertes et al in the studies of *Allium cepa*, *Narcissus pseudonarcissus* bulb epidermis, and single eggs of *Lytechnius pictus*.[136] Later in 2010, LAESI-MS was applied for MSI of metabolites as well.[135] Laser desorption/ionization droplet delivery mass spectrometry (LDIDD-MS) is another laser assisted desorption/ionization ambient MS technique, and it was first introduced by the Nam and Zare groups in 2016.[137] In their studies, laser (15Hz, 266nm) and DESI (methanol:waster, 1:1 v/v, 5kV) were combined for desorption/ionization. With the assistance of laser, DESI created around 10 times higher extracted ion current. MSI experiments of mouse brain tissue and single cell analysis of HEK 293T cells were performed using this integrated method with 3 μm spatial resolution.

1.2.2.3 High throughput ambient techniques

Ambient SCMS techniques are usually coupled with microscopes to monitor the sampling process, providing users a more intuitive view of how single-cell analysis is performed. Although numerous ambient probe-based methods have been developed,

experiments generally require precise operating stage system, locating target single cells, and carefully optimizing experimental conditions; therefore, these methods generally have relatively lower experiment throughput comparing to vacuum-based SCMS techniques. To overcome this drawback, developing fluidic-based high throughput ambient SCMS techniques is regarded as an important direction. Inductively coupled plasma (ICP)-MS has been widely used for metal ion detection.[138] In 2018, the Yu and Wang groups developed the MicroCross sampling interface to quantify nanoparticles using ICP-SC-MS instrument.[139] A MicroCross adapter was connected by four quartz capillaries. The organic-continuous phase was injected from the first and second head-on flowing inlets, and the dispersed phase (i.e., cell suspension) was delivered from the third inlet of the MicroCross adapter. Mixing these two phases formed monodisperse droplets in the transport capillary, which was connected with the fourth inlet of the MicroCross adapter, to introduce single cells to ICP-MS. High throughput (~12 ms/cell) experiments were conducted to reveal cell heterogeneity based on the significant discrepancy of cellular uptake of nanoparticles (AuNPs).

Inertial-force-assisted droplet-free single-cell sampling (IDSS) was performed using eight circle spiral channels with a series of periodic dimensional confinement micropillars.[140] Inside these channels, 104 periodic dimensional confinement micropillars were fabricated to accelerate Dean-like secondary flow to align and sample single cells from cell suspension. Quantitative SCMS analyses were performed using this setup as described in the next section. To perform quantitative

analysis, another channel was used to provide the internal standard solution. This channel was connected with the outlet of the cell sample channel, and the mixture was measured by ICP-MS. High through analyses (3.7 ms/cell) were carried out to determine the accumulation of Cu^{2+} by MCF-7, bEnd3, and HepG2 cells to study cell heterogeneity.

Single-cell printer (SCP) is a commercially available device (Cytena Gmbh, Freiburg, Germany) that isolates single cells based upon microscopy and droplet operation. Cell suspension was continuously delivered to the nuzzle, which was monitored with microscopic devices, before being ejected. Droplets containing no cell or more than one cell were removed by vacuum suction to ensure single-cell isolation. Cahill *et al.* combined a SCP with the liquid vortex capture-mass spectrometry (SCP-LVC-MS) for high-throughput SCMS measurements in 2019.[141] SCP has also been adopted in single-cell proteomics studies, but this is out of the focus of this chapter.

High throughout SCMS experiments can also be conducted without using microfluidics or SCP. The intact living-cell electrolaunching ionization mass spectrometry (ILCEI-MS), which was introduced by the Wang group,[142] stands out due to its relatively simple design. Cell suspension was put in an in-house-built pressurized chamber, which was sealed and connected to a capillary with a constant inner diameter and a thin-walled tip. One end of the capillary was dipped into the cell suspension, and cells were introduced into the capillary driven by pressure from nitrogen gas. Because the inner diameter of the capillary was slightly smaller than cells, single cells moved in sequence to achieve single-cell isolation. A stainless-steel

needle was inserted in the cell suspension to apply a high voltage (1-2 kV), and the electric filed between the emitter and MS inlet induced single-cell electrolaunching. The ionization of single-cell components occurred in the ion-transfer tube of the mass spectrometer. More than 700 ions from over 5,000 cells were detected with a throughput of 51 cells/min.

1.3 Single-probe single cell mass spectrometry

The Single-probe, a miniaturized multifunctional device for *in situ* and real-time sampling, was introduced by the Yang group in 2014.[143] A dual-bore quartz needle was pulled on one side to form a sharp tip (~10 um), and a solvent-providing capillary and a nano-ESI emitter were inserted into the two channels from the back. During analysis, the solvent-providing capillary connected with a syringe continuously provides solvent. Liquid junction is formed at the dual-bore quartz needle tip, which is inserted into a single cell, to extract cellular analytes. The solution containing cellular analytes is automatically drawn to the nano-ESI emitter channel through self-aspiration followed by ionization. Extracted metabolites detected from MS include lipids, fatty acids, amino acids, and adenosine monophosphates (AMP, ADP, and ATP).[112, 144-146] In 2019, glass chips containing microwells were adopted as a substrate to reduce sample loss during the quantitative analysis of anticancer drug amounts. The results showed board distribution across different cells, indicating the cell heterogeneities in pharmacokinetics.[147] Using the Single-probe combined with an integrated cell manipulation system, studies have been extended to include both

adherent and non-adherent cells in 2021.[148, 149] Recently, Lu group modified the Single-probe by immobilizing TiO_2 onto the inner wall of the transfer capillary[150] and applying porous graphitic carbon for the Single-probe mass spectrometry imaging (MSI) to enrich the signals of low-abundance sphingolipids[151].

1.4 Quantitative mass spectrometry

While most SCMS methods excel in qualitatively examining molecular compositions, the pursuit of quantitative chemical insights, particularly concerning subcellular spatial distribution, remains a relatively unexplored frontier due to inherent limitation in many existing SCMS approaches. Quantitative SCMS techniques have emerged, predominantly building upon their qualitative counterparts, with advancements achieved through heightened instrument sensitivity, improved microscope resolution, more precise liquid handling, and the incorporation of standardized reference materials. These developments are instrumental in addressing the challenge of obtaining quantitative chemical information at the subcellular level, a fundamental requirement for comprehending cellular functions.

1.4.1 Relative quantification

As a comprehensive method, MS has the ability to obtain vast amounts of analytes at the same time. It is almost impossible to obtain absolute values for all analytes. Hence, relative quantification has been applied to compare the abundance of specific molecules. Due to the fact that absolute intensity varies for each scan, reference is required to normalize in standard. For an analysis using a certain

instrument, the total ion count (TIC) for each scan tends to be consistent. Hence, the signal from a uniform ‘constant’ background can potentially serve as a reference to measure the change of other species.[16] This technique is predicated on the consistent and reproducible response exhibited by a specific substance in all samples subjected to identical experimental conditions. When the observed variations in concentration are substantial enough to yield meaningful conclusions, this method can be readily employed. Notably, it offers the advantage of applicability to all components within a complex mixture without the necessity of introducing reference standards. Nevertheless, this method is not without its critiques, primarily concerning its susceptibility to signal instability in the chosen reference substances, and its vulnerability to potential errors stemming from the suppressive influence of competing ions. [152] Hence, introducing a chemical as internal standard is the other approach. Comparing with TIC normalization, this method has better stability. However, introducing a chemical could cause potential suppressive issue.

1.4.2 Absolute quantification

In traditional mass spectrometry (MS) analysis of bulk samples, the use of internal standards for absolute quantification is a common practice. [100, 153-156] However, in the context of absolute quantification, particularly in single-cell studies, a more stringent set of criteria is necessary compared to internal standards used for relative quantification. First and foremost, to account for disparities in ionization efficiency, it is imperative that the internal standard closely resembles the chemical structure of the compound to be quantified, preferably in the form of an isotopically-labeled isomer.

Secondly, these internal standards must also exhibit a similar abundance to the target compound. This similarity is crucial to prevent misleading artifacts arising from competition during the ionization process. Lastly, it is essential to recognize that a single internal standard may not suffice for simultaneously quantifying multiple components in a single assay. As a result, corrections for the recovery rate of both the internal standard and the target molecules must be determined and applied.

The materials in **Chapter 1** are adapted from an article under review in *TrAC.*

Chapter 2: Quantification of Nitric Oxide (NO) in Single Cells using the Single-Probe Mass Spectrometry Technique

2.1 Introduction

In life processes, bioactive small molecules play critical roles such as cell signaling, regulation of enzyme activities, and treatment of diseases. Among all bioactive small molecules, nitric oxide (NO) is particularly important, and its production and abundance are tightly relevant to many physiological and pathological processes.[157] NO is a signaling molecule regulating cell survival and proliferation in diverse biological systems.[157-159] For example, in the cardiovascular system, NO regulates blood flow and blood pressure. The recognition of its role as a cardiovascular signaling molecule has been acknowledged with the 1998 Nobel Prize in Physiology or Medicine.[157, 160-163]

In biological systems, NO can be produced from exogenous (i.e., provided by NO donor compounds) and endogenous (i.e., produced by cells) resources. Exogenous NO donor compounds have been applied to the treatment of heart and blood pressure related disease.[164, 165] For example, nitroglycerin (or glyceryl trinitrate) and sodium nitroprusside (SNP) contain NO in their structures, and they release NO through cell metabolism; they are widely used for the treatment of high blood pressure and heart failure.[166-168] Endogenous NO can be generated by cells through the catalytical

reaction of the NO synthases (NOSs, a family of enzymes catalyzing the production of NO).[165] For example, the anticancer drug doxorubicin (DOX) can promote the activities of NOSs, resulting in increased NO abundances in cells. [169-171]

The production and abundance of NO are tightly relevant to human health and diseases. For example, in the immune system, low concentrations of NO produce anti-inflammatory effects by inhibiting the proliferation of T helper cells; however, high concentrations of NO lead to strong proinflammatory responses under abnormal conditions.[172-176]

Similarly, the concentration of NO directly influences the angiogenesis in tumors: low concentration of NO promotes the growth and nutrition of tumors due to the formation of blood vessels, whereas high abundances of NO can suppress tumor growth.[177, 178] Previous studies showed the NO level in cancer cells changed after the anticancer drug treatment.[179, 180] Therefore, monitoring the abundances of NO in cells is important for both fundamental biological sciences and human diseases.

The abundances of NO in tumors can significantly vary from cell to cell. Factors affecting its intracellular abundances include the intrinsic cell heterogeneity, variances in the expression of NOSs,[181] and heterogeneity in immune response.[182] Cell heterogeneity has been observed in most biological systems and multiple human diseases such as cancer. Particularly, cell heterogeneity is regarded as a major challenge for cancer studies and treatment.[183, 184] Due to cell heterogeneity, NO levels in different single cells vary significantly.[176, 185, 186] However, quantitative measurement of NO in single cells is very challenging, primarily due to its extremely short lifetime

(<1s) and low amounts (10^{-19} Mole) in single cells as well as very complex cellular species.[187]

A variety of different methods have been developed for a quantitative analysis of intracellular NO. These analytical techniques include fluorescence[188-190], colorimetric[188, 191-193], chemiluminescence[194-196], electrochemical[197-199], gas chromatography[200, 201], electron paramagnetic or spin resonance (EPR or ESR) [202-205], and magnetic resonance imaging (MRI).[206, 207] Among these methods, fluorescence-based techniques are commonly used, and some of them have been adopted in studies of single cells.[208, 209] Because NO cannot directly produce fluorescence, probes (e.g., 2,3-diaminonaphthaline (DAN)) are needed to react with NO and produce fluorescent products for detection.[210] However, fluorescence-based methods have several drawbacks, including interference of cellular autofluorescence and side reactions of NO with other species.[210] In addition, these techniques are unable to detect nonfluorescent molecules, limiting their applications to studying broader ranges of cellular species.

Mass spectrometry (MS) is a powerful tool to sensitively detect and accurately identify molecules at low abundances in a complex matrix.[211-213] Recent developments in MS lead to the creation of a variety of different single cell MS (SCMS) methods. Based on their sampling and ionization conditions, these SCMS techniques can be generally classified into two groups: vacuum-based and ambient methods.[15, 17, 20, 214] Vacuum-based methods require high vacuum environment during analysis and complex sample preparation, but their sensitivity and throughput are relatively higher.

Matrix Assisted Laser Desorption/Ionization (MALDI) and secondary ion mass spectrometry (SIMS) are two wildly applied methods for SCMS and mass spectrometry imaging (MSI).[15, 215-217] To overcome certain drawbacks of vacuum-based methods, numerous ambient SCMS techniques have been developed. These methods include desorption electrospray ionization (DESI)[218, 219], nanospray desorption electrospray ionization (nano-DESI)[220-222], video-MS[97, 223, 224], Single-probe[143, 145, 225], T-probe[113, 114], laser ablation electrospray ionization (LAESI)[135, 226], and pulsed direct current electrospray ionization mass spectrometry (Pico-ESI-MS)[227, 228].

MS is wildly used for quantitative analysis of cellular compounds such as metabolites and proteins.[229, 230] In relatively quantification experiments, the intensities of ions of interest are commonly normalized to the total ion intensity (TIC) for comparison.[16] This method has been often used in SCMS studies due to its convenience.[16, 143] Another strategy for relative quantification is to add an internal standard with a fixed concentration into all samples, and intensities of all target ions are then normalized to that of the internal standard.[100] In absolute quantification studies, internal standard spiking and standard addition are generally used. When the isotopically labeled compound is used as the internal standard, the target compound, which has the same structure as the internal standard, can be quantified without using any calibration curve.[144, 147] However, due to the complexity of biological systems, isotopically labeled internal standards for multiple target molecules may not be conveniently available. Therefore, using unlabeled internal standards (e.g., analogs with structures similar to the target molecules) and calibration curves of target

molecules is an effective approach to absolute quantification.[178] Standard addition is another strategy, in which a series of samples containing different amounts of standard are prepared. Based on the response curve, the absolute abundance of target molecule can be determined.[231]

Quantitative measurement of analytes in single cells is very challenging, primarily due to their extremely limited sizes and complex compositions. Only a few SCMS techniques have been developed for absolute quantification of molecules in single cells. Yin et al. used electroosmotic extraction method to quantitatively extract *Allium cepa* cell and an internal standard (glucose-d2 solution) into a nanopipette for MS analysis.[153] Our group has developed the quantitative Single-probe SCMS methods to measure the absolute abundances and concentrations of anticancer drugs in single cells.[144, 147, 149] The Single-probe is a miniaturized, multifunctional device for *in situ* sampling and real-time MS analysis. To fabricate a Single-probe, a solvent-providing fused silica capillary and a nano-ESI emitter are embedded into two channels of a dual-bore quartz needle, which is laser-pulled to form a sharp tip (~10 um). During our routine SCMS analysis, the Single-probe tip is inserted into the target cell to extract cellular contents by a liquid junction of the solvent (e.g., acetonitrile with 1% formic acid) formed on the tip. The extracted cellular contents are spontaneously drawn to the nano-ESI emitter through a self-aspiration process. In quantitative Single-probe SCMS experiments, the internal standard (e.g., an isotopically labeled compound) is added in the solvent with a known concentration. The extracted target molecule in single cells are simultaneously ionized along with the internal standard for MS

detection.[232, 233]

The quantitative Single-probe SCMS experiments have been conducted for both adherent and suspended cells. For adherent cell, a glass chip containing microwells (diameter: 55 μm; depth: 25 μm) was used as a substrate for cell culture.[147] During experiments, only single cells inside single microwells were analyzed. The microwells were able to minimize the diffusion loss of molecules, including cellular contents, the target molecules (e.g., anticancer drug irinotecan absorbed the cell), and the internal standard (e.g., irinotecan-d10), to ensure accurate quantification.[147] To analyze suspended cells, an integrated cell manipulation platform was coupled to the Single-probe SCMS setup. A single cell was captured using a cell-selection probe connected to a microinjection, which was used to provide a gentle suction for cell capture, and moved to the Single-probe tip.[144] The liquid junction of the sampling solution (e.g., acetonitrile containing isotopically labeled drug compounds) formed on the probe tip immediately lysed the captured cell, and the single cell lysate was then analyzed by MS in real-time to obtain drug quantity. In order to determine the concentration of target molecules (e.g., anticancer drug), cell images were token during cell selection to estimate the volume of each target.[144]

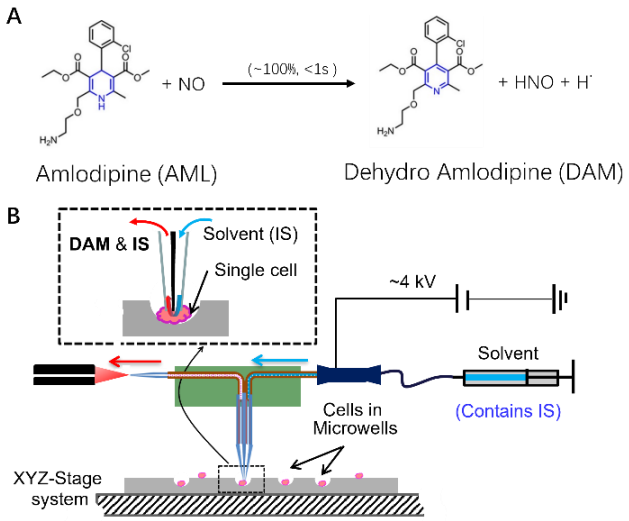

Figure 1 Quantification of NO in single cells. (A) Reaction of AML and NO producing DAM. (B) Quantitative Single-probe SCMS cell setup. Glass chip containing microwells is used for cell culture and SCMS experiment.

To the best of our knowledge, there are no reported studies of using MS method to quantify NO from single cells. Due to NO's small molecular weight, high reactivity, and dissuasive properties, it is challenging to directly analyze this molecule using MS-based methods. Detecting NO from live single cell is more challenging because of its limited amount in each cell. Alternatively, chemical reactions have been used for indirect MS detection of NO. It has been reported that Hantzsch ester can react with NO with a high efficiency and specificity.[234-237] Using amlodipine (AML), a compound containing Hantzsch ester group,[238] NO can efficiently (100%) and rapidly (<1 s) react with AML to produce dehydro amlodipine (DAM), a stable compound that can be sensitively detected by MS (Figure 1A).[178] Because this reaction efficiency is nearly 100%,[178] NO can be quantified by measuring the amount of DAM produced from this reaction.[178] These studies also demonstrated that AML does not react with other

reactive cellular species (e.g., reactive oxygen and nitrogen species as well as biological reductants) to produce DAM.[178] The integration of SCMS technique with chemical reactions has been utilized in our previous studies of carbon double (C═C) bonds in unsaturated lipids.[112] In the current study, we combined the quantitative Single-probe SCMS technique with the above chemical reaction (Figure 1A) to quantitatively measure the amounts of NO in single cells.

2.2 Experimental section

2.2.1 Experimental materials and instruments

All data were obtained using a Thermo LTQ Orbitrap XL mass spectrometer (Thermo Scientific, Waltham, MA, USA). DAM extracted from cell lysates were analyzed using a nanoACQUITY ultra performance liquid chromatography (LC) (Waters, Milford, MA, USA) coupled to the Orbitrap mass spectrometer.

Chemicals: amlodipine (AML, Cayman Chemical, MI, USA); dehydro amlodipine (DAM, Santa Cruz Biotech, TX, USA); oxasulfuron (OXF, internal standard for SCMS quantification of DAM); d_4-AML (internal standard for LC-MS quantification of DAM, Cayman Chemical, MI, USA); sodium nitroprusside (SNP, Cayman Chemical, MI, USA); doxorubicin (DOX, Alfa Aesar, MA, USA).

2.2.2 Cell culture

Human colon cancer cells (HCT-116) were originally obtained from American Type Culture Collection (ATCC; Rockville, MD, USA). Cell culture medium for HCT-116 is McCoy's 5A cell culture medium containing 10% FBS (fetal bovine serum) and 1% Pen

Strep (Life Technologies, Grand Island, NY, USA). All cells were cultured at 37°C in an incubator with 5% CO_2 supply (HeraCell, Heraeus, Germany). To prepare cells for SCMS experiments, cells were seeded in 12-well plates (5.0 x 10^5/mL with 2 mL/well) containing microwell glass chips. To prepare cells for LC/MS experiments, cells were seeded in Petri dishes (10 mL/dish) 12 hours prior to the drug treatment. AML (dissolved in DMSO) was added into culture medium (with a final concentration of 2.0 μM AML) to treat the cells for 2 hours, and then the medium was disposed. Cells were washed by PBS for two times, and the prepared culture medium containing SNP (exogenous group) or DOX (endogenous group) was used to treat cells for 24 hours. Cells were then rinsed by fresh cell culture medium prior to direct SCMS experiments. In addition, rinsed cells were used for lysate preparation, DAM extraction, followed by LC/MS analysis.Cells in control groups, which were treated by AML (without SNP or DOX), SNP (without AML), or DOX (without AML), were used to determine if DAM is solely produced from the reaction between AML and exogenous or endogenous NO.

2.2.3 Single-probe SCMS

The Single-probe is a multifunctional sampling and ionization device. A Single-probe is fabricated by integrating three major components: a needle pulled from dual-bore quartz tubing (outer diameter (o.d.) 500 μm; inner diameter (i.d.) 127 μm; tip size <10 μm; Friedrich & Dimmock, Inc., Millville, NJ, USA) using a laser pipet puller (P-2000 micropipette puller, Sutter Instrument, Novato, CA, USA), a fused silica capillary (o.d. 105 μm; i.d. 40 μm; Polymicro Technologies, Phoenix, AZ, USA), and a nano-ESI emitter produced using the same type of fused silica capillary. Detailed description of

the device fabrication and utilization has been reported in our previous studies.[143, 145, 147, 225, 232] Mass spectrometer settings include the ionization voltage of 4.5 kV, mass resolution of 60,000 (at m/z 400), isolation window of 1 m/z, CID of 20 normalized collision energy (NCE), and mass range from m/z 100-450. The sampling solution used in SCMS experiments was acetonitrile (ACN) containing 0.1% formic acid (FA) and 1.0 μM OXF, and the optimized flow rates range between 0.1 μL/min and 0.3 μL/min in each experiment.

2.2.4 LC/MS

After disposing used medium, cells were washed by PBS. 2 mL 0.5% trypsin was used to detach cells for 3 mins, and trypsinization was stopped by adding 8 mL of culture medium. Cells were centrifuged at 1,000 rpm for 5 min, resuspend by PBS for washing, and then counted (BioRad TC20 cell counter, USA). To prepare cell pellet, cells were centrifuged at 1,500 rpm for 5 min. After discarding the supernatant, 200 μL Tris buffer (pH = 8.0) containing 8 M urea was added to cell pellet. The mixtures were sonicated for 20 s (FS-300N, Edeardda; with 50% power) and shaken (with ice bath) by orbital shaking for 5 min at 100 rpm. To precipitate proteins and extract DAM, 800 μL cold acetone (-20°C) was added into the cell lysate prior to overnight storage (-20°C). Stored samples were centrifuged at 12,300 rpm at 4°C for 5 min, and the supernatant was collected to another Eppendorf tube and dried at room temperature using a SpeedVac (SPD111V, Thermo Scientific, San Jose, CA, USA). The dried samples were resuspended in 200 μL methanol/water solution (methanol (20%)/ H_2O (80%) with 0.1% FA). To desalt samples, 10 μL C18 desalting tips (PureSpeed, Rainin Pipetting 360°,

Oakland, CA, USA) were used following vendor's protocols. The eluted solutions were dried by the SpeedVac, and the dried samples were resuspended in 90 μL solution (MeOH (20%)/H_2O (80%) with 0.1% FA) and 10 μL internal standard (100 nM d4-AML).

Home-packed trap column (150 μm, 50mm, 3 μm, 100 Å; Daisogel, Japan) and C18 capillary column (150 μm, 150mm, 3 μm, 100 Å; Daisogel, Japan) were used for LC separation. Mobile phases A (ACN containing 0.1 % FA) and B (H_2O containing 0.1 % FA) were sonicated for 30 min to remove gas before use. During the analysis, 2 μL sample was injected into the trap column, followed by 5 min trapping using 5% mobile phase B at a flow rate of 3 μL/min. Separation was performed in the analytical column at a flow rate of 500 nL/min and a column temperature of 50 ℃. LC gradient started from 5% mobile phase B for the first 1 min, followed by a quick increase to 45% mobile phase B in 5min. In the next 12 min, the percentage of mobile phase B was increased to 95% and held for another 5 min. Then the gradient of mobile phase B was changed back to 5% for 10 min re-equilibrium. The outlet of the analytical column was connected to a nanoESI emitter. The MS analysis parameters are listed as follows: ionization voltage +2.0 kV, ion transfer tube temperature 250 ℃ mass range 150–1,500, mass resolution 60,000 at m/z 400, 1 microscan, 500 ms max injection time, and automatic gain control (AGC) on with the target value of 1E6. Each lysate was analyzed for three times (i.e., three analytical replicates).

2.2.5 Extraction efficiency of DAM.

For accurate quantification in LC/MS, the extraction efficiencies of DAM were measured from LC/MS analyses of two groups of cell lysate solutions.

1. Reference cell lysate solutions.

These solutions were prepared from redissolved cell lysate extracts and then spiked with both DAM and its internal standard (d4-AML), implying 100% extraction efficiency of DAM. First, we prepared cell pellets. 0.77−3.62x10^6 cells/mL of cell suspension were aliquoted to 11 portions, and each portion (1 mL cell suspension) was centrifuged to prepare one pellet. The supernatant was discarded. Second, we prepared cell lysate solutions. Each cell pellet was lysed by urea (8 M). Using the above protocols (D. LC/MS), we performed protein precipitation, extraction of DAM, drying, desalting, and redissolution. Third, we spiked both DAM and d4-AML into lysate extracts for LC/MS measurements. Each redissolved extract was spiked with different amounts of DAM (with final concentrations of 2.0, 5.0, 7.5, 10.0, 12.5, 15.0, 17.5, 20.0, 25.0, 30.0, and 50.0 nM) but the same amount of d4-AML (10.0 nM final concentration). The final volume of each solution is 100 μL. d4-AML was selected as the internal standard because its retention time is nearly the same as DAM, minimizing the difference of matrix effects, which are induced by co-eluted matrix components, and instrument fluctuation during LC/MS quantification.[239] Last, we conducted LC/MS measurements. Without further extraction (i.e., 100% extraction efficiency), these samples were directly used for LC/MS analysis to obtain the relative peak areas of DAM/d4-AML.

2. Cell lysate solutions containing extracted DAM and spiked d4-AML.

To prepare these solutions, extracts were obtained from cell lysates containing DAM, redissolved, and then spiked with d4-AML for LC/MS measurements. First, we

prepared cell pellets using the same protocols as described above. Second, we prepared DAM-containing solutions of cell lysates. Each cell pellet was lysed using urea (8 M). Different amounts of DAM was added into lysates with a series of final concentrations (i.e., 2.0, 5.0, 7.5, 10.0, 12.5, 15, 17.5, 20.0, 25.0, 30.0, and 50.0 nM). Third, we extracted DAM from cell lysate solutions using cold acetone following the same protocols provided above (D. LC/MS). Fourth, we spiked d4-AML (10 nM final concentration) into each redissolved extract. Last, we performed LC/MS analysis of these samples to acquire the relative peak areas of DAM/d4-AML.

Three analytical replicates for each group were tested. The DAM extraction efficiency of DAM (48.5 ± 7.4 %) was determined by comparing the ratios of DAM/d4-AML obtained from these two groups of samples. This measured DAM extraction efficiency was used to correct the LC/MS measurement of average intracellular DAM (i.e., NO).

2.2.6 Data analysis of cell subpopulations

SCMS and LC/MS raw data were accessed using Xcalibur 5.0 (Thermo Fisher Scientific). In SCMS experiments, the detection of single cells was confirmed from the appearance of typical cellular species (e.g., PC(34:1), m/z 782.567).[143] The LC/MS retention time was measured as 21.47 and 21.81 min for DAM and d4-AML, respectively. The peak areas of both DAM and d4-AML were exported from Xcaliber and imported into Microsoft Excel for quantification.

D>2 Ashman's criterion was used to confirm the presence of subpopulations with normal distributions in SNP (exogenous NO) treatment groups. By applying the mean

and standard deviation, the D>2 Ashman's criterion for normal distribution were calculated using Eq. 1:

$$D_{12} = \frac{\sqrt{2}|\mu_1 - \mu_2|}{\sqrt{\sigma_1^2 + \sigma_2^2}} \quad \text{(Eq. 1)}$$

The presence of two subpopulations is confirmed if $D_{12} > 2$ in the *post hoc* grouping.

Gamma distribution functions were used to fit results from DOX (endogenous NO) treatment groups. The dip test (R package 'diptest') was used to determine if subpopulations exist. The null hypothesis is that only monomodal is present in the dataset (Supporting information).

All fittings were generated by a home-made python script (Supporting information).

2.3 Results and discussion

2.3.1 Establishment of calibration curves

A. SCMS

During SCMS measurements, intensive isobaric background ions (ranging from m/z 407.1040 to 407.2090) interfered with the isolation and detection of the target ion DAM ($[DAM+H]^+$, m/z 407.1325, Figure S1). These interfering ions significantly affected the direct quantification of NO (i.e., DAM) in single cell using MS1. In contrast, our experiments showed that the MS/MS spectra of the interfering ions were significantly different from those of $[DAM+H]^+$ (Figure S2), indicating that DAM quantification can be performed using MS/MS to eliminate the influence of interfering ions. Due to the unavailability of isotopically DAM compounds, oxasulfuron (OXF) was

chosen as the internal standard of DAM. This is because $[OXF+H]^+$ (m/z 407.1020) can be co-isolated with $[DAM+H]^+$ (m/z 407.1325) for MS/MS analysis, whereas their fragments are significantly different (Figures S3 and S4). Another benefit of using MS/MS quantification is that mass spectra with a cleaner background can be obtained (Figure S5), resulting in improved detection sensitivity due to increased signal-to-noise ratio.[240] Our experiments indicated that, using the Single-probe SCMS setup, the limit of detection for DAM is 0.2 and 0.05 nM in MS1 and MS/MS measurements, respectively.

To establish the MS/MS calibration line, the Single-probe setup was used to analyze calibration solutions, mimicking the SCMS experimental conditions. A series of cell lysate solutions containing DAM (i.e., 0.2, 0.5, 1.0, 2.0, and 5.0 nM) and OXF (1.0 μM) were prepared as the calibration solutions. These calibration solutions were added into containers and sampled by the Single-probe for MS/MS (using CID at 20 NCE) data acquisition. The following two equations (Eq. 2 and 3) were used to construct the calibration curve:

$$\frac{\sum A}{\sum B} = a\frac{X}{Y} + b \qquad \text{(Eq. 2)}$$

$$Y = c_Y * t * v_Y \qquad \text{(Eq. 3).}$$

ΣA and ΣB are the integrated ion intensities (i.e., peak areas) of fragments of DAM and OXF, respectively; *a* and *b* are constants; *X* and *Y* are the amount (in moles) of DAM and OXF, respectively. Because the internal standard OXF is provided through the sampling solvent, its quantity can be obtained from its concentration c_Y, the data

acquisition time for each cell *t*, and flow rate of the solution v_Y. The major (i.e., most abundant) fragments in MS/MS spectra of DAM (m/z 346.0820) and OXF (m/z 150.0663) were used to construct the calibration curve. The linear regression function resulted in an excellent fitting (R^2 = 0.9933) (Figure 2A). This calibration curve was then used for quantitative SCMS measurements of DAM in single cells. All experiments were performed using the same instrument settings and on the same day.

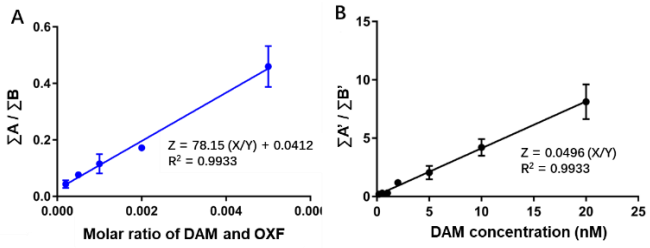

Figure 2 Calibration curves for (A) quantitative SCMS and (B) LC/MS measurements of intracellular NO amounts. ∑A and ∑B indicate MS/MS fragments' peak areas of DAM and OXF, respectively. ∑A' and ∑B' indicate MS1 peak areas of DAM and d4-AML, respectively.

B. LC/MS

LC/MS experiments were conducted to obtain the average NO amounts in single cells. To mimic the matrix effect in LC-MS experiments, cell lysate was used to prepare solutions containing the standard compounds. Briefly, cell lysate was dissolved in the solvent (MeOH (20%)/H_2O (80%) with 0.1% FA). Both DAM and d4-AML (the internal standard for DAM) were added into the solutions with different final concentrations (i.e., DAM: 0.2, 0.5, 1.0, 2.0, 5.0, 10, and 20 nM, d4-AML: 100nM). Cell lysate aliquots were spiked with different amounts of DAM (final concentrations: 0.2, 0.5, 1.0, 2.0, 5.0, 10,

and 20 nM) but a fixed amount of d4-AML (final concentration: 100 nM). Each sample was analyzed with three analytical replicates. Because all interfering species were eliminated by LC separation, MS1 spectra were used to construct the LC/MS calibration curve using Eq. 2, whereas ΣA' and ΣB' indicate peak MS1 areas of DAM and d4-AML, respectively. X and Y represent the concentrations of DAM and d4-AML, respectively. The linear regression function resulted in an excellent fitting (R^2 = 0.9892) (Figure 2B). This calibration curve was then used for quantitative LC/MS measurements of DAM in cell lysates. All experiments were performed using the same instrument settings and on the same day. For accurate quantification, the extraction efficiencies of DAM from cell lysates were measured. (E. Extraction efficiency of DAM). This measured extraction efficiency (48.5 ± 7.4 %) was then used to correct the LC/MS quantification of average intracellular DAM (i.e., NO) (Table 1).

		SCMS		LC/MS
Cell group	**Treatment* concentrations**	**Amount (amol)**	**n****	**Amount (amol)**
SNP-L	0.25 mM	23.4±13.9	41	0.82±0.10
SNP-M	1.0 mM	25.3±22.7	48	1.92±0.12
SNP-H	4.0 mM	60.4±67.0	51	5.47±0.41
DOX-L	0.75 μM	36.8±40.5	94	2.91±0.20
DOX-M	2.0 μM	46.6±48.0	41	4.05±0.17

DOX-H	4.0 μM	61.7±93.9	60	10.72±0.48

Table 1 Amounts of NO in single cells measured using SCMS and LC/MS methods.

*Cells were treated by SNP (sodium nitroprusside) or DOX (doxorubicin) for 24 h.

**n indicates the number of single cells measured in each SCMS experiment.

2.3.2 SCMS quantification of exogenous and endogenous NO in single cell

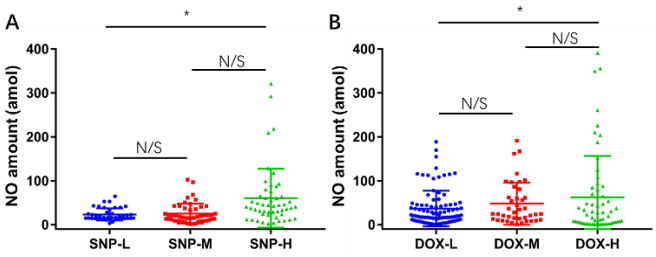

Figure 3 Box plots indicating (A) exogenous (SNP treated, 24 h) and (B) endogenous (DOX treated, 24 h) NO amounts (amol) in single cells. (*: $p<0.05$, N/S: no significant difference)

Cells were attached onto the microwell glass chip through incubation (Figure 1B). Using similar experimental protocols reported in our previous studies,[147] only microwells containing one cell were measured using the Single-probe SCMS setup. 1.0 μM OXF (the internal standard for DAM) was added in the sampling solvent, of which the flow rate was recorded for the analysis of each cell. The total amount of OXF was calculated using Eq. 3. Based on the calibration curve (Figure 2A), the integrated intensities of major fragments of DAM and OXF were used to quantify DAM in each

cell. For the control group, DAM was not detected which indicated the tiny influence of other factors on the reaction forming DAM.

In SCMS studies of exogenous NO, AML treated cells were rinsed and then incubated (for 24 h) in medium containing three different concentrations of sodium nitroprusside (SNP), i.e., low (SNP-L, 0.25 mM), medium (SNP-M, 1.0 mM), and high (SNP-H, 4.0 mM). As a NO donor, SNP can be absorbed by cells and release NO through reactions with sulfhydryl groups in proteins.[167, 168] NO molecules then react with intracellular AML and produce DAM (Figure 1A). Cells (n = 41−51) in each group were analyzed using the Single-probe SCMS technique. Our experimental results indicated broad distributions of intracellular NO of cells in all three groups, very likely due to cell heterogeneity (Figure 3A). Similarly, heterogeneous anticancer drug uptake in single cells has been observed in our previous studies.[144, 147] The average NO amounts in SNP-L, SNP-M, and SNP-H group are 23.4 ± 13.9, 25.3 ± 22.7, and 60.4 ± 67.0 amol (10^{-18} mole)/cell, respectively (Table 1). Although there is no significant difference of results between the SNP-L and SNP-M treatment groups (t-test, $p>0.05$), higher concentration treatment in the SNP-H group significantly boosted NO production comparing to SNP-L treatment group (t-test, $p<0.05$) (Figure 3A).

In the studies of endogenous NO in single cells, AML treated cells were rinsed and then incubated in medium containing anticancer drug doxorubicin (DOX), which stimulated the production of NO. As a transient paracrine and autocrine signaling molecule, NO plays important functions in the cellular and intercellular drug responds.[241, 242] Previous studies proved that NO level in HCT-116 cells can be

increased by DOX treatment due to elevated NOSs activities.[169, 170] To evaluate the relationship between DOX concentration and amount of endogenous NO in cells, HCT-116 cells were treated (for 24 h) by DOX at three different concentrations, i.e., low (DOX-L, 0.75 μM), medium (DOX-M, 2.0 μM), and high (DOX-H, 4.0 μM). Cells (n = 41−94) in each group were then analyzed using the Single-probe SCMS technique. Broad distributions of intracellular NO amounts were observed (Figure 3B). The measured NO amounts in single cells from the DOX-L, DOX-M, and DOX-H groups are 36.8 ± 40.5, 46.6 ± 48.0, and 61.7 ± 93.9 amol/cell, respectively (Table 1). Similar to results obtained from exogenous NO treatment, there is no significant difference between the DOX-L and DOX-M treatments (t-test, $p<0.05$), but higher concentration of DOX in the DOX-H group significantly stimulated NO production comparing to DOX-L group (t-test, $p<0.05$) (Figure 3B).

The mean values (23.4–61.7 × 10^{-18} mol/cell) of NO abundances in single cells obtained from our experiments may not be fairly compared with previously reported results. In fact, intracellular NO abundances can significantly vary for different cell systems. For example, the amounts of NO in RAW 264.7 cells, which were stimulated by lipopolysaccharide (LPS) to produce NO, were reported as 1.4–2.1 × 10^{-16} mol/cell[243, 244], whereas PC-12 cells exhibited a broad range of 4× 10^{-18} –4.5 × 10^{-14} mol/cell[208, 245]. To the best of our knowledge, there is no reported studies of the same cell system used in our current work. Therefore, direct comparison the single-cell level cannot be performed. It has been reported AML treatment can stimulate the production cellular NO. However, in our control experiment, we were unable to detect DAM in

single cells only treated by AML, which can scavenge NO and produce DAM. Our results indicate that the amounts of NO, if any, induced by AML in HCT116 cells were below the detection limit of our Single-probe SCMS technique.

2.3.3 Subpopulation analysis of NO quantities in single cells

Cell groups	Subpopulation 1 (amol)	Subpopulation 2 (amol)
SNP-L	15.7 ± 4.8	40.5 ± 11.6
SNP-M	13.3 ± 6.9	52.3 ± 22.3
SNP-H	33.6 ± 19.3	96.7 ± 18.2

Table 2 Amount of exogenous NO in single cells in two subpopulations.

Cell heterogeneity has been studied at different levels, such as transcriptomics and metabolomics, using statistical tools. Cells' subpopulations can be evaluated based on the overall molecular profiles. For example, we have previously developed a tool, SinChat_MS, to quantify cell subpopulations based on their global metabolites in single cells.[233] This tool can be also used to prioritize metabolite biomarkers of cell subpopulations and correct batch effect in SCMS studies. Cell subpopulation analysis can be also performed using individual cellular species. For example, Vertes *et al.* used gamma and normal distribution functions to fit the intensity distributions of multiple molecules (e.g., malate and ascorbate) in *E. densa* epidermal cells and *G. max*-infected root nodule cells and obtained subpopulations.[246]

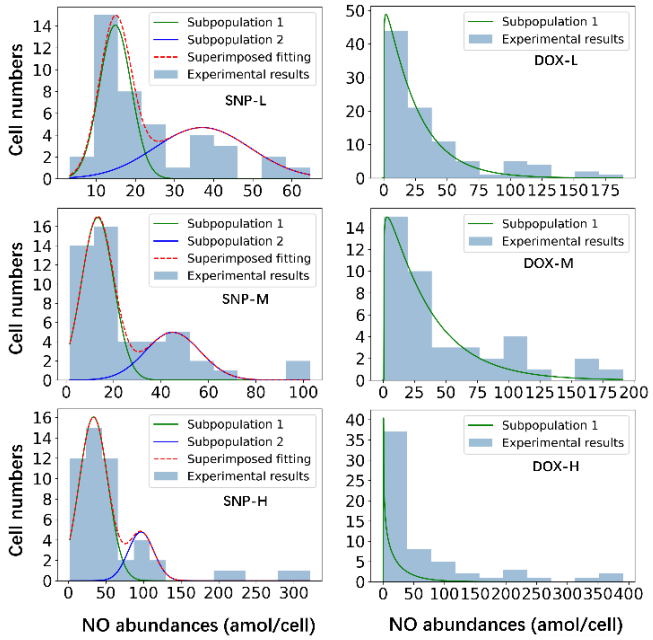

Figure 4 Distributions of NO amounts in single cells. Bimodal (normal) distributions were observed in exogenous NO groups (SNP treatment, left panel). Unimodal (gamma) distributions were observed in endogenous NO groups (DOX treatment, right panel).

In the current studies, we investigated the cells' subpopulations, which reflect cells containing different amounts of NO, by fitting the distributions of NO amounts in single cells. We evaluated different distribution functions, and we discovered that normal and gamma distribution functions provided the best fittings for endogenous and exogeneous NO groups, respectively (Figure 4). Our fitting results also indicate there are two subpopulations of cells in all three exogeneous NO treatment groups (Figure 4, left column). We further confirmed the presence of two subpopulations using the D>2 Ashmans's criterion.[246, 247] The D_{12} values for subpopulations 1 and 2 are 3.67, 4.00, and 2.31 for SNP-L, SNP-M, and SNP-H treatment groups, respectively. The t-test results indicate that these two subpopulations of cells contain significantly different

($p < 0.05$) amounts of NO. The average amounts of NO in single cells from two subpopulations are summarized in Table 2. Compared with results shown in Table 1, grouping cells into two subpopulations leads to significantly reduced standard deviations. For cells containing endogenous NO, we observed one population (gamma distributions) in all three treatment groups (Figure 4, right column). To determine if there are multimodal distributions, dip test has been performed, yielding no clear evidence of multimodality (Supporting Information). Our results indicate that exogenous and endogenous treatment conditions resulted in different modalities of distributions of NO amounts in single cells, likely due to different levels of toxicities between SNP and DOX. Although there is no reported assessment of SNP toxicity to HCT-116 cells, our cell culture experiments indicated that, compared with cells in normal growing conditions, cell growth was not obviously inhibited by SNP at all three concentrations. Thus, more heterogenous cells were analyzed in our SCMS experiment. In contrast, DOX is a potent anticancer drug (IC_{50} = 0.96 ± 0.02 μM (72 h) for HCT-116 cells).[248] Under our DOX treatment conditions (0.75, 2.0, or 4.0 μM for 24 h), cells with relatively low drug resistance can be largely eliminated from SCMS measurements, resulting in less cell heterogeneity. Although broad distributions of intracellular NO amounts were observed in the previous studies, which were primarily based on fluorescence microscopy techniques, further investigation of cell subpopulations was not conducted.[208, 244, 245, 249] The difference of cell heterogeneity can be potentially validated using other single cell analysis techniques such as single cell RNA sequencing. However, these studies are beyond the scope of our current

studies.

2.3.4 LC/MS quantification of NO in cell lysates

In the comparative studies, LC/MS analyses of cell lysates, which were prepared using cells under the treatment conditions that are the same as those in SCMS studies, were carried out to obtain the average quantities of NO in single cells. The total amounts of NO in cell lysates were calculated using the calibration curve (Fig. 2B), with the correction of extraction efficiencies. The average NO amounts in single cells were then calculated based the total number of cells in each sample (Table S1). First, LC/MS results exhibit a clear trend: the intracellular NO amounts increase as the treatment concentrations of SNP and DOX increase. This trend cannot be clearly observed in our SCMS measurements of cells treated by low and medium concentrations of SNP and DOX, likely due to a relatively small difference of intracellular NO abundances and cell heterogeneity. Second, the mean values of our SCMS results (23.4–61.7 × 10^{-18} mol/cell) are generally higher than those from our LC/MS measurements (0.9–10.7 × 10^{-18} mol/cell). This difference is likely due to cell heterogeneity in SCMS experiments, which also resulted in large standard deviations, and potential DAM loss in multiple sample preparation steps such as trypsin detachment and multiple rounds of cell washing and centrifugation. During these procedures, intracellular DAM might be lost due to cell rapture and diffusion across cell membrane, whereas the internal standard (d4-AML) cannot be added in these steps to compensate this loss. SCMS involves minimal sample preparation, which reduces the change of DAM loss between sample preparation and measurement. Sample loss

during LC/MS sample preparation can likely result in small amounts of DAM compared with those in SCMS experiments. Similar trends have been observed in our previous studies of intracellular anticancer drug compound.[147] Third, our LC/MS results are lower than that (~0.6×10^{-16} mol/cell) in LPS stimulated RAW 264.7 cells measured by LC/MS methods[178], likely due to the intrinsic differences between these two cell lines and treatment conditions.

2.4 Conclusion

We combined the quantitative Single-probe SCMS technique with chemical reactions, in which AML quantitatively reacts with intracellular NO to produce DAM, to quantify NO amounts in live single cells. Two different compounds (i.e., sodium nitroprusside (SNP) and doxorubicin (DOX)) with different concentrations were used to produce exogenous (by SNP) or endogenous (by DOX) NO. Under all treatment conditions, intracellular NO amounts exhibited heterogenous distributions. The distributions of NO amounts in single cells were analyzed, and results indicated that two subpopulations of cell were present in all exogenous NO treatment groups, whereas only one population was discovered in each endogenous NO treatment group. This difference can be potentially attributed to different toxicities between SNP and DOX. Comparison studies of lysates of cells treated under the same conditions were performed using LC/MS method. The mean values obtained from single cells were significantly higher than those measured from population cells, likely due to cell heterogeneity and potential drug compound loss during cell lysate preparation. The

technique reported in the current study is applicable of quantifying NO in many other types of cells. However, this technique has a relatively low throughput due to manual selection and analysis of single cells. This drawback can be potentially solved by developing high throughput SCMS methods. In addition, this method is largely limited to analyze adherent cells, whereas measuring non-adherent cells requires additional instrument modification.[149, 250] The strategy of combining SCMS techniques and chemical reactions can be potentially further developed to study other cellular species of interest.

The materials in **Chapter 2** are adapted from an article just accepted in *Analytical Chemistry* Nov 2023.

Chapter 3: Single-Cell Mass Spectrometry Enables Insight into Heterogeneity in Infectious Disease

3.1 Introduction

Cell heterogeneity commonly presents in nearly all biological systems. In addition to the genetic variation, cellular heterogeneity can be induced by nongenetic mechanisms, i.e., cells possessing similar genotypes but actually expressing morphological and phenotypical differences.[181, 251] Although cell heterogeneity has been reported in human diseases, such as cancer, diabetes, and chronic and age-related diseases[252], it is largely understudied in infectious disease. For the first time, this study will pave the way to study the heterogeneity that presents in infection with *Trypanosoma cruzi* (*T. cruzi*) at the single-cell level.

T. cruzi is a protozoan parasite causing Chagas disease (CD), which is an understudied tropical disease with severe cardiac and gastrointestinal symptoms. At the cellular level, *T. cruzi* trypomastigotes invade host cells and differentiate into amastigotes, which can proliferate, differentiate back into trypomastigotes, and then escape the host cells. These newly produced trypomastigotes can then invade new cells and continue this cycle of damage.[253] *T. cruzi* infection results in a major deregulation of lipid and glucose metabolism in the host cells.[254, 255] Metabolic alterations proportional to CD severity were observed in the heart during experimental *T. cruzi* infection.[256, 257] Differential spatial distribution of metabolic alterations in

experimentally-infected animals reflects sites of Chagas disease tropism.[258-260] However, all of these reported studies have been performed using traditional metabolomic, gene expression, or functional studies from extracts and lysates prepared from cell populations or infected tissues, which masks cellular-level heterogeneity and cellular-level spatiality.

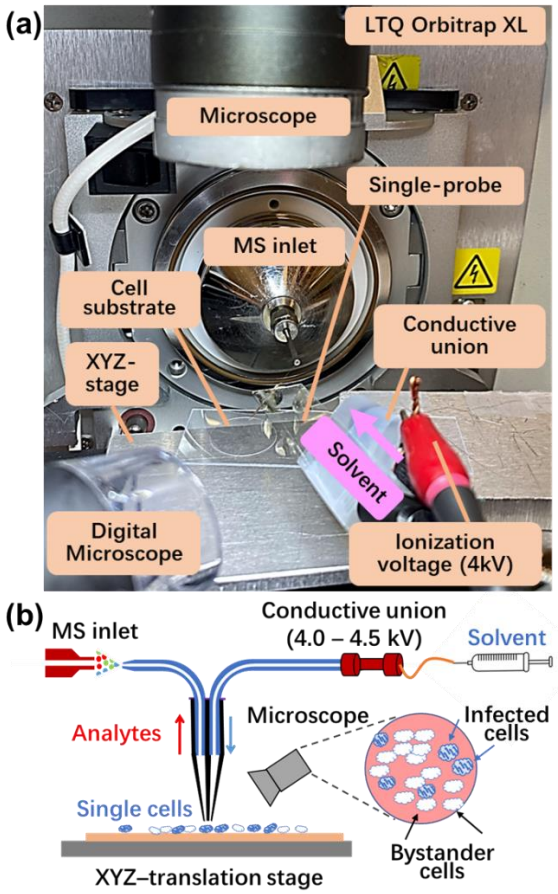

Figure 5 (a) Photo of the Single-probe single cell mass spectrometry (SCMS) setup. (b) The schematic of the working mechanisms of the experimental setup.

Although single cell transcriptomics[261-263] and proteomics[264, 265] are increasingly important, metabolomics insight at the single-cell level can investigate cellular function that may not be rendered by other methods. Metabolites are smaller molecules (<1.5

kDa), including sugars, lipids, and amino acids.[266, 267] Metabolites reflect cell status and unveil functions of associated metabolic pathways. Single cell metabolomics has a great potential to uncover the phenotypic variations from cell to cell and specifically, cellular heterogeneity. In metabolomic studies, mass spectrometry (MS) has become an important tool due to its high sensitivity, broad molecular coverage, and powerful structural identification capabilities. Traditional MS studies rely on bulk samples that do not reveal molecular information at the single cell level and often mask cellular heterogeneity. In contrast, single cell mass spectrometry (SCMS) is capable of profiling metabolites in individual cells and unveiling hidden subpopulations of cells. MS-based single cell metabolomics is capable of analyzing and determining the cellular metabolites that are altered after environmental perturbation.[268] A series of SCMS techniques have been developed to analyze cells under vacuum (e.g., MALDI-MS (matrix-assisted laser desorption/ionization-MS) and SIMS (secondary ion mass spectrometry)[269, 270] or ambient environment (e.g., live single-cell video-MS[99], probe ESI MS[271], LAESI MS[136], and nano-DESI MS[272]). We have developed multiple microscale sampling and ionization devices, including the Single-probe[273], micropipette[112] and T-probe[274], that can be coupled to MS for single cell metabolomics studies. Among them, the Single-probe SCMS method has been routinely used in our studies. Briefly, the Single-probe is a home-built device that can be coupled to a mass spectrometer for microscale sampling (e.g., from single cells and tissue slices) and MS analysis (Figure 5). The Single-probe tip is small enough (~9 μm) for insertion into single cells to extract intracellular analytes, which are immediately ionized by MS

analysis.[232, 250, 273, 275-278] We have used this technique in different single cell studies such as investigating the difference in drug resistance[232, 279], quantifying anticancer drugs in single cells[155, 275, 280, 281], comparing metabolites in cancer stem cells and non-stem cancer cells[282], and determining the influence of the environment on algal cell metabolites[283]. In addition, the Single-probe device has been utilized for MS imaging studies to acquire the spatial distribution of molecules on tissue slices[278, 284-287] as well as to analyze secreted metabolites inside multicellular spheroids.[288]

3.2 Experimental section

3.2.1 Parasite culture

Beta-galactosidase-expressing *T. cruzi* strain Tulahuen (clone C4) were obtained through BEI Resources, NIAID, NIH[289] and maintained in mouse C2C12 myoblasts by once-weekly passaging. Trypomastigotes were collected from culture supernatant and used for infections.

3.2.2 Cell culture

HeLa cells were cultivated in DMEM cell culture medium (Corning) supplemented with 10% iron-supplemented calf serum (HyClone) and 1% penicillin-streptomycin (Gibco) in 5% CO_2 at 37 °C. C2C12 cells were maintained in DMEM media supplemented with 5% iron-supplemented calf serum (HyClone) and 1% penicillin-streptomycin (Invitrogen), in 5% CO_2 and at 37 °C, as previously described[259].

3.2.3 Cell infection and staining

HeLa cells were infected at a host:parasite ratio of 1:10. Two days post-infection, cells were washed with ice-cold PBS and fixed with 0.7% glutaraldehyde for 5 min, fixing and killing the parasites. Cells were then rinsed three times with PBS for 4 min. Cells were then stained overnight with 1 mg/mL of X-Gal in PBS containing 2 mM $MgCl_2$, 4.98 mM potassium ferricyanide and 5.76 mM potassium ferrocyanide,[290] pH 7.3 at 37°C.

3.2.4 Single-probe single cell mass spectrometry (SCMS)

The single-probe SCMS setup includes a Single-probe, a digital microscope, a digital camera, a computer-controlled XYZ-translation stage system (CONEX-MFACC, Newport Co., Irvine, CA, USA) and a Thermo LTQ Orbitrap XL mass spectrometer (Thermo Scientific, Waltham, MA, USA). The fabrication of the Single-probe and the SCMS set-up were detailed in details in our previous studies.[232, 250, 273, 275-278] Briefly, the Single-probe was fabricated using a laser-pulled (P-2000 Micropipette Laser Puller, Sutter Instrument Co., Novato, CA) dual-bore quartz tubing (outer diameter (OD) 50 μm; inner diameter (ID) 127 μm, Friedrich & Dimmock, Inc., Millville, NJ, USA) embedded with a fused silica capillary (OD 105 μm; ID 40 μm, Polymicro Technologies, Phoenix, AZ, USA) in one channel and a nano-ESI emitter, which is produced from the same fused silica capillary, in another channel. The three parts were sealed using UV curing resin (Light Cure Bonding Adhesive, Prime-Dent, Chicago, Il, USA).

Glass coverslips containing cells were washed three times with fresh DMEM and

placed on the XYZ-stage system of the Single-probe SCMS set-up for data acquisition. The targeted single cells were selected for analysis by precisely moving the stage system guided by the microscope. The sampling solvent (50% acetonitrile/50% methanol (v/v)) with 0.1% formic acid) was continuously delivered through the fused silica capillary to extract cellular contents followed by ionization via the nano-ESI emitter and real-time MS analysis. MS experiments were conducted under the following parameters: 200 nL/min flow rate; mass resolution, 60,000; +4.5 kV ionization voltage; 1 microscan; 100 ms max injection time. MS/MS experiments were conducted under the following parameters: 200 nL/min flow rate; mass resolution 60,000; +4.5 kV ionization voltage; 3 microscan; 500 ms max injection time. Collision energies were included in supporting information (Figure S4).

3.2.5 SCMS Data Analysis

SCMS data pretreatment was conducted following our established protocols.[273, 276] MS data were exported with peaks (*m/z* values and relative intensities) generated by Thermo Xcalibur Qual Browser 3.0 (Thermo Scientific, Waltham, MA, USA). The exported raw data was subjected to background and noise subtraction in which all peaks with relative intensity < $3x10^3$ are removed. Background signals derived from organic solvent and cell culture medium were subtracted using an in-house R script as described in our prior work.[274, 291] Normalization of ion intensities to total ion signal (TIC normalization) was subsequently performed. The normalized data was uploaded to *Geena2* online software

(http://proteomics.hsanmartino.it/geena2/geena2_ssi_norm.php)[292] for peak alignment (with a mass tolerance of 10 ppm) and subsequent analysis. *Geena2* parameters were as follows: analysis range from 150 to 1500 *m*/z, maximum number of isotopic replicas: 3, maximum delta between isotopic peaks: 0.01 Da, maximum delta for aligning replicates: 0.01 Da and maximum delta for aligning average spectra: 0.01 Da. After performing peak alignment, missing values (50%) were removed using an in-house Python script (SI Supporting File 1).

Pretreated SCMS data were then imported to Metaboanalyst 5.0[293-297] to perform principal component analysis (PCA), and hierarchical clustering. Random Forest analysis[278] was used to identify misclassified and correctly classified adjacent uninfected cells in comparison to infected cells using an in-house R script (with 500 trees and 7 predictors) (SI Supporting File 2). Then, one-way analysis of variance (ANOVA)[298] was performed with an adjusted p-value cutoff of 0.05 using False Discovery Rate (FDR) correction. The hierarchical clustering heatmap[294] was generated using Ward's minimum variance clustering method and Euclidean distance method, from normalized data with autoscale feature standardization. To minimize the technical variance[232, 299], two replicates were performed for comparison under similar experimental conditions. Boxplots display median, upper and lower quartiles, with whiskers extending to the largest and lowest quartiles and outliers beyond the whiskers represented as dots. Annotations were generated as follows from the combined two replicates' ANOVA test results. 1) Via LC-MS/MS to obtain MS/MS spectra (see below for parameters). 2) Via SC-MS/MS (see above). Annotations

were generated from the resulting SC-MS/MS spectra by spectral comparison to data deposited in METLIN (https://metlin.scripps.edu)[300], HMDB (http://www.hmdb.ca)[301] and GNPS (https://gnps.ucsd.edu/, see Table S3 for parameters)[302, 303].

3.2.6 LC-MS/MS analysis

Metabolites were extracted from uninfected and infected HeLa cells using a two-step extraction with 50% methanol followed by 3:1 dichloromethane-methanol (all Fisher Optima LC-MS grade). Extracts were resuspended in 50% methanol, as in our prior work.[259] LC analysis was performed on a Thermo Vanquish LC equipped with a 1.7 µm Kinetex C18 50 x 2.1 mm column, 100 Å pore size, protected by a SecurityGuard ULTRA C18 Guard Cartridge (Phenomenex). Injection volume was 5 µL. Auto-injector was washed with 10% methanol at a rate of 10 µL/s for 2 seconds. LC gradient was composed of mobile phase A (water + 0.1% formic acid) and mobile phase B (acetonitrile + 0.1% formic acid) at a flow rate of 0.5 mL/min (Table S1). The autosampler was maintained at 10 ℃ and the column compartment at 40 ℃.

MS data were acquired on a Thermo Fisher Q-Exactive Plus hybrid quadrupole orbitrap mass spectrometer operating in positive parallel reaction monitoring (PRM mode, Table S2). Instrument calibration was performed using Thermo Fisher Calmix. All samples underwent a 12.5-minute runtime elution gradient as follows: start at 5% solvent B for one minute, gradual increase to 100% solvent B for eight minutes, hold at 100% solvent B for two minutes, drop to 5% solvent B for 30 seconds, and hold at 5% solvent B for one minute (Table S1). Full PRM parameters were: scan range set

to 100-1,500 *m/z*, default charge state was 1, resolution was 17,500, AGC target set to 2e5, maximum IT was 54 ms, isolation window set to 1 *m/z*, and normalized collision energy increased from 20-60%. MS source parameters were as previously described in[259].

Raw data files were converted to mzXML format using MSConvert.[304]

3.2.7 Data availability

Data from LC-MS (accession number MSV000087656) and SCMS (accession number MSV000089503) have been deposited in MassIVE.

3.3 Results and discussion

In the current study, we focused on metabolomics of single cells infected by *T. cruzi*, due to the crucial role of metabolism in CD.[260, 305] The experiments were conducted using the Single-probe SCMS technique to analyze HeLa cells, which were used as the model system in three different groups: *T. cruzi*-infected, bystander (i.e., uninfected cells that are adjacent to infected cells), and control cells (no parasite exposure). Our results revealed striking bystander effects of infection, including metabolic pathways commonly perturbed in infected cells and bystander cells. These results help improve our understanding of host pathways of CD pathogenesis and may help develop new treatments to address late-stage disease that cannot be cured by antiparasitic agents. Furthermore, our approach is compatible with biosafety protocols and thus should have broad applicability to other intracellular pathogenic agents.

During chronic *T. cruzi* infection, only a minority of cells are infected.[306, 307] Although parasite persistence is required for disease progression[308], CD symptoms can nevertheless develop even with low parasite load that may be spatially disconnected from sites of tissue damage.[309, 310] SCMS analyses of infected and uninfected cells in the same culture plate, in comparison to control wells, can deconvolute direct effects of *T. cruzi* infection from bystander effects of infection. HeLa cells were used as a model and infected with beta-galactosidase-expressing *T. cruzi.*[289] Cells were fixed by glutaraldehyde to kill the parasites and ensure biosafety. The fixed cells were stained by X-gal, enabling us to differentiate parasite-containing cells from bystander cells. The invasion of amastigote stage of parasites can be observed in bright-field microscopic images (Figure 6a), and the infected cells containing amastigotes can be clearly distinguished from the bystander cells. These observations match with previous publications regarding this parasite strain.[311, 312] SCMS measurements were performed not only on these infected and bystander cells, but also on control cells from a separate, uninfected culture well.

PCA (principal component analysis) showed that the fixation and staining processes had no significant influence on the overall cellular metabolite profiles (Figure 6b, S4a). This conclusion was further confirmed ($p = 0.49$ from permutation test) by PLS-DA (partial least squares discriminant analysis) (Figure S4b and S4c). As expected, parasite-containing cells have different overall metabolite compositions compared with bystander cells. However, strikingly, both cell types differed in terms of overall metabolome from control and stained cells (both are uninfected). This finding

supports bystander effects of *T. cruzi* infection on the overall cellular metabolome and provides a metabolic mechanism to explain the development of Chagas disease lesions at sites with low parasite burden.[313]

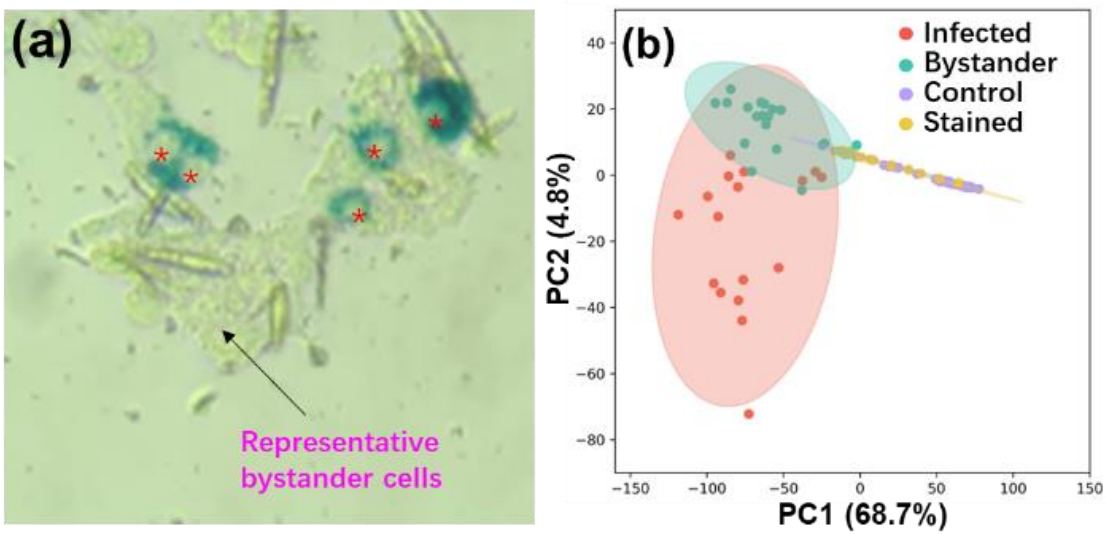

Figure 6 Influence of the optimized fixation and staining processes on the overall profiles of cellular metabolites in HeLa cells infected by T. cruzi. (a) Bright-field microscopy picture of HeLa cells infected with beta-galactosidase-expressing T. cruzi. Cells were fixed by glutaraldehyde and stained by X-gal. Infected cells with intracellular amastigotes T. cruzi (stained as deep blue in an oval shape; indicated by red stars) can be distinguished from bystander cells (adjacent uninfected cells; indicated by a black arrow). (b) PCA results. Without parasite infection, cells have comparable profiles of metabolites without (control) and with (stained) the fixation and staining processes. Cells exposed to parasites (infected and bystander cells) present significantly different metabolite profiles than unexposed cells (control and stained).

PCA results showed that a subset of bystander cells was particularly similar to (i.e., overlapped with) infected cells from the same culture plate (Figure 6b, Figure 7a). Indeed, random forest machine learning algorithms mis-classified 16 out of 53 bystander cells as infected (Table 3). In contrast, 62 out of 68 infected cells were correctly classified. It is worth noting that a large portion of control cells was misclassified as stained cells and vice versa, supporting that fixation and staining processes have no significant influence on cell metabolites. We then manually regrouped the bystander cells into correctly classified and mis-classified subgroups and conducted PCA. We observed a high degree of similarity between the mis-classified and infected cells (Figure 3b). Similar trends were observed from results from hierarchical clustering of metabolites (Figure S1). To determine metabolites with significantly different abundances among the infected and two bystander groups (correctly classified and mis-classified infected cells), we performed ANOVA (with False Discovery Rate (FDR) correction and adjusted p-value ≤ 0.05) (Table S4). We obtained 16 ions from all groups possessing strikingly similar patterns for both mis-classified bystander cells and infected cells across two independent experimental replicates (e.g., lower levels of *m/z* 267.0620, 322.886, and 359.025 compared to correctly-classified bystander cells) (Table S4, Figure S2).

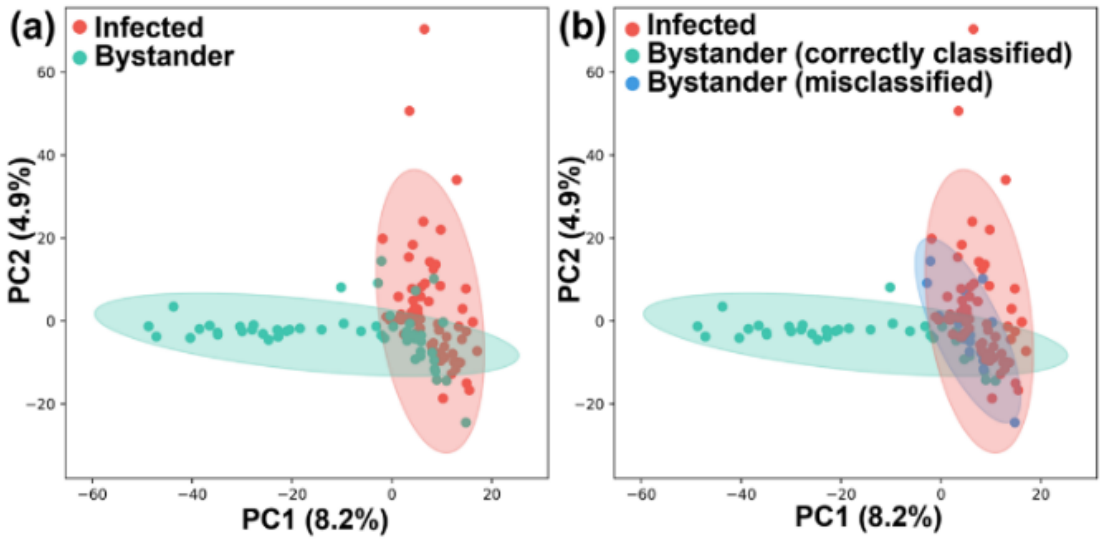

Figure 7 Impact of T. cruzi infection on the metabolome of bystander uninfected cells. (a) PCA of SCMS data highlighting metabolic overlap between T. cruzi infected cells and a subset of bystander cells. (b) PCA analysis of SCMS data as in (a), colored based on random forest classifier prediction. Mis-classified uninfected bystander cells have similar overall metabolomes to infected cells.

Predicted / **Correct**	Control	Stained	Infected	Bystander	Classification error
Control	48	12	1	0	0.213
Stained	25	13	0	0	0.658
Infected	0	1	62	5	0.014
Bystander	3	1	16	33	0.32

Table 3 Random Forest classification of single cells.

To annotate these ions, we performed MS/MS of both single cells (using the Single-probe SCMS method) and cell lysate (using LC-MS/MS). Similar to our

previous studies[232, 299], some species could only be detected in the SCMS experiments, likely due to multiple reasons (e.g., differences in sample preparation methods, matrix compositions, and stabilities of molecules during sample preparation) (Table S4). As expected in untargeted metabolomics[314], most metabolite features could not be annotated (Table S4). Among all annotatable metabolites, *m/z* 756.547 was annotated as PC(34:3), LPC(34:4), or PC(O-34:4) (Table S4, Figure 4). This lipid significantly differed in abundance between cell groups ($p = 2.33x10^{-4}$ using ANOVA test with False Discovery Rate correction (Figure 4a). It is interesting to note that, similar to infected cells, mis-classified bystander cells also contain high abundances of this species (Figure 4a). Other infection-elevated metabolites were also annotated as glycerophosphocholines (GPCs), including *m/z* 768.583, 780.5460, 782.5630, 808.5770 and 810.5940 (Table S4, Figure S3). This observation concurs with our prior findings of infection-elevated GPCs in heart tissue in proportion to disease severity and in the infected esophagus and large intestine, in mice across multiple infection timepoints and parasite strains.[255, 256, 258, 259] While confidently assigning a parasite *vs* host origin to these GPCs is challenging, very long-chain GPCs and lysoglycerophosphocholines (Lyso-GPCs) are elevated in isolated amastigote-stage *T. cruzi* compared to host cells.[315] These findings may support further re-development of therapeutics targeting phosphatidylcholine metabolism, such as miltefosine, currently in clinical use for the related parasite *Leishmania,* but in this case to target the metabolic consequences of infection on the host.[316, 317]

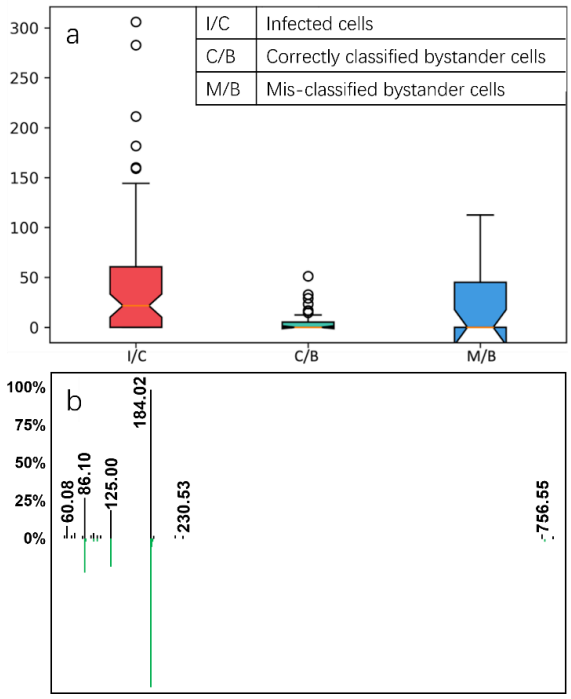

Figure 8 Representative glycerophosphocholine (m/z 756.547) differentiating between cell groups. (a) Normalized intensity of PC(34:3) in three different cell types (p = 0.000233 using ANOVA test with FDR correction). (b) LC-MS/MS mirror plot supporting PC annotation. Green, reference library MS/MS spectrum for 1-Oleoyl-2-palmitoyl-sn-glycero-3-phosphocholine (PC 34:1). Black, experimental MS/MS spectrum for m/z 756.547. M/z 756.547 is smaller by 4.03 to 1-Oleoyl-2-palmitoyl-sn-glycero-3-phosphocholine.

3.4 Conclusion

In conclusion, we used the Single-probe SCMS technique for metabolomics studies of cells with heterogeneous infection by *T. cruzi* at the single-cell level. This represents, to the best of our knowledge, the first implementation of single-cell metabolomics in mammalian-infectious disease. We discovered that necessary cell

fixation (to kill the parasites) and staining (to illustrate *T. cruzi* infection) have no significant influence on the overall cell metabolome (Figure 6b, S4). Our results demonstrate for the first-time bystander effects of *T. cruzi* on infection-adjacent uninfected cells (Figure 6b, Figure 7,Figure 8). Although our current studies cannot fully explain the mechanisms of the bystander effects, it is very likely that the uneven infection was due to the heterogeneity of host cells. The bystander cells may belong to a subpopulation of host cells containing lower levels of glucose, which is needed to support parasites' replication internally. It has been reported that *T. cruzi* amastigotes transport extracellular glucose to fuel their own metabolism and replicate in the host cytosol.[318] In addition, nutritional deficiencies in the host cells will lead the failure of *T. cruzi* infection.[319]

Our results provide a significant insight into CD pathogenesis, explaining lesion development in sites that do not contain parasites.[309, 310] This has major implications for CD treatment, indicating that killing parasites alone may not be sufficient. Our results may explain the failure of Benznidazole Evaluation for Interrupting Trypanosomiasis (BENEFIT) clinical trial[320], and pave the way for future work to assess the role of metabolic heterogeneity in CD pathogenesis, tissue resilience, parasite dormancy and antiparasitic susceptibility.

3.5 Author contribution

Conceptualization, Z.Y., L.-I.M.; methodology, Z.Y., L.-I.M., **Y.L.,** T.D.N., R.L.; sample preparation, S.S.K., L.-I.M., **Y.L.,** T.D.N.; single cell MS and MS/MS analysis, **Y.L.**,

T.D.N.; LC-MS/MS analysis, J.J.H.; data analysis, **Y.L.**, T.D.N.; R and Python script preparation, **Y.L.**; resources, Z.Y., L.-I.M.; writing—original draft preparation, **Y.L.**, T.D.N.; writing—review and editing, L.-I.M., Z.Y., **Y.L.**, T.D.N.

Chapter 4: Quantifying Cell Heterogeneity and Subpopulations Using Single Cell Metabolomics

4.1 Introduction

It has been well accepted that nearly all biological systems are heterogenous[321] due to genetic and phenotypic variances. Even within the isogenic cell populations, cell-to-cell heterogeneity is prevalent, because of stochastic processes in transcription, translation, and metabolism.[322] Uncovering cell heterogeneity is critical for studying fundamental cell biology and human diseases. For example, tumors contain heterogeneous distributions of malignant cells with varied physiological and biological properties.[323] Such cell-to-cell heterogeneity was reported as a result of intrinsic and extrinsic factors,[324] and recognized to play a key function in diseases evolution, drug resistance, and tumor relapse.[325] In particular, cell heterogeneity reflects the effectiveness of cancer treatment and management, because an escape of a small subpopulation of cells, such as circulating tumor cells and cancer stem cells, from drug treatment can cause disease remission.[326]

To date, a variety of single cell studies using different approaches (e.g., flow cytometry,[327] image-based signaling marker colonization,[328] single cell genomics,[328, 329] single cell transcriptomics,[330, 331] single cell western blotting,[332] and single cell metabolomics[333]) have revealed the coexistence of multiple cell subpopulations in the same environment. Among various platforms, single cell RNA-seq quantification[334, 335]

has gained most attraction, likely due to the availability of the instruments (e.g., 10X Genomics[336]) and analytical software packages.[337-340] Although the transcriptomic profiling is informative and powerful, the downstream proteomic or metabolomic responses are still unclear. As metabolites can rapidly and accurately reflect cell status and functions, single cell metabolomics is a promising approach to uncovering cell heterogeneity. Among all analytical techniques, single cell mass spectrometry (SCMS) has become the most popular tool for single cell metabolomics studies.[113, 153, 273, 341-346]

Heterogeneous cells could be grouped into subpopulations with similar biological traits[347, 348] (e.g., morphology,[349] surface marker expression level,[350] and intracellular metabolism[333]). Several SCMS metabolomics studies have been performed to group cells into different sub-groups based on individual characteristic metabolites.[351,352] However, to the best of our knowledge, no methodologies have been reported to use the overall metabolomic profiles of single cells to quantify the changes of cell heterogeneity and the associated cell subpopulations. The absence of relevant work is likely due to two major reasons: (1) the lack of the metrics to quantify cell heterogeneity using the single cell metabolomics profiling data and (2) suitable data analysis approaches that can determine cell subpopulations with minimum artificial bias without prior knowledge of specific subpopulations. In this regard, we report a comprehensive method combining SCMS experimental method with a novel bioinformatics tool to address these challenges.

Metastatic melanoma cancer cell lines have higher drug resistance than primary melanoma cancer cell lines.[353] In this proof-of-concept study, we used two cancer cell lines as models: the primary melanoma (i.e., drug-sensitive cell line) WM115 (Figure S1A) and metastatic melanoma (i.e., drug-resistant cell line) WM266-4 (Figure S1B). Previous studies reported differential expression of genes and global proteins in these two melanoma cell lines to unveil various proteins that are associated with the drug-resistant phenotype.[354] The Single-probe SCMS experimental technique,[225, 232, 273, 282, 283, 355] a homebuilt method for real-time *in situ* data acquisition of live single cells, was combined with a novel bioinformatics tool, SinCHet-MS, for quantitative analysis of cell subpopulations. Briefly, we cultured cancer cells under normal conditions. Cells were attached to glass cover slips during incubation, and then treated by 1 μM vemurafenib, an anticancer drug for melanoma therapy, for 48 h, and then analyzed using the Single-probe SCMS method (Figure 9). Although batch-to-batch variation is commonly recognized in conventional metabolomic studies (e.g., using liquid chromatography (LC)-MS),[356, 357] it is under-appreciated in most SCMS metabolomic analyses. To accurately evaluate the cellular response to microenvironmental stimulus (vemurafenib), we examined the batch-to-batch variation, which is potentially introduced by minor difference in sample preparation and fluctuations of instrument conditions on different days, and thus separating it from biological variance. We performed experiments for both the control (untreated) and treated cells within a batch, and repeated the experiments on a different day for both cell lines (Table S1). We then performed data pre-treatment, including noise removal, background reduction, peak

alignment, and ion intensity normalization, prior to analyses using SinCHet-MS (Figure 9).[358] Built on SinCHet,[359] a computational toolbox with a graphical user interface (GUI) for analyzing single cell mRNA expression and methylation data, we developed SinCHet-MS to analyze SCMS data by devising three crucial features: batch correction, a novel d-statistic for determining default cell subpopulation resolution for further investigation, and the sGF score (Subpopulation Generalized Fisher Product Score) for prioritizing biomarkers defining cell subpopulations.

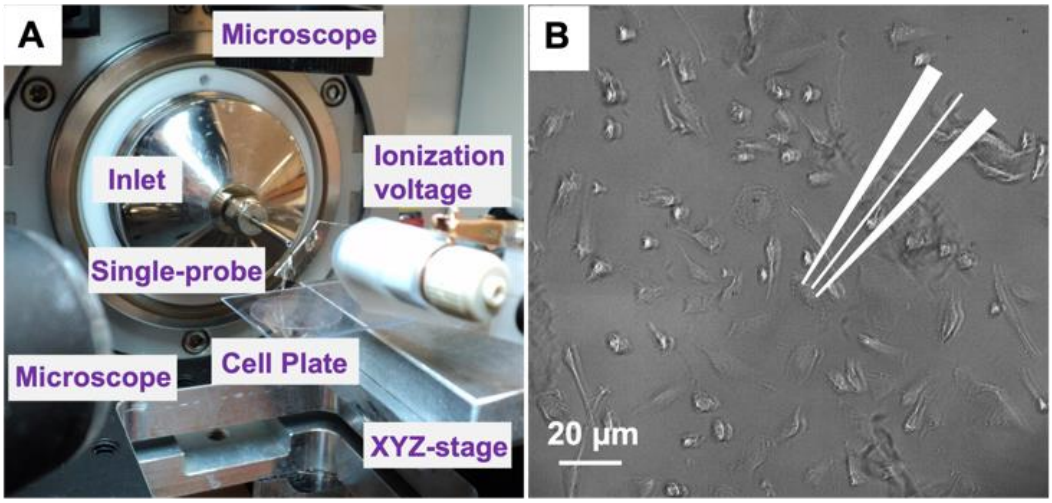

Figure 9 (A) Setup of the Single-probe SCMS experiment. (B) Analyzing a single cell guided by high-resolution microscopes.

4.2 Methods

4.2.1 Cell culture and sample preparation

Human melanoma cell lines, WM-115 and WM-266-4 cells (generously provided by Dr. Yinsheng Wang at the University of California, Riverside) were classified as the primary and metastatic cell lines, respectively, as established from the same

melanoma patient. Cells were subcultured every three (WM-266-4) to five (WM-115) days in Dulbecco's Modified Eagle Medium (Santa Cruz Biotechnology Inc., Dallas, TX) supplemented with 10% fetal bovine serum (FBS, Life Technologies, Grand Island, NY, USA) and 1% penicillin-streptomycin (Life Technologies, Grand Island, NY, USA). Cells were maintained in a cell incubator (HeraCell) at 37 °C in a humidified environment containing 5% CO_2. When cells reached ~ 80% confluence, they were rinsed twice using phosphate buffered saline (PBS) solution followed by trypsinization in the incubator for detachment. Trypsinization was quenched and the cell suspension were then transferred onto a glass cover slip (diameter = 18 mm, VWR International). After overnight incubation, cells were attached to the coverslip, and then transferred to the XYZ-translational stage system (MFA-CC, Newport Co., Irvine, CA, USA) for SCMS experiments. To conduct Vemurafenib treatment, 500 μM Vemurafenib stock solution in dimethyl sulfoxide (DMSO) (>99.9%, MilliporeSigma Co. St. Louis, MO, USA) was prepared and diluted in the complete culture medium at a final concentration of 1 μM. Cells after overnight culture were then treated with 1 μM Vemurafenib solution for a duration of 48 h and maintained in the incubator, followed by washing with fresh culture medium (without FBS) twice to remove residual drug molecules prior to SCMS analysis.

4.2.2 SCMS Experiments

he Single-probe SCMS experiments were performed following our previously published protocols[273], and only a brief description is provided here. A Single-probe

was fabricated by embedding a solvent-providing fused silica capillary (O.D. 105μm; I.D. 40 μm, Polymicro Technologies, Phoenix, AZ) , a nano-ESI emitter (produced from the same fused silica capillary using a butane micro torch) into a dual-bore quartz needle (produced from qual-bore quartz tubing (O.D. 500 μm; I.D. 127 μm, Friedrich & Dimmock, Millville, NJ) using a laser micropipette puller (Sutter P-2000, Sutter Instrument, Novato, CA)). The Single-probe device was coupled to a LTQ Orbitrap XL mass spectrometer (Thermofisher Scientific, San Jose, CA) (Figure 9A). Cells were cultured, attached onto glass coverslip, treated by anticancer drug, and then rinsed by fresh culture medium (no fetal bovine serum). The glass coverslip containing cells was placed onto the XYZ-translational stage (step size = 0.1 μm). Guided by a digital microscope (Shenzhen D&F Co., China), a target cell was selected and penetrated by gradually moving the stage (Figure 9B). Cellular metabolites were extracted by the liquid junction (acetonitrile with 0.1% formic acid) formed at the tip of the Single-probe, and immediately ionized and analyzed. WM-115 and WM-266-4 cells prepared on the same day were randomly selected and analyzed with the MS analysis parameters listed as follows: ionization voltage +4.5 kV, mass range 150–2000, mass resolution 60,000 at m/z 400, 1 microscan, 100 ms max injection time, and automatic gain control (AGC) on.

4.2.3 SCMS data pre-treatment

The obtained SCMS raw datasets of all single cells were accessed using Xcalibur 5.0 (Thermofisher Scientific). Detection of single cells was confirmed from the mass

spectra (including detected ions and their intensities) of common cellular species (e.g., PC (34:1); *m/z* 782.57). Background ions from the sampling solvent and culture medium were subtracted, and the instrument noise (i.e., ions with intensities < 10^3) was removed using an in-house developed software.[358] We normalized ion intensities of each cellular metabolite to the total ion current (TIC) and submitted the datasets to Geena2[292] for peak alignment and isotope grouping. The pre-treated data were submitted to MetaboAnalyst 5.0[297] to select commonly detected species with 50% missing value (i.e., metabolites that can be detected in > 50% of all measured single cells). All datasets were subjected to log2 transformation prior to the downstream analysis.

4.2.4 SinCHet-MS

Built on SinCHet,[359] a bioinformatics toolbox for performing heterogeneity analysis of single cell transcriptomes, we introduced a new tool, SinCHet-MS, for analyzing SCMS data (Figure 9). Details on how to run SinChet-MS were described in the manual (Supporting Information). There are five panels: (1) Input/Output, (2) Data Processing, (3) Heterogeneity Analyses, (4) Subpopulation, and (5) Biomarkers. In "Heterogeneity Analyses", hierarchical cluster analyses were performed to group cells into subpopulations based on the similarities of metabolites' profiles. Clustergram and heatmaps are available for visual examination. The following three novel features of SinCHet-MS:

(1) Batch effect evaluation and removal. In the panel of "Data Processing", we include a function to evaluate and remove potential batch effects. First, principal component

analysis (PCA), an unsupervised dimension reduction method, in “Data Processing” is used to quickly examine potential batch effect and then determine if undesirable batch or technical effect is observed. For instance, if data from different batches are clearly separated in PCA plot, especially when the separation of different batches of cells is observed, say, along the first PC, which means the difference due to batch difference explains the largest variability of the data, while the experimental effect of research interest (e.g., treatment effect) explains less variability of the dataset. In this case, the user could remove this observed undesirable batch effect by selecting Yes from the drop-down option (YES/NO) for debatching. COMBAT,[360] a commonly used debatching method (based on empirical Bayes frameworks), often used in transcriptomic studies, was implemented to remove potential batch effects here.

(2) The *d* statistic. In the ‘Subpopulation’ panel, we introduce a d statistic to determine the default number of clusters for further investigation of subpopulations. The *d* statistic was modified from the *D* statistic defined previously[46]. Briefly, the *D* statistic, quantifies the overall change of heterogeneity before and after treatment, is defined as the areas under the Shannon Profiles (SPs) between two conditions. The *d* statistic is defined as the difference of the Shannon index (H) between two conditions of research interest at the minimum number of clusters with significance estimated using permutation (Equations S1 and S2 in the Supporting Information). It is worth noting that these two statistic methods are different: the D statistic can be perceived as the heterogeneity difference between two conditions considering all possible clustering resolutions, whereas our novel *d* statistic is defined as the difference of the

Shannon index (H) between two conditions at a given clustering resolution of research interest. The default clustering resolution of SinCHet-MS is determined using the minimum number of clusters with the *d* statistic differs significantly between two conditions. SinCHet-MS has the flexibility for users to explore alternative clustering resolutions. The statistical significance is estimated from the permutation test, similar to that reported in our previous publication[359] and described in the Supplemental Equation S2 (Supporting Information).

(3) Subpopulation_Generalized Fisher Product Score (sGF). As implemented in 'BioMarkers' panel, this function can be used to prioritize biomarkers. sGF was devised to summarize the overall difference among cell subpopulations for each metabolite, with the consideration of *p*-values from multiple comparison tests and fold change of pairwise comparison between the subpopulation of interest and any other subpopulation (Supplemental equations S3 and S4 in the Supporting Information). Those metabolites with Benjamini-Hochberg false discover rate (FDR) adjusted *p*-values < 0.05 were regarded as the subpopulational biomarkers.

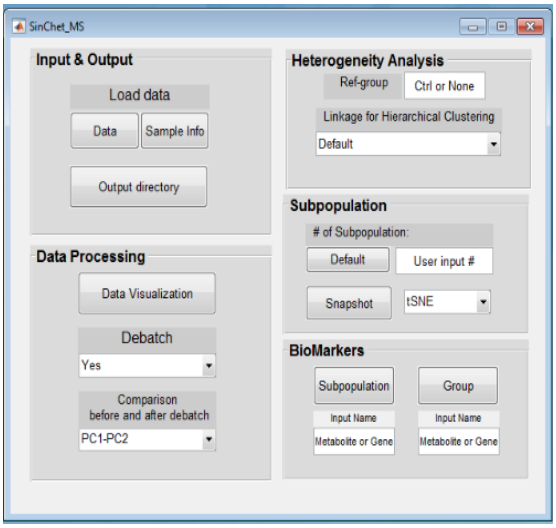

Figure 10 The main Graphic User Interface (GUI) of the SinCHet-MS software

package. This GUI integrates functions of batch correction, determination and visualization of cell subpopulations, and prioritization of subpopulation diagnostic features.

4.3 Results and discussion

In total, we analyzed 75 and 128 cells for WM115 and WM266-4, respectively. The representative mass spectra of single cells (before and after vemurafenib treatment) are shown in Figure S2. Rich metabolomic information can be observed in a mass range of *m/z* 650–950, which encompassed a variety of lipids, along with background ions (e.g., *m/z* = 493.25). Numerous species were detected in each cell. To extract the essential information from all mass spectra, experimental data need to be carefully treated and analyzed.

4.3.1 Batch correction for SCMS datasets

Batch effect may be present in SCMS experiments. Debatching can enhance statistical power by enabling concurrent data analysis across multiple batches obtained under the same experimental condition. We used PCA to visualize cellular metabolomic profiles (for all cells) to evaluate potential batch effect: a significantly different PCA grouping between two batches (i.e., from the same cell line with the same treatment conditions) indicates an evident batch effect. To remove the observed technical batch effect, we performed batch correction, which is integrated in SinCHet-MS based on COMBAT.[360]

Our experimental results indicate that for the sensitive cell line WM115, no significant batch effect was observed (data not shown). For the resistant cell line WM266-4, there is observed batch effect even though the biological differences are larger than the batch effect (Figure 11A). Figure 11B indicated that the debatch functions of SinChet-MS can remove the batch effect for further analysis. However, group separation due to treatment effect was not observed in the first four PC dimensions before and after debatching (Figure 11A vs B; Figure S3A vs S3B). Similar trends can also be observed using box plot (Fig. S4). Such minimum change in cellular profiles agrees with earlier publications reporting higher drug resistance of metastatic melanoma, which corresponds with the hardness of medical therapies for melanoma cancer.[24] As a proof-of-concept study, we demonstrated batch correction of SCMS data, which were acquired from the same passage of cells but with different time of experiments. The batch effect originated from different cell passages needs to be investigated in future studies.

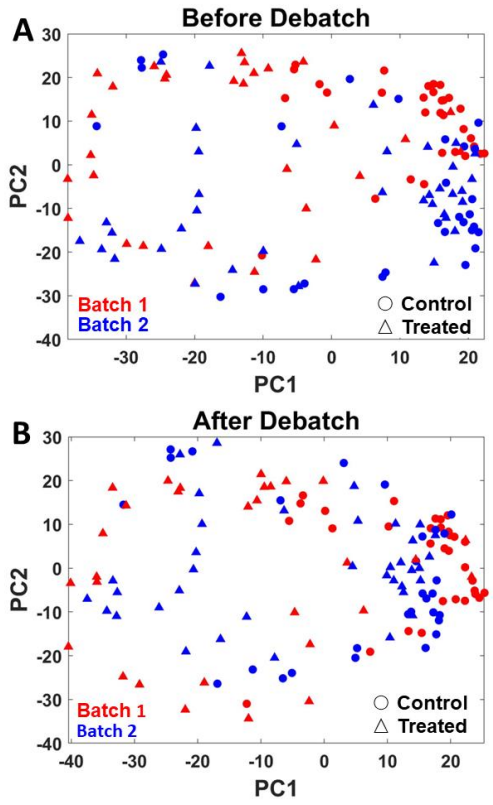

Figure 11 Batch correction. PCA plots of WM266-4 cell lines (A) before and (B) after COMBAT in the PC1 and PC2 dimensions. (Symbols represent control (○) and treatment (∆) groups, and colors represent batch 1 (red) and batch 2 (blue) experiments.)

4.3.2 Quantitative analysis of cell subpopulations and heterogeneity differences

Cellular subpopulations can be reflected from variances of metabolite expression levels and their associated metabolic noise distributions. Previous studies have investigated cell subpopulations by fitting the relative abundances of certain metabolites using probability functions such as normal, lognormal, and gamma distributions.[346, 361] These pioneering studies have demonstrated the possibilities of

using the combined SCMS experiments and statistical data analyses to reveal subpopulations of cells. However, only a limited number of metabolites were selected for analyses, whereas the majority of mass spectra information was not efficiently used. Our previous studies, in which machine learning and SCMS experiments were combined to predict phenotypes of cells, indicate that analyses involving all detected species produced higher reliability than those using selected metabolic biomarkers, which may result in information loss.[232, 355]

For the first time, we performed systematic and quantitative analysis of the changes of subpopulations. In the current study, all detected ions (after pretreatment) were utilized for cell heterogeneity analyses. From SinChet-MS, our results showed that metabolomic heterogeneity was significantly changed by drug treatment in both cell lines ($D = 83.2$, $p < 0.001$ for WM115 (Figure S5A); $D = 54.2$, $p < 0.001$ for WM266-4 (Figure S5B)). When there is no different D (with statistical significance between conditions (i.e., $p \geq 0.05$)), the default number of cell clusters for user investigation is determined using the minimum value of the change points derived from the multivariate adaptive regression splines (MARS) model[359]. In this chapter, the number of subpopulations is determined using the *d* statistics with heterogeneity significantly different between the control and treatment groups ($d = 0.13$, $p < 0.001$ for WM115 (Figure 5A); $d = 0.02$, $p < 0.001$ for WM266-4 (Figure 5B)). The composition of cell subpopulation before and after the treatment were examined and visualized in hierarchical heatmap and pie chart (Figure 12). For the sensitive cell line WM115, there was only one population in the control group; however, a new subpopulation emerged

after treatment (Figure 12A and B). For WM266-4 cells, the number of subpopulation (two) was unchanged, but their relative abundances were altered: ~7:3 and ~3:7 in the control and treatment groups, respectively (Figure 12C and D). The subpopulations of these two cell lines can also be intuitively visualized using tSNE (t-distributed stochastic neighbor embedding) without detailed quantitative information (Figure S6). These findings agreed with published studies reporting an increase in cell heterogeneity upon drug treatment for cancer cell line[24]. In addition, as shown in the representative single cell MS spectra corresponding to each subpopulation (Figure S7), the metabolomic features (*m/z* 650–950) can be visually differentiated.

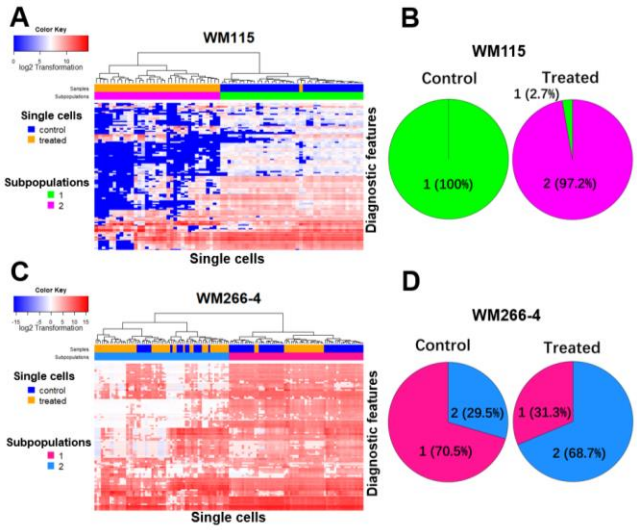

Figure 12 Visualization of subpopulation compositions of control and drug treated single cells before and after drug treatment for (A & B) WM115 and (C & D) WM266-4 cell lines using hierarchical heat map (left column) and pie chart (right column). The determination of cell subpopulation is based on the minimum number of clusters where d statistic indicates significantly different heterogeneity found between control and treatment.

4.3.3 Identification of subpopulational biomarkers

As metabolites reflect cell metabolism, cells in different subgroups likely possess different metabolomic features. For the first time, we identified and prioritized biomarkers for different subpopulations. SinCHet-MS provides three types of GF scores (Generalized Fisher scores): 1) subpopulation GF score (sGF), 2) grouped GF score (gGF), and 3) the widely used GF score as previously described.[359] In the current study, sGF was utilized to prioritize subpopulation diagnostic features. The top three species with the highest sGF, representing significant contributions to the subpopulation discrimination, were visualized among all subpopulations in both cell lines (Figure 13). The diagnostic features with high loadings for the first two PCs were also displayed in the loading plot for each cell line (Figure S8). It is worth noting that, unlike metabolomic biomarkers discovered in conventional LC-MS[362, 363] and other single cell metabolomic studies,[113, 364, 365] the subpopulation biomarkers reported here were based on differences of metabolites' abundances among cell subpopulations, rather than different treatment conditions or types of cells. Based on multiple comparison among subpopulations (FDR < 0.05), we prioritized 95 and 67 subpopulational diagnostic features from WM115 and WM266-4 cells, respectively (Table S2–S3). Further, we conducted MS/MS to identify these diagnostic features using single cells and cell lysates (as detailed in the Supporting Information). As a result, a majority of identified subpopulation biomarkers are cellular lipids (e.g., phosphatidylcholine, phosphatidylethanolamine, diacylglycerol, triacylglycerol) that are related to cellular signal transduction,[366] and their compositions are sensitive to

cells' ambient microenvironment.[367] Through the current proof-of-concept studies, these identified subpopulational biomarkers are likely associated with the emergence, expansion, or reduction of certain cell subpopulations due to change of microenvironment (i.e., drug treatment). However, the correlation between cell subpopulations and drug mechanisms are still to be understood.

4.3.4 Evaluation of technical and biological variation of SCMS datasets

We considered the influence of SCMS technical variation on our analyses. Our previous studies indicated that the technical variation of the Single-probe SCMS method is ~20%, which is determined from the relative standard deviation (RSD) of the ion intensities of standard compound solutions measured using different Single-probe devices.[232] The combined biological and technical variance (RSD = 95%~110%) of cells induced by drug treatment was estimated from the RSD of intensities of the top-121 (WM115) and top-103 (WM266-4) ions due to drug treatment. Similarly, the combined biological and technical variance between different subpopulations (RSD = 75~98%) was also estimated from those 95 (WM115) and 67 (WM266- 4) metabolite biomarkers of subpopulations. Our results indicate that the technical variance is significantly less than the combined biological and technical variance in all cases, indicating the reliability of discovered biomarkers using our method.

4.3.5 Limitations of SCMS datasets

One limitation for this proof-of-concept study is that the sample size is small for the

analysis, primarily due to the limited throughput of the Single-probe SCMS technique. We analyzed a total of 75 WM115 cells (i.e., 31 and 44 cells from batch 1 and 2, respectively) 128 WM266-4 cells (i.e., 62 and 66 cells from batch 1 and 2, respectively). To evaluate if our biological findings shown above are reproducible, we performed the combined analysis (by pooling the data from both batches) and compared the results with those per-batch analyses, performed using the data from each batch separately. The observed agreement (Figure S9 and S10) indicated that findings from per-batch analysis are similar to those from the combined analyses. For sensitive cell line WM115, two subpopulations were identified in batch 1 and batch 2, respectively. Those two subpopulations represent the control and treated groups of cells separately (Figure S9A and S9B), which are the same as those two subpopulations identified in the combined analyses (Figure 12A). In the combined analysis, only one cell from the treatment group was clustered differently from the rest of the cells in the treatment group (Figure 12A). In addition, there are statistically significant correlations of sGF score, which were used to prioritize the subpopulation diagnostic features, between each batch and the combined analysis (Figure S9C). For the resistant cell line WM266-4, even though the proportions of two subpopulations in batch 1 and batch 2 are different (Figure S10A and S10B), their proportions changed by treatment are similar to findings in the combined analysis (Figure 12C and D). Furthermore, there are statistically significant correlations of sGF score of subpopulation biomarkers between analyses by each batch and results from the combined analysis (Figure S10C). In summary, per-batch analysis generated similar conclusions drawn from the combined

analyses. Although the sample size is small, but the observations made between batches were similar.

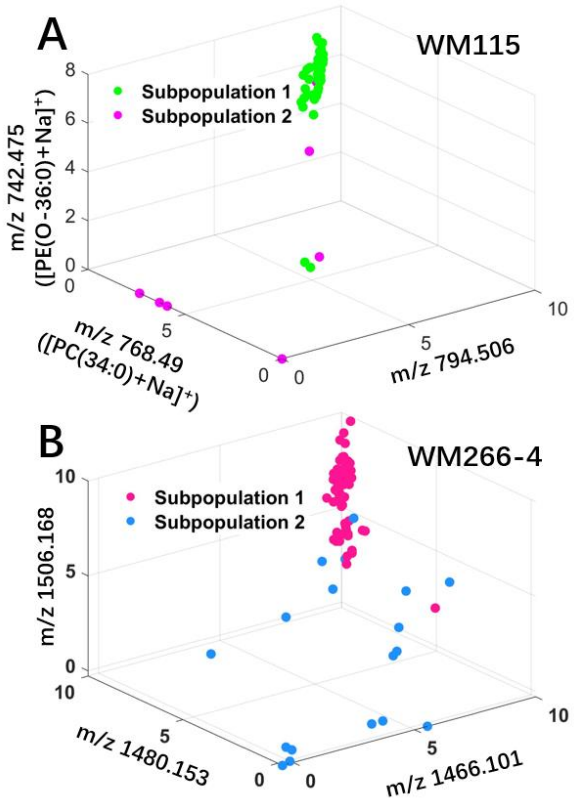

Figure 13 Relative abundances of top-three subpopulation diagnostic features (with top-three highest sGF scores) for (A) WM115 and (B) WM266-4 cell lines. Annotated species were identified through MS/MS analyses.

4.4 Conclusion

In conclusion, for the first time from a metabolomics perspective, we reported a combined experimental and bioinformatic method to reveal changes of cell heterogeneity and quantify subpopulation compositions. Cellular metabolomic profiles of drug-sensitive and drug-resistant cancer cells were measured using the Single-

probe SCMS techniques, and experimental data were subjected to batch correction prior to downstream analysis. Using comprehensive statistical analyses, we revealed that the subpopulations were evidently changed, and a new subpopulation emerged in drug-sensitive primary melanoma cancer cells (WM115) treated with vemurafenib. The emergence of new subpopulations was not clearly observed in the drug-resistant cell line (WM266-4); however, it was evident that proportional change between subpopulations occurred. Although the exact correlation between the determined cell subpopulations and specific cellular biophysical properties of each subpopulation is currently unclear, our technique provides a new label-free method, which is different from traditional targeted approaches (isotope tracing,[368] fluorescent labeling,[64] etc.), to study subpopulations. In addition, we integrated multiple functions for SCMS metabolomic studies, including the batch correction, visualization of cellular metabolomic profiles, comparison of cell heterogeneity, determination of subpopulations, and prioritization of subpopulational biomarkers, in a package with a user-friendly GUI (SinCHet-MS, freely available for non-profit academic use at http://lab.moffitt.org/chen/software/). SinCHet-MS could be applied to analyze single cell metabolomic datasets obtained from different instrument platforms. Profound understanding of cellular metabolism can be gained not only from the cell heterogeneity perspective, but also at the subpopulational resolution.

4.5 Author contribution

Conceptualization, Z.Y., Y.A.C., R.L., J.L.; methodology, Z.Y., Y.A.C., R.L., J.L., **Y.L.**,

T.D.N.; single cell MS and MS/MS analysis, **Y.L.**, T.D.N.; MS data analysis, **Y.L.**, T.D.N.; Python script preparation, **Y.L.**; SinCHet-MS software development and bioinformatic analysis, Y.A.C, J.L.; resources, Z.Y., Y.A.C; manuscript preparation, Z.Y., Y.A.C., R.L., J.L, **Y.L.**, T.D.N.

Chapter 5: Towards Early Monitoring of Chemotherapy-induced Drug Resistance Based on Single Cell Metabolomics: Combining Single-probe Mass Spectrometry with Machine Learning

5.1 Introduction

Chemotherapy is widely acknowledged as a cancer treatment approach, but its effectiveness is limited in the clinic[369]. This is because drug resistance impairs the effectiveness of various chemotherapeutic agents through intricate mechanisms, such as reduced drug uptake, increased cellular detoxification, oncogene mutation, and other mechanisms[369, 370]. Treatment failure and malignancy recurrence are caused by the decreased chemotherapeutic efficacy. There are two main categories of drug resistance: acquired drug resistance, which is defined as resistance that develops and changes in response to treatment pressure, and primary drug resistance, which refers to intrinsic resistance to chemotherapeutics prior to treatment because of genetic and epigenetic factors[371, 372]. Recent data suggested that a combination of the two types may be responsible for the drug resistance seen after chemotherapy.[373, 374] Many methods have been reported to track chemotherapy-induced drug resistance, despite extensive mechanistic research aimed at radically improving our comprehension of drug resistance. These techniques include both established protocols (e.g., clinically applicable imaging-assisted tissue biopsy[375, 376]) and in-development methods (e.g.,

drug monitoring, liquid biopsy, resistance-related protein monitoring, fluorescence-labeled[377] or nanoparticle-bound[378], integral cell response monitoring,[379] real-time monitoring using optofluidic chips[380]). Three significant limitations are still present, though. First, most published methods assess drug resistance based on cell populations, which inevitably loses the molecular details of tumor cell heterogeneity, which plays a crucial role in the development of cancer.[381] Second, most approaches require a long monitoring period (e.g., one[382] to several months[383] after chemotherapy) for consistent results, depending on the kind of drug resistance. This exposes patients to toxicity and ineffective chemotherapy treatment. Third, certain techniques necessitate removing tumor cells from their natural biological milieu, which can change the biophysical and metabolic characteristics of the cells[384] Therefore, new analytical techniques that can track chemotherapy-induced drug resistance in single cancer cells during the early stages of treatment in their native conditions are required.

In order to overcome these constraints, we have previously described a technique that predicts cells with primary drug resistance (i.e., adhesion-mediated drug resistance) prior to drug intervention by combining single cell mass spectrometry (SCMS) experiments with machine learning (ML) data analysis.[355] In the current study, we improved an analytical method to track the various levels of drug resistance that chemotherapy-induced exposure to drugs causes in living cancer cells.

5.2 Methods

5.2.1 SCMS metabolomics and statistical analysis.

In order to extract cellular metabolomic information from the raw data matrix, obtained SCMS metabolomic datasets containing three groups of single cells (control, 10-day, and 20-day drug exposure) underwent a thorough data pre-treatment procedure that included background subtraction, noise removal, intensity normalization, peak alignment, and selection of common species (see "SCMS Data Pre-treatment" in the Supporting Information).[291] After dimensionality reduction using partial least squares-discriminant analysis (PLS-DA) on pre-treated SCMS metabolomic datasets, individual cells' metabolomic profiles in various groups were intuitively displayed in two dimensions[385]. Furthermore, three groups' relative ion intensities of detected cellular species were compared using univariate analysis, such as analysis of variance (ANOVA), and metabolic biomarkers that differ significantly in abundance across all examined groups were found.

5.2.2 Machine learning.

Apart from the logical display of cellular metabolomic profiles through the use of a multivariate approach (PLS-DA), trustworthy mathematical models are essential for tracking drug resistance by forecasting the level of drug resistance (i.e., no, low, or high resistance) that individual cells will possess during chemotherapy. In order to build models that can recognize the underlying patterns in the acquired SCMS datasets and additionally identify drug-resistant cells by analyzing their cellular

metabolomic profiles, we utilized machine learning techniques. Our research employed three machine learning techniques: random forest (RF), which produces the ensemble model's most popular decision, artificial neural network (ANN), which enhances model prediction by changing the network's node and layer configuration, and multinominal penalized (also known as elastic net) logistic regression (LR), which forecasts categorical outcomes by maximizing the likelihood logistic function while minimizing less contributing variables[386]. Conventional untargeted metabolomic research has used RF, ANN, and penalized LR in applications like identification of detected metabolites by liquid chromatography-mass spectrometry (LC-MS) measurements, prediction of chromatographic retention time, and assessment of metabolic changes.[387-389] In this chapter, we constructed a machine learning model using 80% of the single cells that were randomly selected from the obtained SCMS datasets as the training set. The remaining cells were used as the testing set to assess the predictive accuracy. To prevent model bias, each model was assessed using five independent predictions, which were then followed by a 5-fold cross-validation (CV). In An internal script was used for the model's development, validation, and assessment.[390]

The randomForest() function from the R package "randomForest" was used to conduct RF. To put it briefly, the original dataset was supplemented with a response label variable. Eighty percent of the single-cell shuffled data were used for testing, and the remaining twenty percent were used for training. 500 trees were grown in order to create the predictive RF model. The number of variables that were split at each node

(called the "mtry" parameter) was optimized to 7, and other parameters were used by default. Ninety percent of the single cells in the training dataset were chosen at random to train a model. After 100 iterations of this process, the final averaged results were published.

The R package "neuralnet" provided the function neuralnet(), which was used to implement ANN. In short, the ML model (apart from binary classification) in our study was constructed using a multi-label classification approach. As a result, three response label variables were made and added to the original dataset: "None," "Low," and "High." There was only one hidden layer with ten neurons, and the activation function was the "logistic." All parameters, with the exception of "linear.output = FALSE," were used by default. Before ANN modeling, the ion abundance of every identified metabolite in all datasets was pareto-scaled.

Multinominal penalized LR was performed with the 'glmnet' R package. To put it briefly, three response label variables were made and added to the original dataset: "None," "Low," and "High." To train the model, we randomly selected 80% of the cells as the training set, and we used the remaining 20% of the cells as the testing set. All datasets underwent pareto-scaling before the penalized LR modeling, and the model was constructed using default parameters with the exception of alpha = 0.5, which characterizes an elastic net method.

5.3 Results and discussion

5.3.1 Monitoring drug resistance during chemo-treatment using ML models.

In our study, drug resistance was tracked during treatment using RF, ANN, and penalized LR. These models were used to predict the drug resistance levels (i.e., "none," "low," or "high") of individual cells using well-established models. Table 4 presents the prediction accuracy of each model using the confusion matrix. In LC-MS metabolomic studies, our models produced excellent predictive accuracy (97.4% ± 1.8%, 97.4% ± 2.8%, and 97.4% ± 2.3% for the RF, ANN, and penalized LR model, respectively). These models were compared with previously published models, but with comparatively fewer measurements (e.g., ~100)[391, 392]. Our models had less than perfect (100%) predictive accuracy, which may have resulted from cellular responses to the drug pressure that were not all the same. Our findings illustrated the predictive capacity of machine learning models, especially when analyzing minute variations in the cellular metabolomic profiles of various groups. Notably, Welch's two-tail t-test revealed that the three models' predictive accuracies on the testing set were comparable ($p > 0.99$), demonstrating their ability and dependability to track early-stage resistance during treatment at the single cell level.

5.3.2 Model comparison.

Conventional LC-MS metabolomic studies are very interested in metabolic biomarkers, which have been found and used to track drug resistance in many studies

before.[393, 394] We conducted a systematic comparison of the predictive accuracy (i.e., performance) of models using metabolic biomarkers determined by different methods versus models based on SCMS datasets. In other metabolomic research, biomarker discovery has typically relied on a range of criteria (e.g., statistical tests,[128, 240] loading plots of multivariate analysis,[113, 395], or variable importance[396]). ANOVA, principal component analysis loadings, and variable importance (VI) as determined by mean decrease accuracy (MDA)[397], a value signifying a variable's contribution to the group separation (refer to “Model Comparison” in the Supporting Information), were utilized in our investigations to select biomarkers. Various numbers of biomarkers were found using the three above methods: 15 from VI (top-15 metabolites with the highest MDA obtained from the RF model constructed on SCMS datasets), 22 from PCA loadings (metabolites with highest PC1 and PC2 loading scores), and 24 from ANOVA (metabolites with ANOVA p-value < 0.05 and post-hoc p-value < 0.05 between each compared groups).[396] Each dataset has a different number of variables, and the selection criterion has identified some metabolites as biomarkers that are either mutually exclusive or exclusively present. For instance, twenty metabolites were only found under one selection criterion, seven metabolites were mutually recognized as biomarkers by all the criteria, and forty-one metabolites in the SCMS datasets were not selected as biomarkers by any of the criteria.

We then constructed ML models using the RF, ANN, and penalized LR algorithms, utilizing these biomarkers found through various approaches and all metabolites included in the SCMS dataset. Finally, we assessed the performance of these models

(Table 4). Even though different groups of metabolites were used to construct the models, all trained machine learning models generally demonstrated excellent predictive accuracy on the testing set. All together, they showed the potential of our approach to predict drug-resistant cells in a reliable (> 94.9% predictive accuracy) and fast (< 30 s computing time in model construction using pretreated SCMS data) manner. However, ML models based on biomarkers require less computing time than models based on SCMS datasets, most likely as a result of the inclusion of fewer variables.

5.3.3 Multi-class ROC analysis.

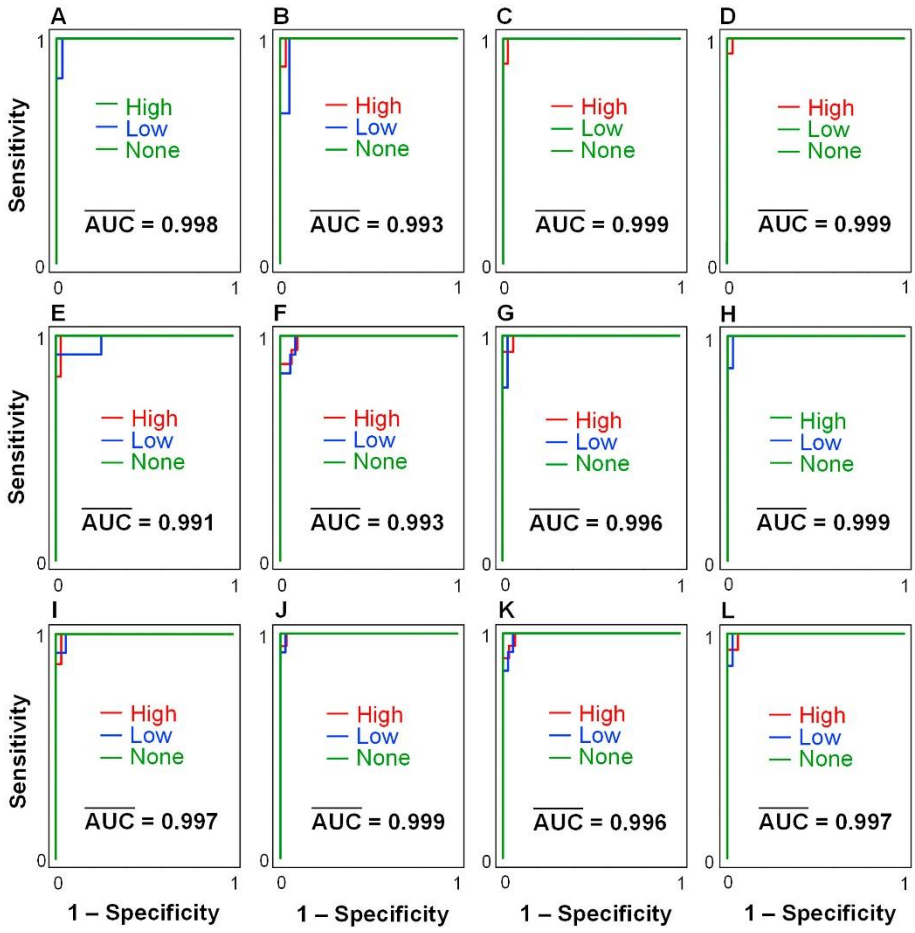

Figure 14 Multi-class ROC analysis of ML models including RF models constructed on

the (A) SCMS datasets, (B) ANOVA subset, (C) PCA loadings subset, (D) variable importance (VI) subset; ANN models constructed on the (E) SCMS datasets, (F) ANOVA subset, (G) PCA loadings subset, (H) VI subset; and penalized LR models constructed on the (I) SCMS datasets, (J) ANOVA subset, (K) PCA loadings subset, (L) VI subset. The model classification ability is represented by the averaged area under curve (AUC) from three pairwise ROC analyses (e.g., “High” *vs.* pooled “Low” and “None”, etc.) in each model.

In LC-MS metabolomic studies, receiver operating characteristic (ROC) analysis was frequently performed for classification models despite the predictive accuracy[386]. The area under the curve (AUC), a complementary performance metric in a diagnostic model, was used to assess the classification capability.[392, 398] To assess the classification ability of various machine learning models, we performed multi-class ROC analysis in our study, which is a generalized version of the conventional binary ROC analysis[399] (Figure 14). An AUC was specifically computed using two sets of data: one group of cells (such as "none") and the other group made up of all remaining cells (such as pooled "Low" and "High"). For the other two cell groups (such as "Low" and "High"), this kind of computation was done once more, and the averaged AUC (i.e., $\bar{}$("AUC")) was the output. Thus, in predicting the cell attributes across all groups, all models demonstrated exceptional[400] classification capability ($\bar{}$("AUC") > 0.99), which is consistent with our previous findings of the excellent model predictive accuracy.

Datasets	Predictive Accuracy	Error Rate	Predictive Accuracy	Error Rate	Predictive Accuracy	Error Rate$_L$

	(RF) *	RF**	(ANN) *	ANN**	(LR) *	R**
SCMS	97.4% ± 1.8%	2.2%	97.4% ± 2.8%	2.1%	97.4% ± 2.3%	3.5%
ANOVA	97.4% ± 1.8%	3.0%	97.4% ± 1.8%	4.3%	98.7% ± 1.2%	3.0%
PCA Loadings	97.9% ± 1.5%	4.3%	95.7% ± 2.6%	5.7%	94.9% ± 2.4%	5.2%
VI	96.2% ± 1.0%	3.5%	98.3% ± 1.8%	1.7%	98.7% ± 1.9%	1.7%

Table 4 Predictive accuracy of RF, ANN and penalized LR models based on SCMS datasets and biomarkers discovered using different criteria.

*Predictive accuracy of single cells possessing no, low and high ADR was calculated from five independent predictions (average ± standard deviation).

**Error rate was estimated using a 5-fold CV in each model.

5.4 Conclusion

We presented an analytical method to track drug resistance in cancer cells after drug exposure that combines single cell metabolomics with machine learning. Models were built using three algorithms: penalized LR, ANN, and RF. The datasets came from the SCMS analysis of cancer cells exposed to drugs and control cells. After building the models, we assessed their performance using a variety of methods, including 5-fold CV, predictive accuracy, and classification capability (i.e., ROC). According to our findings, the RF model built using SCMS datasets could predict individual cells with varying degrees of resistance (i.e., none, low, and high) accurately (86.5%) and quickly (~0.5 s). As a result, other labs could directly use the model for

simple predictions. While in vitro cancer cell lines were used in this chapter, it may be applied to early and real-time monitoring of chemotherapy-induced drug resistance in patient samples, so long as effective malignant cell isolation from clinical specimen is carried out[401], followed by SCMS measurements and machine learning predictions based on a validated model. In addition to our previously published technique for identifying individual cells with primary drug resistance,[355] we showcased new methods based on single cell metabolomics that may be applied to upcoming point-of-care (POC)[402] diagnostic tests in clinical settings.

5.5 Author contribution

Conceptualization, Z.Y., R.L., M.S., G.Z.; methodology, Z.Y., R.L., M.S., G.Z.; single cell MS and MS/MS analysis, M.S.; MS data analysis, R.L., **Y.L.**; Coding script preparation, G.Z., **Y.L.**; resources, Z.Y.; manuscript preparation, Z.Y., R.L., M.S., G.Z., **Y.L.**

References

(1) Kalisky, T.; Quake, S. R. Single-cell genomics. *Nature methods* **2011**, *8* (4), 311-314.

(2) Yan, L.; Yang, M.; Guo, H.; Yang, L.; Wu, J.; Li, R.; Liu, P.; Lian, Y.; Zheng, X.; Yan, J. Single-cell RNA-Seq profiling of human preimplantation embryos and embryonic stem cells. *Nature structural & molecular biology* **2013**, *20* (9), 1131-1139.

(3) Kann, B.; Offerhaus, H. L.; Windbergs, M.; Otto, C. Raman microscopy for cellular investigations—From single cell imaging to drug carrier uptake visualization. *Advanced drug delivery reviews* **2015**, *89*, 71-90.

(4) Schie, I. W.; Huser, T. Methods and applications of Raman microspectroscopy to single-cell analysis. *Applied spectroscopy* **2013**, *67* (8), 813-828.

(5) Wang, D.; Bodovitz, S. Single cell analysis: the new frontier in 'omics'. *Trends in biotechnology* **2010**, *28* (6), 281-290.

(6) Davey, H. M.; Kell, D. B. Flow cytometry and cell sorting of heterogeneous microbial populations: the importance of single-cell analyses. *Microbiological reviews* **1996**, *60* (4), 641-696.

(7) Andersson, H.; van den Berg, A. Microtechnologies and nanotechnologies for single-cell analysis. *Current opinion in biotechnology* **2004**, *15* (1), 44-49.

(8) Schmid, A.; Kortmann, H.; Dittrich, P. S.; Blank, L. M. Chemical and biological single cell analysis. *Current opinion in biotechnology* **2010**, *21* (1), 12-20.

(9) Muzzey, D.; van Oudenaarden, A. Quantitative time-lapse fluorescence microscopy in single cells. *Annual review of cell and developmental biology* **2009**, *25*, 301.

(10) Wang, Q.; Niemi, J.; Tan, C. M.; You, L.; West, M. Image segmentation and dynamic lineage analysis in single-cell fluorescence microscopy. *Cytometry Part A: The Journal of the International Society for Advancement of Cytometry* **2010**, *77* (1), 101-110.

(11) Sandmann, M.; Lippold, M.; Saalfrank, F.; Odika, C. P.; Rohn, S. Multidimensional single-cell analysis based on fluorescence microscopy and automated image analysis. *Analytical and bioanalytical chemistry* **2017**, *409* (16), 4009-4019.

(12) Aldridge, S.; Teichmann, S. A. Single cell transcriptomics comes of age. *Nature Communications* **2020**, *11* (1), 1-4.

(13) Tasic, B.; Menon, V.; Nguyen, T. N.; Kim, T. K.; Jarsky, T.; Yao, Z.; Levi, B.; Gray, L. T.; Sorensen, S. A.; Dolbeare, T. Adult mouse cortical cell taxonomy revealed by single cell transcriptomics. *Nature neuroscience* **2016**, *19* (2), 335-346.

(14) Ormerod, M. G.; Imrie, P. R. Flow cytometry. In *Animal Cell Culture*, Springer, 1990; pp 543-558.

(15) Yin, L.; Zhang, Z.; Liu, Y.; Gao, Y.; Gu, J. Recent advances in single-cell analysis by mass spectrometry. *Analyst* **2019**, *144* (3), 824-845.

(16) Liu, R.; Yang, Z. Single cell metabolomics using mass spectrometry: Techniques and data analysis. *Analytica Chimica Acta* **2021**, *1143*, 124-134.

(17) Zhang, L.; Vertes, A. Single-cell mass spectrometry approaches to explore cellular heterogeneity. *Angewandte Chemie International Edition* **2018**, *57* (17), 4466-4477.

(18) Duncan, K. D.; Fyrestam, J.; Lanekoff, I. Advances in mass spectrometry based single-cell metabolomics. *Analyst* **2019**, *144* (3), 782-793.

(19) Klepárník, K.; Foret, F. Recent advances in the development of single cell analysis—A review. *Analytica chimica acta* **2013**, *800*, 12-21.

(20) Yang, Y.; Huang, Y.; Wu, J.; Liu, N.; Deng, J.; Luan, T. Single-cell analysis by ambient mass spectrometry.

TrAC Trends in Analytical Chemistry **2017**, *90*, 14-26.
(21) Massonnet, P.; Heeren, R. M. A concise tutorial review of TOF-SIMS based molecular and cellular imaging. *Journal of Analytical Atomic Spectrometry* **2019**, *34* (11), 2217-2228.
(22) Buchberger, A. R.; DeLaney, K.; Johnson, J.; Li, L. Mass spectrometry imaging: a review of emerging advancements and future insights. *Analytical chemistry* **2018**, *90* (1), 240.
(23) Bian, Y.; Zheng, R.; Bayer, F. P.; Wong, C.; Chang, Y.-C.; Meng, C.; Zolg, D. P.; Reinecke, M.; Zecha, J.; Wiechmann, S. Robust, reproducible and quantitative analysis of thousands of proteomes by micro-flow LC–MS/MS. *Nature communications* **2020**, *11* (1), 157.
(24) Li, W.; Tse, F. L. Dried blood spot sampling in combination with LC-MS/MS for quantitative analysis of small molecules. *Biomedical Chromatography* **2010**, *24* (1), 49-65.
(25) Ramalingam, P.; Ko, Y. T. A validated LC-MS/MS method for quantitative analysis of curcumin in mouse plasma and brain tissue and its application in pharmacokinetic and brain distribution studies. *Journal of Chromatography B* **2014**, *969*, 101-108.
(26) Ali, A.; Abouleila, Y.; Shimizu, Y.; Hiyama, E.; Emara, S.; Mashaghi, A.; Hankemeier, T. Single-cell metabolomics by mass spectrometry: advances, challenges, and future applications. *TrAC Trends in Analytical Chemistry* **2019**, *120*, 115436.
(27) Tajik, M.; Baharfar, M.; Donald, W. A. Single-cell mass spectrometry. *Trends in Biotechnology* **2022**.
(28) Herzog, R.; Viehböck, F. Ion source for mass spectrography. *Physical Review* **1949**, *76* (6), 855.
(29) Porta Siegel, T.; Hamm, G.; Bunch, J.; Cappell, J.; Fletcher, J. S.; Schwamborn, K. Mass spectrometry imaging and integration with other imaging modalities for greater molecular understanding of biological tissues. *Molecular Imaging and Biology* **2018**, *20*, 888-901.
(30) Lanni, E. J.; Rubakhin, S. S.; Sweedler, J. V. Mass spectrometry imaging and profiling of single cells. *Journal of proteomics* **2012**, *75* (16), 5036-5051.
(31) Liebl, H. Ion microprobe mass analyzer. *Journal of Applied Physics* **1967**, *38* (13), 5277-5283.
(32) Nuñez, J.; Renslow, R.; Cliffll, J. B.; Anderton, C. R. NanoSIMS for biological applications: Current practices and analyses. *Biointerphases* **2018**, *13* (3), 03B301.
(33) Zhang, W.; Xia, X.; Zhang, Y.; Peng, T.; Yang, Q. A novel sample preparation method for ultra-high vacuum (UHV) secondary ion mass spectrometry (SIMS) analysis. *Journal of Analytical Atomic Spectrometry* **2018**, *33* (9), 1559-1563.
(34) Vickerman, J. C.; Briggs, D. ToF-SIMS: surface analysis by mass spectrometry; *IM*, **2001**.
(35) Tian, H.; Sparvero, L. J.; Blenkinsopp, P.; Amoscato, A. A.; Watkins, S. C.; Bayır, H.; Kagan, V. E.; Winograd, N. Secondary - ion mass spectrometry images Cardiolipins and phosphatidylethanolamines at the subcellular level. *Angewandte Chemie International Edition* **2019**, *58* (10), 3156-3161.
(36) Van der Heide, P. Secondary ion mass spectrometry: an introduction to principles and practices; *John Wiley & Sons*, **2014**.
(37) Winograd, N. Gas cluster ion beams for secondary ion mass spectrometry. *Annual review of analytical chemistry* **2018**, *11*, 29-48.
(38) Robinson, M. A.; Graham, D. J.; Castner, D. G. ToF-SIMS Depth Profiling of Cells: z-Correction, 3D Imaging, and Sputter Rate of Individual NIH/3T3 Fibroblasts. *Analytical Chemistry* **2012**, *84* (11), 4880-4885.
(39) Sheng, L.; Cai, L.; Wang, J.; Li, Z.; Mo, Y.; Zhang, S.; Xu, J.-J.; Zhang, X.; Chen, H.-Y. Simultaneous imaging of newly synthesized proteins and lipids in single cell by TOF-SIMS. *International Journal of Mass Spectrometry* **2017**, *421*, 238-244.
(40) Passarelli, M. K.; Winograd, N. Lipid imaging with time-of-flight secondary ion mass spectrometry

(ToF-SIMS). *Biochimica et Biophysica Acta (BBA)-Molecular and Cell Biology of Lipids* **2011**, *1811* (11), 976-990.
(41) Vanbellingen, Q. P.; Castellanos, A.; Rodriguez-Silva, M.; Paudel, I.; Chambers, J. W.; Fernandez-Lima, F. A. Analysis of Chemotherapeutic Drug Delivery at the Single Cell Level Using 3D-MSI-TOF-SIMS. *Journal of the American Society for Mass Spectrometry* **2016**, *27* (12), 2033-2040.
(42) Behrens, S.; Kappler, A.; Obst, M. Linking environmental processes to the in situ functioning of microorganisms by high-resolution secondary ion mass spectrometry (NanoSIMS) and scanning transmission X-ray microscopy (STXM). *Environmental Microbiology* **2012**, *14* (11), 2851-2869.
(43) Kopp, C.; Wisztorski, M.; Revel, J.; Mehiri, M.; Dani, V.; Capron, L.; Carette, D.; Fournier, I.; Massi, L.; Mouajjah, D. MALDI-MS and NanoSIMS imaging techniques to study cnidarian–dinoflagellate symbioses. *Zoology* **2015**, *118* (2), 125-131.
(44) Lodding, A.; Odelius, H. Applications of SIMS in interdisciplinary materials characterization. In *Progress in Materials Analysis: Vol. 1*, 1983; Springer: pp 21-49.
(45) Angerer, T. B.; Blenkinsopp, P.; Fletcher, J. S. High energy gas cluster ions for organic and biological analysis by time-of-flight secondary ion mass spectrometry. *International Journal of Mass Spectrometry* **2015**, *377*, 591-598.
(46) Cillero-Pastor, B.; Eijkel, G.; Kiss, A.; Blanco, F. J.; Heeren, R. M. Time-of-flight secondary ion mass spectrometry-based molecular distribution distinguishing healthy and osteoarthritic human cartilage. *Analytical chemistry* **2012**, *84* (21), 8909-8916.
(47) Walther, F.; Koerver, R.; Fuchs, T.; Ohno, S.; Sann, J.; Rohnke, M.; Zeier, W. G.; Janek, J. r. Visualization of the interfacial decomposition of composite cathodes in argyrodite-based all-solid-state batteries using time-of-flight secondary-ion mass spectrometry. *Chemistry of Materials* **2019**, *31* (10), 3745-3755.
(48) Haase, A.; Arlinghaus, H. F.; Tentschert, J.; Jungnickel, H.; Graf, P.; Mantion, A.; Draude, F.; Galla, S.; Plendl, J.; Goetz, M. E. Application of laser postionization secondary neutral mass spectrometry/time-of-flight secondary ion mass spectrometry in nanotoxicology: visualization of nanosilver in human macrophages and cellular responses. *ACS nano* **2011**, *5* (4), 3059-3068.
(49) Brunelle, A.; Touboul, D.; Laprévote, O. Biological tissue imaging with time-of-flight secondary ion mass spectrometry and cluster ion sources. *Journal of mass spectrometry* **2005**, *40* (8), 985-999.
(50) Mayerhofer, K. E.; Heier, J.; Maniglio, Y.; Keller, B. A. Three dimensional analysis of self-structuring organic thin films using time-of-flight secondary ion mass spectrometry. *Thin solid films* **2011**, *519* (18), 6183-6189.
(51) Veith, L.; Böttner, J.; Vennemann, A.; Breitenstein, D.; Engelhard, C.; Meijer, J.; Estrela-Lopis, I.; Wiemann, M.; Hagenhoff, B. Detection of ZrO2 Nanoparticles in Lung Tissue Sections by Time-of-Flight Secondary Ion Mass Spectrometry and Ion Beam Microscopy. *Nanomaterials* **2018**, *8* (1), 44.
(52) Gulin, A.; Nadtochenko, V.; Solodina, A.; Pogorelova, M.; Panait, A.; Pogorelov, A. A novel approach for 3D reconstruction of mice full-grown oocytes by time-of-flight secondary ion mass spectrometry. *Analytical and bioanalytical chemistry* **2020**, *412* (2), 311-319.
(53) Passarelli, M. K.; Newman, C. F.; Marshall, P. S.; West, A.; Gilmore, I. S.; Bunch, J.; Alexander, M. R.; Dollery, C. T. Single-cell analysis: visualizing pharmaceutical and metabolite uptake in cells with label-free 3D mass spectrometry imaging. *Analytical chemistry* **2015**, *87* (13), 6696-6702.
(54) Vaidyanathan, S.; Fletcher, J. S.; Goodacre, R.; Lockyer, N. P.; Micklefield, J.; Vickerman, J. C. Subsurface Biomolecular Imaging of Streptomyces coelicolor Using Secondary Ion Mass Spectrometry. *Analytical Chemistry* **2008**, *80* (6), 1942-1951.
(55) Fletcher, J. S.; Lockyer, N. P.; Vickerman, J. C. Developments in molecular SIMS depth profiling and 3D

imaging of biological systems using polyatomic primary ions. *Mass Spectrometry Reviews* **2011**, *30* (1), 142-174.
(56) Mao, D.; Wucher, A.; Brenes, D. A.; Lu, C.; Winograd, N. Cluster Secondary Ion Mass Spectrometry and the Temperature Dependence of Molecular Depth Profiles. *Analytical Chemistry* **2012**, *84* (9), 3981-3989.
(57) Seah, M. P.; Havelund, R.; Gilmore, I. S. SIMS of Delta Layers in Organic Materials: Amount of Substance, Secondary Ion Species, Matrix Effects, and Anomalous Structures in Argon Gas Cluster Depth Profiles. *The Journal of Physical Chemistry C* **2016**, *120* (46), 26328-26335.
(58) Breuer, L.; Popczun, N. J.; Wucher, A.; Winograd, N. Reducing the Matrix Effect in Molecular Secondary Ion Mass Spectrometry by Laser Post-Ionization. *The Journal of Physical Chemistry C* **2017**, *121* (36), 19705-19715.
(59) Anderton, C. R.; Gamble, L. J. Secondary ion mass spectrometry imaging of tissues, cells, and microbial systems. *Microscopy today* **2016**, *24* (2), 24-31.
(60) Oehler, D. Z.; Cady, S. L. Biogenicity and syngeneity of organic matter in ancient sedimentary rocks: recent advances in the search for evidence of past life. *Challenges* **2014**, *5* (2), 260-283.
(61) Levenson, R. M.; Borowsky, A. D.; Angelo, M. Immunohistochemistry and mass spectrometry for highly multiplexed cellular molecular imaging. *Laboratory Investigation* **2015**, *95* (4), 397-405.
(62) Fong, L. G.; Young, S. G.; Beigneux, A. P.; Bensadoun, A.; Oberer, M.; Jiang, H.; Ploug, M. GPIHBP1 and plasma triglyceride metabolism. *Trends in Endocrinology & Metabolism* **2016**, *27* (7), 455-469.
(63) Marchant, H. K.; Mohr, W.; Kuypers, M. M. Recent advances in marine N-cycle studies using 15N labeling methods. *Current opinion in biotechnology* **2016**, *41*, 53-59.
(64) Li, Q.; Chen, P.; Fan, Y.; Wang, X.; Xu, K.; Li, L.; Tang, B. Multicolor Fluorescence Detection-Based Microfluidic Device for Single-Cell Metabolomics: Simultaneous Quantitation of Multiple Small Molecules in Primary Liver Cells. *Anal Chem* **2016**, *88* (17), 8610-8616.
(65) Honig, R.; Woolston, J. Laser-induced emission of electrons, ions, and neutral atoms from solid surfaces. *Applied Physics Letters* **1963**, *2* (7), 138-139.
(66) Karas, M.; Hillenkamp, F. Laser desorption ionization of proteins with molecular masses exceeding 10,000 daltons. *Analytical chemistry* **1988**, *60* (20), 2299-2301.
(67) Tanaka, K.; Waki, H.; Ido, Y.; Akita, S.; Yoshida, Y.; Yoshida, T.; Matsuo, T. Protein and polymer analyses up to m/z 100 000 by laser ionization time-of-flight mass spectrometry. *Rapid communications in mass spectrometry* **1988**, *2* (8), 151-153.
(68) Darie-Ion, L.; Whitham, D.; Jayathirtha, M.; Rai, Y.; Neagu, A.-N.; Darie, C. C.; Petre, B. A. Applications of MALDI-MS/MS-based proteomics in biomedical research. *Molecules* **2022**, *27* (19), 6196.
(69) Jiménez, C. R.; Burlingame, A. L. Ultramicroanalysis of peptide profiles in biological samples using MALDI mass spectrometry. *Nephron Experimental Nephrology* **1998**, *6* (5), 421-428.
(70) Li, L.; Garden, R. W.; Romanova, E. V.; Sweedler, J. V. In Situ Sequencing of Peptides from Biological Tissues and Single Cells Using MALDI− PSD/CID Analysis. *Analytical Chemistry* **1999**, *71* (24), 5451-5458.
(71) Garden, R. W.; Moroz, L. L.; Moroz, T. P.; Shippy, S. A.; Sweedler, J. V. Excess salt removal with matrix rinsing: direct peptide profiling of neurons from marine invertebrates using matrix-assisted laser desorption/ionization time-of-flight mass spectrometry. *Journal of mass spectrometry* **1996**, *31* (10), 1126-1130.
(72) Peterson, D. S. Matrix-free methods for laser desorption/ionization mass spectrometry. *Mass spectrometry reviews* **2007**, *26* (1), 19-34.
(73) Keller, C.; Maeda, J.; Jayaraman, D.; Chakraborty, S.; Sussman, M. R.; Harris, J. M.; Ané, J.-M.; Li, L.

Comparison of vacuum MALDI and AP-MALDI platforms for the mass spectrometry imaging of metabolites involved in salt stress in Medicago truncatula. *Frontiers in plant science* **2018**, *9*, 1238.
(74) Mandal, A.; Singha, M.; Addy, P. S.; Basak, A. Laser desorption ionization mass spectrometry: Recent progress in matrix-free and label-assisted techniques. *Mass spectrometry reviews* **2019**, *38* (1), 3-21.
(75) Doroshenko, V. M.; Laiko, V. V.; Taranenko, N. I.; Berkout, V. D.; Lee, H. S. Recent developments in atmospheric pressure MALDI mass spectrometry. *International Journal of Mass Spectrometry* **2002**, *221* (1), 39-58.
(76) Karas, M.; Bachmann, D.; Hillenkamp, F. Influence of the wavelength in high-irradiance ultraviolet laser desorption mass spectrometry of organic molecules. *Analytical chemistry* **1985**, *57* (14), 2935-2939.
(77) Ellis, S.; Soltwisch, J.; Paine, M.; Dreisewerd, K.; Heeren, R. Laser post-ionisation combined with a high resolving power orbitrap mass spectrometer for enhanced MALDI-MS imaging of lipids. *Chemical Communications* **2017**, *53* (53), 7246-7249.
(78) Neumann, E. K.; Comi, T. J.; Rubakhin, S. S.; Sweedler, J. V. Lipid heterogeneity between astrocytes and neurons revealed by single - cell MALDI - MS combined with immunocytochemical classification. *Angewandte Chemie* **2019**, *131* (18), 5971-5975.
(79) Heaton, C.; Bury, C. S.; Patel, E.; Bradshaw, R.; Wulfert, F.; Heeren, R. M.; Cole, L.; Marchant, L.; Denison, N.; McColm, R. Investigating sex determination through MALDI MS analysis of peptides and proteins in natural fingermarks through comprehensive statistical modelling. *Forensic Chemistry* **2020**, *20*, 100271.
(80) Xu, H.; Liu, M.; Huang, X.; Min, Q.; Zhu, J.-J. Multiplexed quantitative MALDI MS approach for assessing activity and inhibition of protein kinases based on postenrichment dephosphorylation of phosphopeptides by metal–organic framework-templated porous CeO2. *Analytical chemistry* **2018**, *90* (16), 9859-9867.
(81) Drzeżdżon, J.; Jacewicz, D.; Sielicka, A.; Chmurzyński, L. MALDI-MS for polymer characterization–recent developments and future prospects. *TrAC Trends in Analytical Chemistry* **2019**, *115*, 121-128.
(82) Dreisewerd, K. The desorption process in MALDI. *Chemical reviews* **2003**, *103* (2), 395-426.
(83) Chu, K. Y.; Lee, S.; Tsai, M.-T.; Lu, I.-C.; Dyakov, Y. A.; Lai, Y. H.; Lee, Y.-T.; Ni, C.-K. Thermal proton transfer reactions in ultraviolet matrix-assisted laser desorption/ionization. *Journal of The American Society for Mass Spectrometry* **2014**, *25* (3), 310-318.
(84) Niehaus, M.; Soltwisch, J.; Belov, M.; Dreisewerd, K. Transmission-mode MALDI-2 mass spectrometry imaging of cells and tissues at subcellular resolution. *Nature methods* **2019**, *16* (9), 925-931.
(85) Han, S. Y.; Lee, T. G.; Moon, D. W. Mass spectrometric method for matrix-free laser desorption/ionization of self-assembled monolayers. Google Patents: 2011.
(86) Wei, J.; Buriak, J. M.; Siuzdak, G. Desorption–ionization mass spectrometry on porous silicon. *Nature* **1999**, *399* (6733), 243-246.
(87) König, S. Target coatings and desorption surfaces in biomolecular MALDI-MS. *Proteomics* **2008**, *8* (4), 706-714.
(88) Lin, Y.-S.; Chen, Y.-C. Laser desorption/ionization time-of-flight mass spectrometry on sol– gel-derived 2, 5-dihydroxybenzoic acid film. *Analytical chemistry* **2002**, *74* (22), 5793-5798.
(89) Piret, G.; Drobecq, H.; Coffinier, Y.; Melnyk, O.; Boukherroub, R. Matrix-free laser desorption/ionization mass spectrometry on silicon nanowire arrays prepared by chemical etching of crystalline silicon. *Langmuir* **2010**, *26* (2), 1354-1361.
(90) Seino, T.; Sato, H.; Yamamoto, A.; Nemoto, A.; Torimura, M.; Tao, H. Matrix-free laser desorption/ionization-mass spectrometry using self-assembled germanium nanodots. *Analytical chemistry* **2007**, *79* (13), 4827-4832.

(91) Addy, P. S.; Bhattacharya, A.; Mandal, S. M.; Basak, A. Label-assisted laser desorption/ionization mass spectrometry (LA-LDI-MS): an emerging technique for rapid detection of ubiquitous cis-1, 2-diol functionality. *RSC advances* **2014**, *4* (87), 46555-46560.
(92) Mandal, A.; Das, A. K.; Basak, A. Label-assisted laser desorption/ionization mass spectrometry (LA-LDI-MS): use of pyrene aldehyde for detection of biogenic amines, amino acids and peptides. *RSC advances* **2015**, *5* (129), 106912-106917.
(93) Hölscher, D.; Shroff, R.; Knop, K.; Gottschaldt, M.; Crecelius, A.; Schneider, B.; Heckel, D. G.; Schubert, U. S.; Svatoš, A. Matrix-free UV-laser desorption/ionization (LDI) mass spectrometric imaging at the single-cell level: Distribution of secondary metabolites of Arabidopsis thaliana and Hypericum species. *The Plant Journal* **2009**, *60* (5), 907-918.
(94) Le Pogam, P.; Schinkovitz, A.; Legouin, B.; Le Lamer, A.-C.; Boustie, J.; Richomme, P. Matrix-free UV-laser desorption ionization mass spectrometry as a versatile approach for accelerating dereplication studies on lichens. *Analytical chemistry* **2015**, *87* (20), 10421-10428.
(95) Baumeister, T. U.; Vallet, M.; Kaftan, F.; Svatoš, A.; Pohnert, G. Live single-cell metabolomics with matrix-free laser/desorption ionization mass spectrometry to address microalgal physiology. *Frontiers in Plant Science* **2019**, *10*, 172.
(96) Masujima, T. Visualized single cell dynamics and analysis of molecular tricks. *Analytica chimica acta* **1999**, *400* (1-3), 33-43.
(97) Mizuno, H.; Tsuyama, N.; Harada, T.; Masujima, T. Live single-cell video-mass spectrometry for cellular and subcellular molecular detection and cell classification. *Journal of mass spectrometry* **2008**, *43* (12), 1692-1700.
(98) Lorenzo Tejedor, M.; Mizuno, H.; Tsuyama, N.; Harada, T.; Masujima, T. Direct single-cell molecular analysis of plant tissues by video mass spectrometry. *Analytical Sciences* **2009**, *25* (9), 1053-1055.
(99) Masujima, T. Live Single-cell Mass Spectrometry. *Analytical Sciences* **2009**, *25* (8), 953-960.
(100) Ali, A.; Abouleila, Y.; Amer, S.; Furushima, R.; Emara, S.; Equis, S.; Cotte, Y.; Masujima, T. Quantitative live single-cell mass spectrometry with spatial evaluation by three-dimensional holographic and tomographic laser microscopy. *Analytical Sciences* **2016**, *32* (2), 125-127.
(101) Esaki, T.; Masujima, T. Fluorescence probing live single-cell mass spectrometry for direct analysis of organelle metabolism. *Analytical Sciences* **2015**, *31* (12), 1211-1213.
(102) Fujita, H.; Esaki, T.; Masujima, T.; Hotta, A.; Kim, S. H.; Noji, H.; Watanabe, T. M. Comprehensive chemical secretory measurement of single cells trapped in a micro-droplet array with mass spectrometry. *Rsc Advances* **2015**, *5* (22), 16968-16971.
(103) Zhang, L.; Foreman, D. P.; Grant, P. A.; Shrestha, B.; Moody, S. A.; Villiers, F.; Kwak, J. M.; Vertes, A. In Situ metabolic analysis of single plant cells by capillary microsampling and electrospray ionization mass spectrometry with ion mobility separation. *Analyst* **2014**, *139* (20), 5079-5085.
(104) Zhang, L.; Vertes, A. Energy charge, redox state, and metabolite turnover in single human hepatocytes revealed by capillary microsampling mass spectrometry. *Analytical chemistry* **2015**, *87* (20), 10397-10405.
(105) Zhang, L.; Khattar, N.; Kemenes, I.; Kemenes, G.; Zrinyi, Z.; Pirger, Z.; Vertes, A. Subcellular peptide localization in single identified neurons by capillary microsampling mass spectrometry. *Scientific reports* **2018**, *8* (1), 1-10.
(106) Gholipour, Y.; Nonami, H.; Erra-Balsells, R. Application of pressure probe and UV-MALDI-TOF MS for direct analysis of plant underivatized carbohydrates in subpicoliter single-cell cytoplasm extract. *Journal of the American Society for Mass Spectrometry* **2008**, *19* (12), 1841-1848.
(107) Gholipour, Y.; Erra-Balsells, R.; Nonami, H. In situ pressure probe sampling and UV-MALDI MS for

profiling metabolites in living single cells. *Mass Spectrometry* **2012**, *1* (1), A0003-A0003.
(108) Gholipour, Y.; Erra-Balsells, R.; Hiraoka, K.; Nonami, H. Living cell manipulation, manageable sampling, and shotgun picoliter electrospray mass spectrometry for profiling metabolites. *Analytical Biochemistry* **2013**, *433* (1), 70-78.
(109) Nonami, H.; Boyer, J. S. Wall extensibility and cell hydraulic conductivity decrease in enlarging stem tissues at low water potentials. *Plant Physiology* **1990**, *93* (4), 1610-1619.
(110) Kajiyama, S. i.; Harada, K.; Fukusaki, E.; Kobayashi, A. Single cell-based analysis of torenia petal pigments by a combination of ArF excimer laser micro sampling and nano-high performance liquid chromatography (HPLC)–mass spectrometry. *Journal of bioscience and bioengineering* **2006**, *102* (6), 575-578.
(111) Izumi, Y.; Kajiyama, S. i.; Nakamura, R.; Ishihara, A.; Okazawa, A.; Fukusaki, E.; Kanematsu, Y.; Kobayashi, A. High-resolution spatial and temporal analysis of phytoalexin production in oats. *Planta* **2009**, *229*, 931-943.
(112) Zhu, Y.; Wang, W.; Yang, Z. Combining Mass Spectrometry with Paternò–Büchi Reaction to Determine Double-Bond Positions in Lipids at the Single-Cell Level. *Analytical chemistry* **2020**, *92* (16), 11380-11387.
(113) Liu, R.; Pan, N.; Zhu, Y.; Yang, Z. T-probe: an integrated microscale device for online in situ single cell analysis and metabolic profiling using mass spectrometry. *Analytical chemistry* **2018**, *90* (18), 11078-11085.
(114) Zhu, Y.; Liu, R.; Yang, Z. Redesigning the T-probe for mass spectrometry analysis of online lysis of non-adherent single cells. *Analytica chimica acta* **2019**, *1084*, 53-59.
(115) Reyes-Garces, N.; Gionfriddo, E.; Gómez-Ríos, G. A.; Alam, M. N.; Boyacı, E.; Bojko, B.; Singh, V.; Grandy, J.; Pawliszyn, J. Advances in solid phase microextraction and perspective on future directions. *Analytical chemistry* **2017**, *90* (1), 302-360.
(116) Prosen, H.; Zupančič-Kralj, L. Solid-phase microextraction. *TrAC Trends in Analytical Chemistry* **1999**, *18* (4), 272-282.
(117) Sarafraz-Yazdi, A.; Amiri, A. Liquid-phase microextraction. *TrAC Trends in Analytical Chemistry* **2010**, *29* (1), 1-14.
(118) Liu, Y.; Shang, Y.; Ma, Q. Microextraction for ambient ionization mass spectrometry analysis. *Advances in Sample Preparation* **2022**, *3*, 100029.
(119) Deng, J.; Yang, Y.; Xu, M.; Wang, X.; Lin, L.; Yao, Z.-P.; Luan, T. Surface-coated probe nanoelectrospray ionization mass spectrometry for analysis of target compounds in individual small organisms. *Analytical chemistry* **2015**, *87* (19), 9923-9930.
(120) Deng, J.; Li, W.; Yang, Q.; Liu, Y.; Fang, L.; Guo, Y.; Guo, P.; Lin, L.; Yang, Y.; Luan, T. Biocompatible surface-coated probe for in vivo, in situ, and microscale lipidomics of small biological organisms and cells using mass spectrometry. *Analytical chemistry* **2018**, *90* (11), 6936-6944.
(121) Deng, J.; Yang, Y.; Liu, Y.; Fang, L.; Lin, L.; Luan, T. Coupling Paternò-Bu¨chi Reaction with Surface-Coated Probe Nanoelectrospray Ionization Mass Spectrometry for In Vivo and Microscale Profiling of Lipid C═ C Location Isomers in Complex Biological Tissues. *Analytical chemistry* **2019**, *91* (7), 4592-4599.
(122) Hiraoka, K.; Nishidate, K.; Mori, K.; Asakawa, D.; Suzuki, S. Development of probe electrospray using a solid needle. *Rapid Communications in Mass Spectrometry: An International Journal Devoted to the Rapid Dissemination of Up-to-the-Minute Research in Mass Spectrometry* **2007**, *21* (18), 3139-3144.
(123) Gong, X.; Zhao, Y.; Cai, S.; Fu, S.; Yang, C.; Zhang, S.; Zhang, X. Single cell analysis with probe ESI-mass spectrometry: detection of metabolites at cellular and subcellular levels. *Analytical chemistry* **2014**, *86* (8), 3809-3816.
(124) Yu, Z.; Chen, L. C.; Ninomiya, S.; Mandal, M. K.; Hiraoka, K.; Nonami, H. Piezoelectric inkjet assisted

rapid electrospray ionization mass spectrometric analysis of metabolites in plant single cells via a direct sampling probe. *Analyst* **2014**, *139* (22), 5734-5739.
(125) Laskin, J.; Heath, B. S.; Roach, P. J.; Cazares, L.; Semmes, O. J. Tissue imaging using nanospray desorption electrospray ionization mass spectrometry. *Analytical chemistry* **2012**, *84* (1), 141-148.
(126) Bergman, H.-M.; Lanekoff, I. Profiling and quantifying endogenous molecules in single cells using nano-DESI MS. *Analyst* **2017**, *142* (19), 3639-3647.
(127) Zhang, X.-C.; Wei, Z.-W.; Gong, X.-Y.; Si, X.-Y.; Zhao, Y.-Y.; Yang, C.-D.; Zhang, S.-C.; Zhang, X.-R. Integrated droplet-based microextraction with ESI-MS for removal of matrix interference in single-cell analysis. *Scientific reports* **2016**, *6* (1), 1-9.
(128) Zhang, X.-C.; Zang, Q.; Zhao, H.; Ma, X.; Pan, X.; Feng, J.; Zhang, S.; Zhang, R.; Abliz, Z.; Zhang, X. Combination of droplet extraction and Pico-ESI-MS allows the identification of metabolites from single cancer cells. *Analytical chemistry* **2018**, *90* (16), 9897-9903.
(129) Phelps, M.; Hamilton, J.; Verbeck, G. F. Nanomanipulation-coupled nanospray mass spectrometry as an approach for single cell analysis. *Review of Scientific Instruments* **2014**, *85* (12), 124101.
(130) Takats, Z.; Wiseman, J. M.; Gologan, B.; Cooks, R. G. Mass spectrometry sampling under ambient conditions with desorption electrospray ionization. *Science* **2004**, *306* (5695), 471-473.
(131) Porcari, A. M.; Zhang, J.; Garza, K. Y.; Rodrigues-Peres, R. M.; Lin, J. Q.; Young, J. H.; Tibshirani, R.; Nagi, C.; Paiva, G. R.; Carter, S. A. Multicenter study using desorption-electrospray-ionization-mass-spectrometry imaging for breast-cancer diagnosis. *Analytical chemistry* **2018**, *90* (19), 11324-11332.
(132) Garza, K. Y.; Feider, C. L.; Klein, D. R.; Rosenberg, J. A.; Brodbelt, J. S.; Eberlin, L. S. Desorption electrospray ionization mass spectrometry imaging of proteins directly from biological tissue sections. *Analytical chemistry* **2018**, *90* (13), 7785-7789.
(133) Wiseman, J. M.; Ifa, D. R.; Venter, A.; Cooks, R. G. Ambient molecular imaging by desorption electrospray ionization mass spectrometry. *Nature Protocols* **2008**, *3* (3), 517-524.
(134) Ferreira, C.; Eberlin, L.; Hallett, J.; Cooks, R. Single oocyte and single embryo lipid analysis by desorption electrospray ionization mass spectrometry. *Journal of Mass Spectrometry* **2012**, *47* (1), 29-33.
(135) Nemes, P.; Vertes, A. Laser ablation electrospray ionization for atmospheric pressure, in vivo, and imaging mass spectrometry. *Analytical chemistry* **2007**, *79* (21), 8098-8106.
(136) Shrestha, B.; Vertes, A. In situ metabolic profiling of single cells by laser ablation electrospray ionization mass spectrometry. *Analytical chemistry* **2009**, *81* (20), 8265-8271.
(137) Lee, J. K.; Jansson, E. T.; Nam, H. G.; Zare, R. N. High-resolution live-cell imaging and analysis by laser desorption/ionization droplet delivery mass spectrometry. *Analytical chemistry* **2016**, *88* (10), 5453-5461.
(138) Mueller, L.; Traub, H.; Jakubowski, N.; Drescher, D.; Baranov, V. I.; Kneipp, J. Trends in single-cell analysis by use of ICP-MS. *Analytical and bioanalytical chemistry* **2014**, *406* (27), 6963-6977.
(139) Wei, X.; Zheng, D.-H.; Cai, Y.; Jiang, R.; Chen, M.-L.; Yang, T.; Xu, Z.-R.; Yu, Y.-L.; Wang, J.-H. High-throughput/high-precision sampling of single cells into ICP-MS for elucidating cellular nanoparticles. *Analytical chemistry* **2018**, *90* (24), 14543-14550.
(140) Zhang, X.; Wei, X.; Men, X.; Jiang, Z.; Ye, W.-Q.; Chen, M.-L.; Yang, T.; Xu, Z.-R.; Wang, J.-H. Inertial-force-assisted, high-throughput, droplet-free, single-cell sampling coupled with ICP-MS for real-time cell analysis. *Analytical chemistry* **2020**, *92* (9), 6604-6612.
(141) Cahill, J. F.; Riba, J.; Kertesz, V. Rapid, untargeted chemical profiling of single cells in their native environment. *Analytical chemistry* **2019**, *91* (9), 6118-6126.
(142) Shao, Y.; Zhou, Y.; Liu, Y.; Zhang, W.; Zhu, G.; Zhao, Y.; Zhang, Q.; Yao, H.; Zhao, H.; Guo, G. Intact living-cell electrolaunching ionization mass spectrometry for single-cell metabolomics. *Chemical science*

2022, *13* (27), 8065-8073.
(143) Pan, N.; Rao, W.; Kothapalli, N. R.; Liu, R.; Burgett, A. W.; Yang, Z. The single-probe: a miniaturized multifunctional device for single cell mass spectrometry analysis. *Analytical chemistry* **2014**, *86* (19), 9376-9380.
(144) Bensen, R. C.; Standke, S. J.; Colby, D. H.; Kothapalli, N. R.; Le-McClain, A. T.; Patten, M. A.; Tripathi, A.; Heinlen, J. E.; Yang, Z.; Burgett, A. W. Single cell mass spectrometry quantification of anticancer drugs: proof of concept in cancer patients. *ACS pharmacology & translational science* **2021**, *4* (1), 96-100.
(145) Nguyen, T. D.; Lan, Y.; Kane, S. S.; Haffner, J. J.; Liu, R.; McCall, L.-I.; Yang, Z. Single-cell mass spectrometry enables insight into heterogeneity in infectious disease. *Analytical Chemistry* **2022**, *94* (30), 10567-10572.
(146) Liu, R.; Li, J.; Lan, Y.; Nguyen, T. D.; Chen, Y. A.; Yang, Z. Quantifying Cell Heterogeneity and Subpopulations Using Single Cell Metabolomics. *Analytical Chemistry* **2023**.
(147) Pan, N.; Standke, S. J.; Kothapalli, N. R.; Sun, M.; Bensen, R. C.; Burgett, A. W.; Yang, Z. Quantification of drug molecules in live single cells using the single-probe mass spectrometry technique. *Analytical chemistry* **2019**, *91* (14), 9018-9024.
(148) Standke, S. J.; Colby, D. H.; Bensen, R. C.; Burgett, A. W.; Yang, Z. Mass spectrometry measurement of single suspended cells using a combined cell manipulation system and a single-probe device. *Analytical chemistry* **2019**, *91* (3), 1738-1742.
(149) Standke, S. J.; Colby, D. H.; Bensen, R. C.; Burgett, A. W.; Yang, Z. Integrated cell manipulation platform coupled with the single-probe for mass spectrometry analysis of drugs and metabolites in single suspension cells. *JoVE (Journal of Visualized Experiments)* **2019**, (148), e59875.
(150) Cui, H.; Wu, Q.; Zhao, Z.; Wang, Y.; Lu, H. Selective Capture-Based Single-Cell Mass Spectrometry for Enhancing Sphingolipid Profiling of Neurons with Differentiation of Cell Body from Synapse. *Analytical Chemistry* **2022**.
(151) Luo, S.; Zhao, Z.; Wu, Q.; Wang, Y.; Lu, H. Porous Graphitic Carbon-Based Imprint Mass Spectrometry Imaging with an Ambient Liquid Extraction Technique for Enhancing Coverage of Glycerolipids and Sphingolipids in Brain Tissue. *Analytical Chemistry* **2022**, *94* (40), 13753-13761.
(152) Deininger, S. O.; Cornett, D. S.; Paape, R.; Becker, M.; Pineau, C.; Rauser, S.; Walch, A.; Wolski, E. Normalization in MALDI-TOF imaging datasets of proteins: practical considerations. *Anal Bioanal Chem* **2011**, *401* (1), 167-181.
(153) Yin, R.; Prabhakaran, V.; Laskin, J. Quantitative extraction and mass spectrometry analysis at a single-cell level. *Analytical chemistry* **2018**, *90* (13), 7937-7945.
(154) Cahill, J. F.; Kertesz, V. Quantitation of amiodarone and N-desethylamiodarone in single HepG2 cells by single-cell printing-liquid vortex capture-mass spectrometry. *Anal Bioanal Chem* **2021**, *413* (28), 6917-6927.
(155) Bensen, R. C.; Standke, S. J.; Colby, D. H.; Kothapalli, N. R.; Le-McClain, A. T.; Patten, M. A.; Tripathi, A.; Heinlen, J. E.; Yang, Z.; Burgett, A. W. G. Single Cell Mass Spectrometry Quantification of Anticancer Drugs: Proof of Concept in Cancer Patients. *ACS Pharmacology & Translational Science* **2021**, *4* (1), 96-100.
(156) Zhang, W.; Xu, F.; Yao, J.; Mao, C.; Zhu, M.; Qian, M.; Hu, J.; Zhong, H.; Zhou, J.; Shi, X.; et al. Single-cell metabolic fingerprints discover a cluster of circulating tumor cells with distinct metastatic potential. *Nature Communications* **2023**, *14* (1), 2485.
(157) Bruckdorfer, R. The basics about nitric oxide. *Molecular aspects of medicine* **2005**, *26* (1-2), 3-31.
(158) Garthwaite, J.; Boulton, C. Nitric oxide signaling in the central nervous system. *Annual review of*

physiology **1995**, *57* (1), 683-706.
(159) Cary, S. P.; Winger, J. A.; Derbyshire, E. R.; Marletta, M. A. Nitric oxide signaling: no longer simply on or off. *Trends in biochemical sciences* **2006**, *31* (4), 231-239.
(160) Naseem, K. M. The role of nitric oxide in cardiovascular diseases. *Molecular aspects of medicine* **2005**, *26* (1-2), 33-65.
(161) Loscalzo, J.; Welch, G. Nitric oxide and its role in the cardiovascular system. *Progress in cardiovascular diseases* **1995**, *38* (2), 87-104.
(162) Jota Baptista, C. V.; Faustino-Rocha, A. I.; Oliveira, P. A. Animal models in pharmacology: A brief history awarding the nobel prizes for physiology or medicine. *Pharmacology* **2021**, *106* (7-8), 356-368.
(163) SoRelle, R. Nobel prize awarded to scientists for nitric oxide discoveries. *Circulation* **1998**, *98* (22), 2365-2366.
(164) Hermann, M.; Flammer, A.; Lüscher, T. F. Nitric oxide in hypertension. *The Journal of Clinical Hypertension* **2006**, *8*, 17-29.
(165) Carnicer, R.; Crabtree, M. J.; Sivakumaran, V.; Casadei, B.; Kass, D. A. Nitric oxide synthases in heart failure. *Antioxidants & redox signaling* **2013**, *18* (9), 1078-1099.
(166) Divakaran, S.; Loscalzo, J. The role of nitroglycerin and other nitrogen oxides in cardiovascular therapeutics. *Journal of the american college of cardiology* **2017**, *70* (19), 2393-2410.
(167) Curry, S. C.; Spyres, M. B. Sodium Nitroprusside. In *Critical Care Toxicology: Diagnosis and Management of the Critically Poisoned Patient*, Brent, J., Burkhart, K., Dargan, P., Hatten, B., Megarbane, B., Palmer, R., White, J. Eds.; Springer International Publishing, 2017; pp 843-850.
(168) Holme, M. R.; Sharman, T. Sodium nitroprusside. **2020**.
(169) Sayed-Ahmed, M. M.; Khattab, M. M.; Gad, M. Z.; Osman, A. M. M. Increased plasma endothelin-1 and cardiac nitric oxide during doxorubicin-induced cardiomyopathy. *Pharmacology & toxicology* **2001**, *89* (3), 140-144.
(170) Salaroglio, I. C.; Gazzano, E.; Abdullrahman, A.; Mungo, E.; Castella, B.; Abd-elrahman, G. E. F. A.-e.; Massaia, M.; Donadelli, M.; Rubinstein, M.; Riganti, C. Increasing intratumor C/EBP-β LIP and nitric oxide levels overcome resistance to doxorubicin in triple negative breast cancer. *Journal of Experimental & Clinical Cancer Research* **2018**, *37*, 1-20.
(171) Aldieri, E.; Bergandi, L.; Riganti, C.; Costamagna, C.; Bosia, A.; Ghigo, D. Doxorubicin induces an increase of nitric oxide synthesis in rat cardiac cells that is inhibited by iron supplementation. *Toxicology and applied pharmacology* **2002**, *185* (2), 85-90.
(172) Taylor-Robinson, A. W.; Liew, F. Y.; Severn, A.; Xu, D.; McSorley, S. J.; Garside, P.; Padron, J.; Phillips, R. S. Regulation of the immune response by nitric oxide differentially produced by T helper type 1 and T helper type 2 cells. *European journal of immunology* **1994**, *24* (4), 980-984.
(173) Bogdan, C. Nitric oxide and the immune response. *Nature immunology* **2001**, *2* (10), 907-916.
(174) Bogdan, C. The function of nitric oxide in the immune system. In *Nitric oxide*, Springer, 2000; pp 443-492.
(175) Tripathi, P.; Tripathi, P.; Kashyap, L.; Singh, V. The role of nitric oxide in inflammatory reactions. *FEMS Immunology & Medical Microbiology* **2007**, *51* (3), 443-452.
(176) Ye, X.; Rubakhin, S. S.; Sweedler, J. V. Detection of nitric oxide in single cells. *Analyst* **2008**, *133* (4), 423-433.
(177) Hu, Y.; Xiang, J.; Su, L.; Tang, X. The regulation of nitric oxide in tumor progression and therapy. *Journal of International Medical Research* **2020**, *48* (2), 0300060520905985.
(178) Zhong, Z.-J.; Yao, Z.-P.; Shi, Z.-Q.; Liu, Y.-D.; Liu, L.-F.; Xin, G.-Z. Measurement of Intracellular Nitric

Oxide with a Quantitative Mass Spectrometry Probe Approach. *Analytical Chemistry* **2021**, *93* (24), 8536-8543.
(179) Singh, S.; Gupta, A. K. Nitric oxide: role in tumour biology and iNOS/NO-based anticancer therapies. *Cancer chemotherapy and pharmacology* **2011**, *67*, 1211-1224.
(180) Mocellin, S. Nitric oxide: cancer target or anticancer agent? *Current cancer drug targets* **2009**, *9* (2), 214-236.
(181) Raj, A.; Rifkin, S. A.; Andersen, E.; van Oudenaarden, A. Variability in gene expression underlies incomplete penetrance. *Nature* **2010**, *463* (7283), 913-918.
(182) Qian, C. Y.; Yun, Z. H.; Yao, Y. D.; Cao, M. H.; Liu, Q.; Hu, S.; Zhang, S. H.; Luo, D. Y. Heterogeneous macrophages: Supersensors of exogenous inducing factors. *Scand J Immunol* **2019**, *90* (1).
(183) Meacham, C. E.; Morrison, S. J. Tumour heterogeneity and cancer cell plasticity. *Nature* **2013**, *501* (7467), 328-337.
(184) Tang, D. G. Understanding cancer stem cell heterogeneity and plasticity. *Cell research* **2012**, *22* (3), 457-472.
(185) Gay, L.; Baker, A.-M.; Graham, T. A. Tumour cell heterogeneity. *F1000Research* **2016**, *5*.
(186) Xie, H.; Li, Y.-T.; Lei, Y.-M.; Liu, Y.-L.; Xiao, M.-M.; Gao, C.; Pang, D.-W.; Huang, W.-H.; Zhang, Z.-Y.; Zhang, G.-J. Real-time monitoring of nitric oxide at single-cell level with porphyrin-functionalized graphene field-effect transistor biosensor. *Analytical chemistry* **2016**, *88* (22), 11115-11122.
(187) Archer, S. Measurement of nitric oxide in biological models. *The FASEB journal* **1993**, *7* (2), 349-360.
(188) Yao, D.; Vlessidis, A. G.; Evmiridis, N. P. Determination of nitric oxide in biological samples. *Microchimica Acta* **2004**, *147*, 1-20.
(189) Hetrick, E. M.; Schoenfisch, M. H. Analytical chemistry of nitric oxide. *Annual review of analytical chemistry* **2009**, *2*, 409-433.
(190) Taha, Z. H. Nitric oxide measurements in biological samples. *Talanta* **2003**, *61* (1), 3-10.
(191) Murphy, M. E.; Noack, E. [24] Nitric oxide assay using hemoglobin method. In *Methods in enzymology*, Vol. 233; Elsevier, 1994; pp 240-250.
(192) Sun, J.; Zhang, X.; Broderick, M.; Fein, H. Measurement of nitric oxide production in biological systems by using Griess reaction assay. *Sensors* **2003**, *3* (8), 276-284.
(193) Bryan, N. S.; Grisham, M. B. Methods to detect nitric oxide and its metabolites in biological samples. *Free radical biology and medicine* **2007**, *43* (5), 645-657.
(194) Hong, H.; Sun, J.; Cai, W. Multimodality imaging of nitric oxide and nitric oxide synthases. *Free Radical Biology and Medicine* **2009**, *47* (6), 684-698.
(195) Woldman, Y. Y.; Eubank, T. D.; Mock, A. J.; Stevens, N. C.; Varadharaj, S.; Turco, J.; Gavrilin, M. A.; Branchini, B. R.; Khramtsov, V. V. Detection of nitric oxide production in cell cultures by luciferin–luciferase chemiluminescence. *Biochemical and biophysical research communications* **2015**, *465* (2), 232-238.
(196) MacArthur, P. H.; Shiva, S.; Gladwin, M. T. Measurement of circulating nitrite and S-nitrosothiols by reductive chemiluminescence. *Journal of Chromatography B* **2007**, *851* (1-2), 93-105.
(197) Ciszewski, A.; Milczarek, G. Electrochemical detection of nitric oxide using polymer modified electrodes. *Talanta* **2003**, *61* (1), 11-26.
(198) Jo, A.; Do, H.; Jhon, G.-J.; Suh, M.; Lee, Y. Electrochemical nanosensor for real-time direct imaging of nitric oxide in living brain. *Analytical chemistry* **2011**, *83* (21), 8314-8319.
(199) Tang, L.; Li, Y.; Xie, H.; Shu, Q.; Yang, F.; Liu, Y.-l.; Liang, F.; Wang, H.; Huang, W.; Zhang, G.-J. A sensitive acupuncture needle microsensor for real-time monitoring of nitric oxide in acupoints of rats. *Scientific reports* **2017**, *7* (1), 6446.

(200) Trettin, A.; Böhmer, A.; Suchy, M.-T.; Probst, I.; Staerk, U.; Stichtenoth, D. O.; Frölich, J. C.; Tsikas, D. Effects of paracetamol on NOS, COX, and CYP activity and on oxidative stress in healthy male subjects, rat hepatocytes, and recombinant NOS. *Oxidative Medicine and Cellular Longevity* **2014**, *2014*.
(201) Becker, A.; Ückert, S.; Tsikas, D.; Noack, H.; Stief, C.; Frölich, J.; Wolf, G.; Jonas, U. Determination of nitric oxide metabolites by means of the Griess assay and gas chromatography–mass spectrometry in the cavernous and systemic blood of healthy males and patients with erectile dysfunction during different functional conditions of the penis. *Urological research* **2000**, *28*, 364-369.
(202) Kiechle, F. L.; Malinski, T. Nitric oxide: biochemistry, pathophysiology, and detection. *American Journal of Clinical Pathology* **1993**, *100* (5), 567-575.
(203) Hirayama, A.; Nagase, S.; Ueda, A.; Yoh, K.; Oteki, T.; Obara, M.; Takada, K.; Shimozawa, Y.; Aoyagi, K.; Koyama, A. Electron paramagnetic resonance imaging of nitric oxide organ distribution in lipopolysuccaride treated mice. *Guanidino Compounds in Biology and Medicine* **2003**, 63-67.
(204) Ren, J.; Fung, P.; Chang, C.; Shen, G.; Lu, G.; Chan, F.; Liu, K.; Shen, J. A comparative ESR study on blood and tissue nitric oxide concentration during renal ischemia-reperfusion injury. *Applied Magnetic Resonance* **2007**, *32*, 243-255.
(205) Lindermayr, C.; Durner, J. Nitric oxide sensor proteins with revolutionary potential. *Journal of Experimental Botany* **2018**, *69* (15), 3507-3510.
(206) Fujii, H.; Wan, X.; Zhong, J.; Berliner, L. J.; Yoshikawa, K. In vivo imaging of spin-trapped nitric oxide in rats with septic shock: MRI spin trapping. *Magnetic Resonance in Medicine: An Official Journal of the International Society for Magnetic Resonance in Medicine* **1999**, *42* (2), 235-239.
(207) Liu, G.; Pagel, M. A smart PARACEST MRI contrast agent for nitric oxide detection. In *Proceedings of the 14th Annual Meeting of ISMRM*, 2006.
(208) Yang, Q.; Zhang, X.; Bao, X.; Lu, H.; Zhang, W.; Wu, W.; Miao, H.; Jiao, B. Single cell determination of nitric oxide release using capillary electrophoresis with laser-induced fluorescence detection. *Journal of Chromatography A* **2008**, *1201* (1), 120-127.
(209) Sarti, P.; Lendaro, E.; IPPOLITI, R.; Bellelli, A.; BENEDETTI, P. A.; BRUNORI, M. Modulation of mitochondrial respiration by nitric oxide: investigation by single cell fluorescence microscopy. *The FASEB Journal* **1999**, *13* (1), 191-197.
(210) Goshi, E.; Zhou, G.; He, Q. Nitric oxide detection methods in vitro and in vivo. *Medical gas research* **2019**, *9* (4), 192.
(211) Kind, T.; Tsugawa, H.; Cajka, T.; Ma, Y.; Lai, Z.; Mehta, S. S.; Wohlgemuth, G.; Barupal, D. K.; Showalter, M. R.; Arita, M. Identification of small molecules using accurate mass MS/MS search. *Mass spectrometry reviews* **2018**, *37* (4), 513-532.
(212) Kim, B.; Araujo, R.; Howard, M.; Magni, R.; Liotta, L. A.; Luchini, A. Affinity enrichment for mass spectrometry: improving the yield of low abundance biomarkers. *Expert review of proteomics* **2018**, *15* (4), 353-366.
(213) Guzman, N. A.; Blanc, T.; Phillips, T. M. Immunoaffinity capillary electrophoresis as a powerful strategy for the quantification of low-abundance biomarkers, drugs, and metabolites in biological matrices. *Electrophoresis* **2008**, *29* (16), 3259-3278.
(214) Tajik, M.; Baharfar, M.; Donald, W. A. Single-cell mass spectrometry. *Trends in Biotechnology* **2022**, *40* (11), 1374-1392.
(215) Schober, Y.; Guenther, S.; Spengler, B.; Ro ¨ mpp, A. Single cell matrix-assisted laser desorption/ionization mass spectrometry imaging. *Analytical chemistry* **2012**, *84* (15), 6293-6297.
(216) Wu, K.; Jia, F.; Zheng, W.; Luo, Q.; Zhao, Y.; Wang, F. Visualization of metallodrugs in single cells by

secondary ion mass spectrometry imaging. *JBIC Journal of Biological Inorganic Chemistry* **2017**, *22*, 653-661.
(217) Zhu, X.; Xu, T.; Peng, C.; Wu, S. Advances in MALDI mass spectrometry imaging single cell and tissues. *Frontiers in Chemistry* **2022**, *9*, 782432.
(218) Ifa, D. R.; Wu, C.; Ouyang, Z.; Cooks, R. G. Desorption electrospray ionization and other ambient ionization methods: current progress and preview. *Analyst* **2010**, *135* (4), 669-681.
(219) Soudah, T.; Zoabi, A.; Margulis, K. Desorption electrospray ionization mass spectrometry imaging in discovery and development of novel therapies. *Mass Spectrometry Reviews* **2023**, *42* (2), 751-778.
(220) Roach, P. J.; Laskin, J.; Laskin, A. Nanospray desorption electrospray ionization: an ambient method for liquid-extraction surface sampling in mass spectrometry. *Analyst* **2010**, *135* (9), 2233-2236.
(221) Hale, O. J.; Cooper, H. J. Native mass spectrometry imaging of proteins and protein complexes by nano-DESI. *Analytical chemistry* **2021**, *93* (10), 4619-4627.
(222) Li, X.; Hu, H.; Yin, R.; Li, Y.; Sun, X.; Dey, S. K.; Laskin, J. High-Throughput Nano-DESI Mass Spectrometry Imaging of Biological Tissues Using an Integrated Microfluidic Probe. *Analytical Chemistry* **2022**, *94* (27), 9690-9696.
(223) Tsuyama, N.; Mizuno, H.; Tokunaga, E.; Masujima, T. Live single-cell molecular analysis by video-mass spectrometry. *Analytical Sciences* **2008**, *24* (5), 559-561.
(224) Shimizu, T.; Miyakawa, S.; Esaki, T.; Mizuno, H.; Masujima, T.; Koshiba, T.; Seo, M. Live single-cell plant hormone analysis by video-mass spectrometry. *Plant and Cell Physiology* **2015**, *56* (7), 1287-1296.
(225) Pan, N.; Rao, W.; Standke, S. J.; Yang, Z. Using dicationic ion-pairing compounds to enhance the single cell mass spectrometry analysis using the single-probe: a microscale sampling and ionization device. *Analytical chemistry* **2016**, *88* (13), 6812-6819.
(226) Meng, Y.; Song, X.; Zare, R. N. Laser ablation electrospray ionization achieves 5 μm resolution using a microlensed fiber. *Analytical Chemistry* **2022**, *94* (28), 10278-10282.
(227) Wei, Z.; Xiong, X.; Guo, C.; Si, X.; Zhao, Y.; He, M.; Yang, C.; Xu, W.; Tang, F.; Fang, X. Pulsed direct current electrospray: enabling systematic analysis of small volume sample by boosting sample economy. *Analytical chemistry* **2015**, *87* (22), 11242-11248.
(228) Zhu, G.; Shao, Y.; Liu, Y.; Pei, T.; Li, L.; Zhang, D.; Guo, G.; Wang, X. Single-cell metabolite analysis by electrospray ionization mass spectrometry. *TrAC Trends in Analytical Chemistry* **2021**, *143*, 116351.
(229) Gillette, M. A.; Carr, S. A. Quantitative analysis of peptides and proteins in biomedicine by targeted mass spectrometry. *Nature methods* **2013**, *10* (1), 28-34.
(230) Urban, P. L. Quantitative mass spectrometry: an overview. *Philosophical Transactions of the Royal Society A: Mathematical, Physical and Engineering Sciences* **2016**, *374* (2079), 20150382.
(231) Rubakhin, S. S.; Sweedler, J. V. Quantitative measurements of cell− cell signaling peptides with single-cell MALDI MS. *Analytical chemistry* **2008**, *80* (18), 7128-7136.
(232) Liu, R.; Sun, M.; Zhang, G.; Lan, Y.; Yang, Z. Towards early monitoring of chemotherapy-induced drug resistance based on single cell metabolomics: Combining single-probe mass spectrometry with machine learning. *Anal Chim Acta* **2019**, *1092*, 42-48.
(233) Liu, R.; Li, J.; Lan, Y.; Nguyen, T. D.; Chen, Y. A.; Yang, Z. Quantifying Cell Heterogeneity and Subpopulations Using Single Cell Metabolomics. *Analytical Chemistry* **2023**, *95* (18), 7127-7133.
(234) Itoh, T.; Nagata, K.; Matsuya, Y.; Miyazaki, M.; Ohsawa, A. Reaction of nitric oxide with amines. *The Journal of Organic Chemistry* **1997**, *62* (11), 3582-3585.
(235) Ma, S.; Fang, D.-C.; Ning, B.; Li, M.; He, L.; Gong, B. The rational design of a highly sensitive and

selective fluorogenic probe for detecting nitric oxide. *Chemical Communications* **2014**, *50* (49), 6475-6478.
(236) Gao, C.; Lin, L.; Sun, W.; Tan, Z.-L.; Huang, J.-R.; He, L.; Lu, Z.-L. Dihydropyridine-derived BODIPY probe for detecting exogenous and endogenous nitric oxide in mitochondria. *Talanta* **2018**, *176*, 382-388.
(237) Li, H.; Zhang, D.; Gao, M.; Huang, L.; Tang, L.; Li, Z.; Chen, X.; Zhang, X. Highly specific C–C bond cleavage induced FRET fluorescence for in vivo biological nitric oxide imaging. *Chemical Science* **2017**, *8* (3), 2199-2203.
(238) Zhu, Y.; Wang, F.; Li, Q.; Zhu, M.; Du, A.; Tang, W.; Chen, W. Amlodipine metabolism in human liver microsomes and roles of CYP3A4/5 in the dihydropyridine dehydrogenation. *Drug Metabolism and Disposition* **2014**, *42* (2), 245-249.
(239) Panuwet, P.; Hunter Jr, R. E.; D'Souza, P. E.; Chen, X.; Radford, S. A.; Cohen, J. R.; Marder, M. E.; Kartavenka, K.; Ryan, P. B.; Barr, D. B. Biological matrix effects in quantitative tandem mass spectrometry-based analytical methods: advancing biomonitoring. *Critical reviews in analytical chemistry* **2016**, *46* (2), 93-105.
(240) Xiao, J. F.; Zhou, B.; Ressom, H. W. Metabolite identification and quantitation in LC-MS/MS-based metabolomics. *TrAC Trends in Analytical Chemistry* **2012**, *32*, 1-14.
(241) Balligand, J.-L.; Cannon, P. J. Nitric oxide synthases and cardiac muscle: autocrine and paracrine influences. *Arteriosclerosis, thrombosis, and vascular biology* **1997**, *17* (10), 1846-1858.
(242) Shah, A. M.; MacCarthy, P. A. Paracrine and autocrine effects of nitric oxide on myocardial function. *Pharmacology & therapeutics* **2000**, *86* (1), 49-86.
(243) Yao, H.-W.; Guo, X.-F.; Wang, H. Simultaneous quantitation of intra-and extracellular nitric oxide in single macrophage RAW 264.7 cells by capillary electrophoresis with laser-induced fluorescence detection. *Analytical Chemistry* **2020**, *92* (17), 11904-11911.
(244) Zhang, Z.-X.; Guo, X.-F.; Wang, H.; Zhang, H.-S. Capillary electrophoresis strategy to monitor the released and remaining nitric oxide from the same single cell using a specially designed water-soluble fluorescent probe. *Analytical chemistry* **2015**, *87* (7), 3989-3995.
(245) Li, L.; Li, Q.; Chen, P.; Li, Z.; Chen, Z.; Tang, B. Consecutive gated injection-based microchip electrophoresis for simultaneous quantitation of superoxide anion and nitric oxide in single PC-12 cells. *Analytical chemistry* **2016**, *88* (1), 930-936.
(246) Stopka, S. A.; Khattar, R.; Agtuca, B. J.; Anderton, C. R.; Paša-Tolić, L.; Stacey, G.; Vertes, A. Metabolic noise and distinct subpopulations observed by single cell LAESI mass spectrometry of plant cells in situ. *Frontiers in plant science* **2018**, *9*, 1646.
(247) Ashman, K. M.; Bird, C. M.; Zepf, S. E. Detecting bimodality in astronomical datasets. *arXiv preprint astro-ph/9408030* **1994**.
(248) Khaleel, S. A.; Al-Abd, A. M.; Ali, A. A.; Abdel-Naim, A. B. Didox and resveratrol sensitize colorectal cancer cells to doxorubicin via activating apoptosis and ameliorating P-glycoprotein activity. *Scientific reports* **2016**, *6* (1), 36855.
(249) Mainz, E. R.; Gunasekara, D. B.; Caruso, G.; Jensen, D. T.; Hulvey, M. K.; Da Silva, J. A. F.; Metto, E. C.; Culbertson, A. H.; Culbertson, C. T.; Lunte, S. M. Monitoring intracellular nitric oxide production using microchip electrophoresis and laser-induced fluorescence detection. *Analytical Methods* **2012**, *4* (2), 414-420.
(250) Standke, S. J.; Colby, D. H.; Bensen, R. C.; Burgett, A. W. G.; Yang, Z. Mass Spectrometry Measurement of Single Suspended Cells Using a Combined Cell Manipulation System and a Single-Probe Device. *Analytical Chemistry* **2019**, *91* (3), 1738-1742.
(251) Xin, X.; Wang, H.; Han, L.; Wang, M.; Fang, H.; Hao, Y.; Li, J.; Zhang, H.; Zheng, C.; Shen, C. Single-Cell

Analysis of the Impact of Host Cell Heterogeneity on Infection with Foot-and-Mouth Disease Virus. *J Virol* **2018**, *92* (9).
(252) Kamies, R.; Martinez-Jimenez, C. P. Advances of single-cell genomics and epigenomics in human disease: where are we now? *Mammalian Genome* **2020**, *31* (5), 170-180.
(253) Fernandes, M. C.; Andrews, N. W. Host cell invasion by Trypanosoma cruzi: a unique strategy that promotes persistence. *FEMS Microbiol Rev* **2012**, *36* (3), 734-747.
(254) D'Avila, H.; Freire-de-Lima, C. G.; Roque, N. R.; Teixeira, L.; Barja-Fidalgo, C.; Silva, A. R.; Melo, R. C.; Dosreis, G. A.; Castro-Faria-Neto, H. C.; Bozza, P. T. Host cell lipid bodies triggered by Trypanosoma cruzi infection and enhanced by the uptake of apoptotic cells are associated with prostaglandin E_2 generation and increased parasite growth. *J Infect Dis* **2011**, *204* (6), 951-961.
(255) Nagajyothi, F.; Desruisseaux, M. S.; Weiss, L. M.; Chua, S.; Albanese, C.; Machado, F. S.; Esper, L.; Lisanti, M. P.; Teixeira, M. M.; Scherer, P. E.; et al. Chagas disease, adipose tissue and the metabolic syndrome. *Memórias do Instituto Oswaldo Cruz* **2009**, *104*, 219-225.
(256) Hoffman, K.; Liu, Z.; Hossain, E.; Bottazzi, M. E.; Hotez, P. J.; Jones, K. M.; McCall, L. I. Alterations to the Cardiac Metabolome Induced by Chronic T. cruzi Infection Relate to the Degree of Cardiac Pathology. *ACS Infect Dis* **2021**, *7* (6), 1638-1649.
(257) McCall, L. I.; Morton, J. T.; Bernatchez, J. A.; de Siqueira-Neto, J. L.; Knight, R.; Dorrestein, P. C.; McKerrow, J. H. Mass Spectrometry-Based Chemical Cartography of a Cardiac Parasitic Infection. *Anal Chem* **2017**, *89* (19), 10414-10421.
(258) Dean, D. A.; Gautham, G.; Siqueira-Neto, J. L.; McKerrow, J. H.; Dorrestein, P. C.; McCall, L.-I. Spatial metabolomics identifies localized chemical changes in heart tissue during chronic cardiac Chagas Disease. *PLOS Neglected Tropical Diseases* **2021**, *15* (10), e0009819.
(259) Hossain, E.; Khanam, S.; Dean, D. A.; Wu, C.; Lostracco-Johnson, S.; Thomas, D.; Kane, S. S.; Parab, A. R.; Flores, K.; Katemauswa, M.; et al. Mapping of host-parasite-microbiome interactions reveals metabolic determinants of tropism and tolerance in Chagas disease. *Sci Adv* **2020**, *6* (30), eaaz2015.
(260) Liu, Z.; Ulrich vonBargen, R.; McCall, L. I. Central role of metabolism in Trypanosoma cruzi tropism and Chagas disease pathogenesis. *Curr Opin Microbiol* **2021**, *63*, 204-209.
(261) Kolodziejczyk, Aleksandra A.; Kim, J. K.; Svensson, V.; Marioni, John C.; Teichmann, Sarah A. The Technology and Biology of Single-Cell RNA Sequencing. *Molecular Cell* **2015**, *58* (4), 610-620.
(262) Bengtsson, M.; Hemberg, M.; Rorsman, P.; Ståhlberg, A. Quantification of mRNA in single cells and modelling of RT-qPCR induced noise. *BMC Molecular Biology* **2008**, *9* (1), 63.
(263) Drayman, N.; Patel, P.; Vistain, L.; Tay, S. HSV-1 single-cell analysis reveals the activation of anti-viral and developmental programs in distinct sub-populations. *eLife* **2019**, *8*, e46339.
(264) Albayrak, C.; Jordi, C. A.; Zechner, C.; Lin, J.; Bichsel, C. A.; Khammash, M.; Tay, S. Digital Quantification of Proteins and mRNA in Single Mammalian Cells. *Mol Cell* **2016**, *61* (6), 914-924.
(265) Zhang, Y.; Naguro, I.; Herr, A. E. In Situ Single-Cell Western Blot on Adherent Cell Culture. *Angewandte Chemie International Edition* **2019**, *58* (39), 13929-13934.
(266) Minakshi, P.; Ghosh, M.; Kumar, R.; Patki, H. S.; Saini, H. M.; Ranjan, K.; Brar, B.; Prasad, G. Chapter 15 - Single-Cell Metabolomics: Technology and Applications. In *Single-Cell Omics*, Barh, D., Azevedo, V. Eds.; Academic Press, 2019; pp 319-353.
(267) Kumar, R.; Ghosh, M.; Kumar, S.; Prasad, M. Single Cell Metabolomics: A Future Tool to Unmask Cellular Heterogeneity and Virus-Host Interaction in Context of Emerging Viral Diseases. *Frontiers in Microbiology* **2020**, *11*.
(268) Dolatmoradi, M.; Samarah, L. Z.; Vertes, A. Single-Cell Metabolomics by Mass Spectrometry:

Opportunities and Challenges. *Analysis & Sensing* **2022**, *2* (1), e202100032.
(269) Boggio, K. J.; Obasuyi, E.; Sugino, K.; Nelson, S. B.; Agar, N. Y. R.; Agar, J. N. Recent advances in single-cell MALDI mass spectrometry imaging and potential clinical impact. *Expert Rev Proteomic* **2011**, *8* (5), 591-604.
(270) Jungnickel, H.; Laux, P.; Luch, A. Time-of-Flight Secondary Ion Mass Spectrometry (ToF-SIMS): A New Tool for the Analysis of Toxicological Effects on Single Cell Level. *Toxics* **2016**, *4* (1).
(271) Gong, X. Y.; Zhao, Y. Y.; Cai, S. Q.; Fu, S. J.; Yang, C. D.; Zhang, S. C.; Zhang, X. R. Single Cell Analysis with Probe ESI-Mass Spectrometry: Detection of Metabolites at Cellular and Subcellular Levels. *Analytical Chemistry* **2014**, *86* (8), 3809-3816.
(272) Bergman, H. M.; Lanekoff, I. Profiling and quantifying endogenous molecules in single cells using nano-DESI MS. *Analyst* **2017**, *142* (19), 3639-3647.
(273) Pan, N.; Rao, W.; Kothapalli, N. R.; Liu, R.; Burgett, A. W. G.; Yang, Z. The Single-Probe: A Miniaturized Multifunctional Device for Single Cell Mass Spectrometry Analysis. *Analytical Chemistry* **2014**, *86* (19), 9376-9380.
(274) Liu, R.; Pan, N.; Zhu, Y.; Yang, Z. T-Probe: An Integrated Microscale Device for Online In Situ Single Cell Analysis and Metabolic Profiling Using Mass Spectrometry. *Anal Chem* **2018**, *90* (18), 11078-11085.
(275) Pan, N.; Standke, S. J.; Kothapalli, N. R.; Sun, M.; Bensen, R. C.; Burgett, A. W. G.; Yang, Z. Quantification of Drug Molecules in Live Single Cells Using the Single-Probe Mass Spectrometry Technique. *Analytical Chemistry* **2019**, *91* (14), 9018-9024.
(276) Sun, M.; Tian, X.; Yang, Z. Microscale Mass Spectrometry Analysis of Extracellular Metabolites in Live Multicellular Tumor Spheroids. *Anal Chem* **2017**, *89* (17), 9069-9076.
(277) Standke, S. J.; Colby, D. H.; Bensen, R. C.; Burgett, A. W. G.; Yang, Z. Integrated Cell Manipulation Platform Coupled with the Single-probe for Mass Spectrometry Analysis of Drugs and Metabolites in Single Suspension Cells. *J Vis Exp* **2019**, (148), 10.3791/59875.
(278) Tian, X.; Zhang, G.; Zou, Z.; Yang, Z. Anticancer Drug Affects Metabolomic Profiles in Multicellular Spheroids: Studies Using Mass Spectrometry Imaging Combined with Machine Learning. *Anal Chem* **2019**, *91* (9), 5802-5809.
(279) Liu, R.; Zhang, G.; Yang, Z. Towards rapid prediction of drug-resistant cancer cell phenotypes: single cell mass spectrometry combined with machine learning. *Chem Commun (Camb)* **2019**, *55* (5), 616-619.
(280) Roberts, B. L.; Severance, Z. C.; Bensen, R. C.; Le, A. T.; Kothapalli, N. R.; Nuñez, J. I.; Ma, H.; Wu, S.; Standke, S. J.; Yang, Z.; et al. Transient Compound Treatment Induces a Multigenerational Reduction of Oxysterol-Binding Protein (OSBP) Levels and Prophylactic Antiviral Activity. *ACS Chemical Biology* **2019**, *14* (2), 276-287.
(281) Liu, M.; Zhang, Y.; Yang, J.; Cui, X.; Zhou, Z.; Zhan, H.; Ding, K.; Tian, X.; Yang, Z.; Fung, K. A.; et al. ZIP4 Increases Expression of Transcription Factor ZEB1 to Promote Integrin α3β1 Signaling and Inhibit Expression of the Gemcitabine Transporter ENT1 in Pancreatic Cancer Cells. *Gastroenterology* **2020**, *158* (3), 679-692.e671.
(282) Sun, M.; Yang, Z. Metabolomic Studies of Live Single Cancer Stem Cells Using Mass Spectrometry. *Anal Chem* **2019**, *91* (3), 2384-2391.
(283) Sun, M.; Yang, Z.; Wawrik, B. Metabolomic Fingerprints of Individual Algal Cells Using the Single-Probe Mass Spectrometry Technique. *Frontiers in Plant Science* **2018**, *9*.
(284) Rao, W.; Pan, N.; Yang, Z. High Resolution Tissue Imaging Using the Single-probe Mass Spectrometry under Ambient Conditions. *J Am Soc Mass Spectrom* **2015**, *26* (6), 986-993.
(285) Rao, W.; Pan, N.; Tian, X.; Yang, Z. High-Resolution Ambient MS Imaging of Negative Ions in Positive

Ion Mode: Using Dicationic Reagents with the Single-Probe. *Journal of the American Society for Mass Spectrometry* **2016**, *27* (1), 124-134.
(286) Rao, W.; Pan, N.; Yang, Z. Applications of the Single-probe: Mass Spectrometry Imaging and Single Cell Analysis under Ambient Conditions. *J Vis Exp* **2016**, (112).
(287) Tian, X.; Xie, B.; Zou, Z.; Jiao, Y.; Lin, L.-E.; Chen, C.-L.; Hsu, C.-C.; Peng, J.; Yang, Z. Multimodal Imaging of Amyloid Plaques: Fusion of the Single-Probe Mass Spectrometry Image and Fluorescence Microscopy Image. *Analytical Chemistry* **2019**, *91* (20), 12882-12889.
(288) Sun, M.; Tian, X.; Yang, Z. Microscale Mass Spectrometry Analysis of Extracellular Metabolites in Live Multicellular Tumor Spheroids. *Analytical Chemistry* **2017**, *89* (17), 9069-9076.
(289) Buckner, F. S.; Verlinde, C. L.; La Flamme, A. C.; Van Voorhis, W. C. Efficient technique for screening drugs for activity against Trypanosoma cruzi using parasites expressing beta-galactosidase. *Antimicrob Agents Chemother* **1996**, *40* (11), 2592-2597.
(290) Monvoisin, A.; Alva, J. A.; Hofmann, J. J.; Zovein, A. C.; Lane, T. F.; Iruela-Arispe, M. L. VE-cadherin-CreERT2 transgenic mouse: A model for inducible recombination in the endothelium. *Developmental Dynamics* **2006**, *235* (12), 3413-3422.
(291) Liu, R.; Zhang, G.; Sun, M.; Pan, X.; Yang, Z. Integrating a generalized data analysis workflow with the Single-probe mass spectrometry experiment for single cell metabolomics. *Analytica chimica acta* **2019**, *1064*, 71-79.
(292) Romano, P.; Profumo, A.; Rocco, M.; Mangerini, R.; Ferri, F.; Facchiano, A. Geena 2, improved automated analysis of MALDI/TOF mass spectra. *BMC Bioinformatics* **2016**, *17* (4), 61.
(293) Xia, J.; Broadhurst, D. I.; Wilson, M.; Wishart, D. S. Translational biomarker discovery in clinical metabolomics: an introductory tutorial. *Metabolomics* **2013**, *9* (2), 280-299.
(294) Xia, J.; Sinelnikov, I. V.; Wishart, D. S. MetATT: a web-based metabolomics tool for analyzing time-series and two-factor datasets. *Bioinformatics* **2011**, *27* (17), 2455-2456.
(295) Xia, J.; Wishart, D. S. MetPA: a web-based metabolomics tool for pathway analysis and visualization. *Bioinformatics* **2010**, *26* (18), 2342-2344.
(296) Xia, J.; Wishart, D. S. Web-based inference of biological patterns, functions and pathways from metabolomic data using MetaboAnalyst. *Nature Protocols* **2011**, *6* (6), 743-760.
(297) Pang, Z.; Chong, J.; Zhou, G.; de Lima Morais, D. A.; Chang, L.; Barrette, M.; Gauthier, C.; Jacques, P.-É.; Li, S.; Xia, J. MetaboAnalyst 5.0: narrowing the gap between raw spectra and functional insights. *Nucleic Acids Research* **2021**, *49* (W1), W388-W396.
(298) Quirk, T. J. One-Way Analysis of Variance (ANOVA). In *Excel 2007 for Educational and Psychological Statistics: A Guide to Solving Practical Problems*, Springer New York, 2012; pp 163-179.
(299) Liu, R.; Yang, Z. Single cell metabolomics using mass spectrometry: Techniques and data analysis. *Anal Chim Acta* **2021**, *1143*, 124-134.
(300) Smith, C. A.; Maille, G. O.; Want, E. J.; Qin, C.; Trauger, S. A.; Brandon, T. R.; Custodio, D. E.; Abagyan, R.; Siuzdak, G. METLIN: A Metabolite Mass Spectral Database. *Therapeutic Drug Monitoring* **2005**, *27* (6), 747-751.
(301) Wishart, D. S.; Feunang, Y. D.; Marcu, A.; Guo, A. C.; Liang, K.; Vázquez-Fresno, R.; Sajed, T.; Johnson, D.; Li, C.; Karu, N.; et al. HMDB 4.0: the human metabolome database for 2018. *Nucleic Acids Research* **2017**, *46* (D1), D608-D617.
(302) Wang, M.; Carver, J. J.; Phelan, V. V.; Sanchez, L. M.; Garg, N.; Peng, Y.; Nguyen, D. D.; Watrous, J.; Kapono, C. A.; Luzzatto-Knaan, T.; et al. Sharing and community curation of mass spectrometry data with Global Natural Products Social Molecular Networking. *Nature Biotechnology* **2016**, *34* (8), 828-837.

(303) Wang, M.; Jarmusch, A. K.; Vargas, F.; Aksenov, A. A.; Gauglitz, J. M.; Weldon, K.; Petras, D.; da Silva, R.; Quinn, R.; Melnik, A. V.; et al. Mass spectrometry searches using MASST. *Nature Biotechnology* **2020**, *38* (1), 23-26.
(304) Chambers, M. C.; Maclean, B.; Burke, R.; Amodei, D.; Ruderman, D. L.; Neumann, S.; Gatto, L.; Fischer, B.; Pratt, B.; Egertson, J.; et al. A cross-platform toolkit for mass spectrometry and proteomics. *Nature Biotechnology* **2012**, *30* (10), 918-920.
(305) Dumoulin, P. C.; Burleigh, B. A. Metabolic flexibility in Trypanosoma cruzi amastigotes: implications for persistence and drug sensitivity. *Curr Opin Microbiol* **2021**, *63*, 244-249.
(306) Khan, A. A.; Langston, H. C.; Costa, F. C.; Olmo, F.; Taylor, M. C.; McCann, C. J.; Kelly, J. M.; Lewis, M. D. Local association of Trypanosoma cruzi chronic infection foci and enteric neuropathic lesions at the tissue micro-domain scale. *PLOS Pathogens* **2021**, *17* (8), e1009864.
(307) Ward, A. I.; Lewis, M. D.; Khan, A. A.; McCann, C. J.; Francisco, A. F.; Jayawardhana, S.; Taylor, M. C.; Kelly, J. M.; Burleigh, B. In Vivo Analysis of Trypanosoma cruzi Persistence Foci at Single-Cell Resolution. *mBio* **2020**, *11* (4), e01242-01220.
(308) Tarleton, R. L. Chagas disease: a role for autoimmunity? *Trends Parasitol* **2003**, *19* (10), 447-451.
(309) Marcon, G. E.; de Albuquerque, D. M.; Batista, A. M.; Andrade, P. D.; Almeida, E. A.; Guariento, M. E.; Teixeira, M. A.; Costa, S. C. Trypanosoma cruzi: parasite persistence in tissues in chronic chagasic Brazilian patients. *Mem Inst Oswaldo Cruz* **2011**, *106* (1), 85-91.
(310) Ward, A. I.; Lewis, M. D.; Taylor, M. C.; Kelly, J. M. Incomplete recruitment of protective T cells facilitates Trypanosoma cruzi persistence in the mouse colon. *bioRxiv* **2021**, 2021.2002.2026.433032.
(311) Buckner, F. S.; Verlinde, C. L.; Flamme, A. C. L.; Voorhis, W. C. V. Efficient technique for screening drugs for activity against Trypanosoma cruzi using parasites expressing beta-galactosidase. *Antimicrobial Agents and Chemotherapy* **1996**, *40* (11), 2592-2597.
(312) Buckner, F. S.; Wilson, A. J.; Van Voorhis, W. C. Detection of live Trypanosoma cruzi in tissues of infected mice by using histochemical stain for beta-galactosidase. *Infect Immun* **1999**, *67* (1), 403-409.
(313) Higuchi Mde, L.; De Brito, T.; Martins Reis, M.; Barbosa, A.; Bellotti, G.; Pereira-Barreto, A. C.; Pileggi, F. Correlation between Trypanosoma cruzi parasitism and myocardial inflammatory infiltrate in human chronic chagasic myocarditis: Light microscopy and immunohistochemical findings. *Cardiovasc Pathol* **1993**, *2* (2), 101-106.
(314) Silva, R. R. d.; Dorrestein, P. C.; Quinn, R. A. Illuminating the dark matter in metabolomics. *Proceedings of the National Academy of Sciences* **2015**, *112* (41), 12549-12550.
(315) Gazos-Lopes, F.; Martin, J. L.; Dumoulin, P. C.; Burleigh, B. A. Host triacylglycerols shape the lipidome of intracellular trypanosomes and modulate their growth. *PLOS Pathogens* **2017**, *13* (12), e1006800.
(316) Vakil, N. H.; Fujinami, N.; Shah, P. J. Pharmacotherapy for Leishmaniasis in the United States: Focus on Miltefosine. *Pharmacotherapy: The Journal of Human Pharmacology and Drug Therapy* **2015**, *35* (5), 536-545.
(317) Sales Junior, P. A.; Molina, I.; Fonseca Murta, S. M.; Sánchez-Montalvá, A.; Salvador, F.; Corrêa-Oliveira, R.; Carneiro, C. M. Experimental and Clinical Treatment of Chagas Disease: A Review. *Am J Trop Med Hyg* **2017**, *97* (5), 1289-1303.
(318) Shah-Simpson, S.; Lentini, G.; Dumoulin, P. C.; Burleigh, B. A. Modulation of host central carbon metabolism and in situ glucose uptake by intracellular Trypanosoma cruzi amastigotes. *PLoS Pathog* **2017**, *13* (11), e1006747.
(319) Malafaia, G.; Talvani, A. Nutritional Status Driving Infection by Trypanosoma cruzi: Lessons from Experimental Animals. *J Trop Med* **2011**, *2011*, 981879.

(320) Morillo, C. A.; Marin-Neto, J. A.; Avezum, A.; Sosa-Estani, S.; Rassi, A., Jr.; Rosas, F.; Villena, E.; Quiroz, R.; Bonilla, R.; Britto, C.; et al. Randomized Trial of Benznidazole for Chronic Chagas' Cardiomyopathy. *N Engl J Med* **2015**, *373* (14), 1295-1306.
(321) Altschuler, S. J.; Wu, L. F. Cellular heterogeneity: do differences make a difference? *Cell* **2010**, *141* (4), 559-563.
(322) Barh, D.; Azevedo, V. Single-cell omics. Volume 2, Applications in biomedicine and agriculture : technological advances and applications: (Applications in biomedicine and agriculture); *London: Academic Press*, **2019**.
(323) Dagogo-Jack, I.; Shaw, A. T. Tumour heterogeneity and resistance to cancer therapies. *Nat Rev Clin Oncol* **2018**, *15* (2), 81-94.
(324) Sun, X. X.; Yu, Q. Intra-tumor heterogeneity of cancer cells and its implications for cancer treatment. *Acta Pharmacol Sin* **2015**, *36* (10), 1219-1227.
(325) Stanta, G.; Bonin, S. Overview on Clinical Relevance of Intra-Tumor Heterogeneity. *Front Med (Lausanne)* **2018**, *5*, 85.
(326) Qian, M.; Wang, D. C.; Chen, H.; Cheng, Y. Detection of single cell heterogeneity in cancer. *Semin Cell Dev Biol* **2017**, *64*, 143-149.
(327) Wilmore, J. R.; Jones, D. D.; Allman, D. Protocol for improved resolution of plasma cell subpopulations by flow cytometry. *Eur J Immunol* **2017**, *47* (8), 1386-1388.
(328) Slack, M. D.; Martinez, E. D.; Wu, L. F.; Altschuler, S. J. Characterizing heterogeneous cellular responses to perturbations. *Proc Natl Acad Sci U S A* **2008**, *105* (49), 19306-19311.
(329) Kashtan, N.; Roggensack, S. E.; Rodrigue, S.; Thompson, J. W.; Biller, S. J.; Coe, A.; Ding, H.; Marttinen, P.; Malmstrom, R. R.; Stocker, R.; et al. Single-cell genomics reveals hundreds of coexisting subpopulations in wild Prochlorococcus. *Science* **2014**, *344* (6182), 416-420.
(330) Nguyen, Q. H.; Pervolarakis, N.; Blake, K.; Ma, D.; Davis, R. T.; James, N.; Phung, A. T.; Willey, E.; Kumar, R.; Jabart, E.; et al. Profiling human breast epithelial cells using single cell RNA sequencing identifies cell diversity. *Nature communications* **2018**, *9* (1), 2028-2028.
(331) Buettner, F.; Natarajan, K. N.; Casale, F. P.; Proserpio, V.; Scialdone, A.; Theis, F. J.; Teichmann, S. A.; Marioni, J. C.; Stegle, O. Computational analysis of cell-to-cell heterogeneity in single-cell RNA-sequencing data reveals hidden subpopulations of cells. *Nat Biotechnol* **2015**, *33* (2), 155-160.
(332) Kang, C. C.; Lin, J. M.; Xu, Z.; Kumar, S.; Herr, A. E. Single-cell Western blotting after whole-cell imaging to assess cancer chemotherapeutic response. *Anal Chem* **2014**, *86* (20), 10429-10436.
(333) Ibáñez, A. J.; Fagerer, S. R.; Schmidt, A. M.; Urban, P. L.; Jefimovs, K.; Geiger, P.; Dechant, R.; Heinemann, M.; Zenobi, R. Mass spectrometry-based metabolomics of single yeast cells. *Proc Natl Acad Sci U S A* **2013**, *110* (22), 8790-8794.
(334) Chen, G.; Ning, B.; Shi, T. Single-Cell RNA-Seq Technologies and Related Computational Data Analysis. *Frontiers in Genetics* **2019**, *10*.
(335) Hwang, B.; Lee, J. H.; Bang, D. Author Correction: Single-cell RNA sequencing technologies and bioinformatics pipelines. *Exp Mol Med* **2021**, *53* (5), 1005.
(336) Weisenfeld, N. I.; Kumar, V.; Shah, P.; Church, D. M.; Jaffe, D. B. Corrigendum: Direct determination of diploid genome sequences. *Genome Res* **2018**, *28* (4), 606.
(337) Butler, A.; Hoffman, P.; Smibert, P.; Papalexi, E.; Satija, R. Integrating single-cell transcriptomic data across different conditions, technologies, and species. *Nature Biotechnology* **2018**, *36* (5), 411-420.
(338) Li, H.; Courtois, E. T.; Sengupta, D.; Tan, Y.; Chen, K. H.; Goh, J. J. L.; Kong, S. L.; Chua, C.; Hon, L. K.; Tan, W. S.; et al. Author Correction: Reference component analysis of single-cell transcriptomes elucidates

cellular heterogeneity in human colorectal tumors. *Nature Genetics* **2018**, *50* (12), 1754-1754.
(339) Ji, Z.; Ji, H. TSCAN: Pseudo-time reconstruction and evaluation in single-cell RNA-seq analysis. *Nucleic Acids Research* **2016**, *44* (13), e117-e117.
(340) Smalley, I.; Chen, Z.; Phadke, M.; Li, J.; Yu, X.; Wyatt, C.; Evernden, B.; Messina, J. L.; Sarnaik, A.; Sondak, V. K.; et al. Single-Cell Characterization of the Immune Microenvironment of Melanoma Brain and Leptomeningeal Metastases. *Clin Cancer Res* **2021**, *27* (14), 4109-4125.
(341) Agüi-Gonzalez, P.; Jähne, S.; Phan, N. T. N. SIMS imaging in neurobiology and cell biology. *Journal of Analytical Atomic Spectrometry* **2019**, *34* (7), 1355-1368.
(342) Amantonico, A.; Urban, P. L.; Fagerer, S. R.; Balabin, R. M.; Zenobi, R. Single-Cell MALDI-MS as an Analytical Tool for Studying Intrapopulation Metabolic Heterogeneity of Unicellular Organisms. *Analytical Chemistry* **2010**, *82* (17), 7394-7400.
(343) Chen, Y.; Li, G.; Yuan, S.; Pan, Y.; Liu, Y.; Huang, G. Ultrafast Microelectrophoresis: Behind Direct Mass Spectrometry Measurements of Proteins and Metabolites in Living Cell/Cells. *Analytical Chemistry* **2019**, *91* (16), 10441-10447.
(344) Nakashima, T.; Wada, H.; Morita, S.; Erra-Balsells, R.; Hiraoka, K.; Nonami, H. Single-Cell Metabolite Profiling of Stalk and Glandular Cells of Intact Trichomes with Internal Electrode Capillary Pressure Probe Electrospray Ionization Mass Spectrometry. *Analytical Chemistry* **2016**, *88* (6), 3049-3057.
(345) Passarelli, M. K.; Newman, C. F.; Marshall, P. S.; West, A.; Gilmore, I. S.; Bunch, J.; Alexander, M. R.; Dollery, C. T. Single-Cell Analysis: Visualizing Pharmaceutical and Metabolite Uptake in Cells with Label-Free 3D Mass Spectrometry Imaging. *Anal Chem* **2015**, *87* (13), 6696-6702.
(346) Stopka, S. A.; Khattar, R.; Agtuca, B. J.; Anderton, C. R.; Pasa-Tolic, L.; Stacey, G.; Vertes, A. Metabolic Noise and Distinct Subpopulations Observed by Single Cell LAESI Mass Spectrometry of Plant Cells in situ. *Frontiers in Plant Science* **2018**, *9*.
(347) Pevsner-Fischer, M.; Levin, S.; Zipori, D. The origins of mesenchymal stromal cell heterogeneity. *Stem Cell Rev Rep* **2011**, *7* (3), 560-568.
(348) Auerbach, R.; Plendl, J.; Kusha, B. Endothelial Cell Heterogeneity and Differentiation. In *Angiogenesis in Health and Disease*, Maragoudakis, M. E., Gullino, P., Lelkes, P. I. Eds.; Springer US, 1992; pp 55-62.
(349) Marklein, R. A.; Klinker, M. W.; Drake, K. A.; Polikowsky, H. G.; Lessey-Morillon, E. C.; Bauer, S. R. Morphological profiling using machine learning reveals emergent subpopulations of interferon-γ-stimulated mesenchymal stromal cells that predict immunosuppression. *Cytotherapy* **2019**, *21* (1), 17-31.
(350) Wang, H.; Sridhar, B.; Leinwand, L. A.; Anseth, K. S. Characterization of Cell Subpopulations Expressing Progenitor Cell Markers in Porcine Cardiac Valves. *PLOS ONE* **2013**, *8* (7), e69667.
(351) Zhang, L.; Sevinsky, C. J.; Davis, B. M.; Vertes, A. Single-Cell Mass Spectrometry of Subpopulations Selected by Fluorescence Microscopy. *Analytical Chemistry* **2018**, *90* (7), 4626-4634.
(352) Stopka, S. A.; Khattar, R.; Agtuca, B. J.; Anderton, C. R.; Paša-Tolić, L.; Stacey, G.; Vertes, A. Metabolic Noise and Distinct Subpopulations Observed by Single Cell LAESI Mass Spectrometry of Plant Cells in situ. *Front Plant Sci* **2018**, *9*, 1646.
(353) Smalley, K. S. M.; Haass, N. K.; Brafford, P. A.; Lioni, M.; Flaherty, K. T.; Herlyn, M. Multiple signaling pathways must be targeted to overcome drug resistance in cell lines derived from melanoma metastases. *Molecular Cancer Therapeutics* **2006**, *5* (5), 1136-1144.
(354) Helmbach, H.; Rossmann, E.; Kern, M. A.; Schadendorf, D. Drug-resistance in human melanoma. *Int J Cancer* **2001**, *93* (5), 617-622.
(355) Liu, R.; Zhang, G.; Yang, Z. Towards rapid prediction of drug-resistant cancer cell phenotypes: single cell mass spectrometry combined with machine learning. *Chemical communications* **2019**, *55* (5), 616-619.

(356) Wehrens, R.; Hageman, J. A.; van Eeuwijk, F.; Kooke, R.; Flood, P. J.; Wijnker, E.; Keurentjes, J. J.; Lommen, A.; van Eekelen, H. D.; Hall, R. D.; et al. Improved batch correction in untargeted MS-based metabolomics. *Metabolomics* **2016**, *12*, 88.
(357) Salerno, S., Jr.; Mehrmohamadi, M.; Liberti, M. V.; Wan, M.; Wells, M. T.; Booth, J. G.; Locasale, J. W. RRmix: A method for simultaneous batch effect correction and analysis of metabolomics data in the absence of internal standards. *PLOS ONE* **2017**, *12* (6), e0179530.
(358) Liu, R.; Zhang, G.; Sun, M.; Pan, X.; Yang, Z. Integrating a generalized data analysis workflow with the Single-probe mass spectrometry experiment for single cell metabolomics. *Anal Chim Acta* **2019**, *1064*, 71-79.
(359) Li, J.; Smalley, I.; Schell, M. J.; Smalley, K. S. M.; Chen, Y. A. SinCHet: a MATLAB toolbox for single cell heterogeneity analysis in cancer. *Bioinformatics* **2017**, *33* (18), 2951-2953.
(360) Johnson, W. E.; Li, C.; Rabinovic, A. Adjusting batch effects in microarray expression data using empirical Bayes methods. *Biostatistics* **2006**, *8* (1), 118-127.
(361) Zhang, L. W.; Sevinsky, C. J.; Davis, B. M.; Vertes, A. Single-Cell Mass Spectrometry of Subpopulations Selected by Fluorescence Microscopy. *Anal. Chem.* **2018**, *90* (7), 4626-4634.
(362) Beger, R. D. A review of applications of metabolomics in cancer. *Metabolites* **2013**, *3* (3), 552-574.
(363) Zhang, Y.; Liu, P.; Li, Y.; Zhang, A.-H. Exploration of metabolite signatures using high-throughput mass spectrometry coupled with multivariate data analysis. *RSC Advances* **2017**, *7* (11), 6780-6787.
(364) Onjiko, R. M.; Moody, S. A.; Nemes, P. Single-cell mass spectrometry reveals small molecules that affect cell fates in the 16-cell embryo. *Proc Natl Acad Sci U S A* **2015**, *112* (21), 6545-6550.
(365) Zhu, H.; Zou, G.; Wang, N.; Zhuang, M.; Xiong, W.; Huang, G. Single-neuron identification of chemical constituents, physiological changes, and metabolism using mass spectrometry. *Proceedings of the National Academy of Sciences* **2017**, *114* (10), 2586-2591.
(366) Sillence, D. Lipid rafts : properties, controversies and roles in signal transduction; **2014**.
(367) Rowinsky, E. K. Signal events: Cell signal transduction and its inhibition in cancer. *Oncologist* **2003**, *8 Suppl 3*, 5-17.
(368) Jang, C.; Chen, L.; Rabinowitz, J. D. Metabolomics and Isotope Tracing. *Cell* **2018**, *173* (4), 822-837.
(369) Morgan, G.; Ward, R.; Barton, M. The contribution of cytotoxic chemotherapy to 5-year survival in adult malignancies. *Clinical oncology* **2004**, *16* (8), 549-560.
(370) Gottesman, M. M. Mechanisms of cancer drug resistance. *Annual review of medicine* **2002**, *53* (1), 615-627.
(371) Sharma, P.; Hu-Lieskovan, S.; Wargo, J. A.; Ribas, A. Primary, adaptive, and acquired resistance to cancer immunotherapy. *Cell* **2017**, *168* (4), 707-723.
(372) Foo, J.; Michor, F. Evolution of acquired resistance to anti-cancer therapy. *Journal of theoretical biology* **2014**, *355*, 10-20.
(373) Alfarouk, K. O.; Stock, C.-M.; Taylor, S.; Walsh, M.; Muddathir, A. K.; Verduzco, D.; Bashir, A. H.; Mohammed, O. Y.; Elhassan, G. O.; Harguindey, S. Resistance to cancer chemotherapy: failure in drug response from ADME to P-gp. *Cancer cell international* **2015**, *15* (1), 1-13.
(374) Luqmani, Y. Mechanisms of drug resistance in cancer chemotherapy. *Medical principles and practice* **2005**, *14* (Suppl. 1), 35-48.
(375) Ames, V.; Britton, P. D. Stereotactically guided breast biopsy: a review. *Insights into imaging* **2011**, *2* (2), 171-176.
(376) Fei, B.; Schuster, D. M. PET molecular imaging–directed biopsy: a review. *AJR. American journal of roentgenology* **2017**, *209* (2), 255.

(377) Liang, X. J.; Shen, D. W.; Chen, K. G.; Wincovitch, S. M.; Garfield, S. H.; Gottesman, M. M. Trafficking and localization of platinum complexes in cisplatin-resistant cell lines monitored by fluorescence-labeled platinum. *Journal of cellular physiology* **2005**, *202* (3), 635-641.
(378) Lin, G.; Mi, P.; Chu, C.; Zhang, J.; Liu, G. Inorganic nanocarriers overcoming multidrug resistance for cancer theranostics. *Advanced science* **2016**, *3* (11), 1600134.
(379) Paguio, M. F.; Cabrera, M.; Roepe, P. D. Chloroquine transport in Plasmodium falciparum. 2. Analysis of PfCRT-mediated drug transport using proteoliposomes and a fluorescent chloroquine probe. *Biochemistry* **2009**, *48* (40), 9482-9491.
(380) Liang, L.; Jin, Y.; Zhu, X.; Zhou, F.; Yang, Y. Real-time detection and monitoring of the drug resistance of single myeloid leukemia cells by diffused total internal reflection. *Lab on a Chip* **2018**, *18* (10), 1422-1429.
(381) Tellez-Gabriel, M.; Ory, B.; Lamoureux, F.; Heymann, M.-F.; Heymann, D. Tumour heterogeneity: the key advantages of single-cell analysis. *International journal of molecular sciences* **2016**, *17* (12), 2142.
(382) Lippert, T. H.; Ruoff, H.-J.; Volm, M. Current status of methods to assess cancer drug resistance. *International journal of medical sciences* **2011**, *8* (3), 245.
(383) Diaz Jr, L. A.; Williams, R. T.; Wu, J.; Kinde, I.; Hecht, J. R.; Berlin, J.; Allen, B.; Bozic, I.; Reiter, J. G.; Nowak, M. A. The molecular evolution of acquired resistance to targeted EGFR blockade in colorectal cancers. *Nature* **2012**, *486* (7404), 537-540.
(384) Muir, A.; Danai, L. V.; Vander Heiden, M. G. Microenvironmental regulation of cancer cell metabolism: implications for experimental design and translational studies. *Disease models & mechanisms* **2018**, *11* (8), dmm035758.
(385) Worley, B.; Powers, R. Multivariate analysis in metabolomics. *Current metabolomics* **2013**, *1* (1), 92-107.
(386) Xi, B.; Gu, H.; Baniasadi, H.; Raftery, D. Statistical analysis and modeling of mass spectrometry-based metabolomics data. *Mass spectrometry in metabolomics: methods and protocols* **2014**, 333-353.
(387) Samaraweera, M. A.; Hall, L. M.; Hill, D. W.; Grant, D. F. Evaluation of an artificial neural network retention index model for chemical structure identification in nontargeted metabolomics. *Analytical chemistry* **2018**, *90* (21), 12752-12760.
(388) Miller, T. H.; Musenga, A.; Cowan, D. A.; Barron, L. P. Prediction of chromatographic retention time in high-resolution anti-doping screening data using artificial neural networks. *Analytical chemistry* **2013**, *85* (21), 10330-10337.
(389) Narath, S. H.; Mautner, S. I.; Svehlikova, E.; Schultes, B.; Pieber, T. R.; Sinner, F. M.; Gander, E.; Libiseller, G.; Schimek, M. G.; Sourij, H. An untargeted metabolomics approach to characterize short-term and long-term metabolic changes after bariatric surgery. *PloS one* **2016**, *11* (9), e0161425.
(390) Matthew, W. Bias of the random forest out-of-bag (OOB) error for certain input parameters. *Open Journal of Statistics* **2011**, *2011*.
(391) Grissa, D.; Pétéra, M.; Brandolini, M.; Napoli, A.; Comte, B.; Pujos-Guillot, E. Feature selection methods for early predictive biomarker discovery using untargeted metabolomic data. *Frontiers in molecular biosciences* **2016**, *3*, 30.
(392) Hinton, D. J.; Vázquez, M. S.; Geske, J. R.; Hitschfeld, M. J.; Ho, A. M.; Karpyak, V. M.; Biernacka, J. M.; Choi, D.-S. Metabolomics biomarkers to predict acamprosate treatment response in alcohol-dependent subjects. *Scientific reports* **2017**, *7* (1), 2496.
(393) Armitage, E. G.; Southam, A. D. Monitoring cancer prognosis, diagnosis and treatment efficacy using metabolomics and lipidomics. *Metabolomics* **2016**, *12*, 1-15.

(394) Zong, L.; Pi, Z.; Liu, S.; Liu, Z.; Song, F. Metabolomics analysis of multidrug-resistant breast cancer cells in vitro using methyl-tert-butyl ether method. *RSC advances* **2018**, *8* (28), 15831-15841.
(395) Nemes, P.; Knolhoff, A. M.; Rubakhin, S. S.; Sweedler, J. V. Metabolic differentiation of neuronal phenotypes by single-cell capillary electrophoresis–electrospray ionization-mass spectrometry. *Analytical chemistry* **2011**, *83* (17), 6810-6817.
(396) Viswan, A.; Singh, C.; Rai, R. K.; Azim, A.; Sinha, N.; Baronia, A. K. Metabolomics based predictive biomarker model of ARDS: A systemic measure of clinical hypoxemia. *PloS one* **2017**, *12* (11), e0187545.
(397) Han, H.; Guo, X.; Yu, H. Variable selection using mean decrease accuracy and mean decrease gini based on random forest. In *2016 7th ieee international conference on software engineering and service science (icsess)*, 2016; IEEE: pp 219-224.
(398) Grund, B.; Sabin, C. Analysis of biomarker data: logs, odds ratios and ROC curves. *Current Opinion in HIV and AIDS* **2010**, *5* (6), 473.
(399) Hand, D. J.; Till, R. J. A simple generalisation of the area under the ROC curve for multiple class classification problems. *Machine learning* **2001**, *45*, 171-186.
(400) Mandrekar, J. N. Receiver operating characteristic curve in diagnostic test assessment. *Journal of Thoracic Oncology* **2010**, *5* (9), 1315-1316.
(401) Valente, M. J.; Henrique, R.; Costa, V. L.; Jerónimo, C.; Carvalho, F.; Bastos, M. L.; de Pinho, P. G.; Carvalho, M. A rapid and simple procedure for the establishment of human normal and cancer renal primary cell cultures from surgical specimens. *PloS one* **2011**, *6* (5), e19337.
(402) Ferreira, C. R.; Yannell, K. E.; Jarmusch, A. K.; Pirro, V.; Ouyang, Z.; Cooks, R. G. Ambient ionization mass spectrometry for point-of-care diagnostics and other clinical measurements. *Clinical chemistry* **2016**, *62* (1), 99-110.

Appendix

A. Figures

Chapter 2.

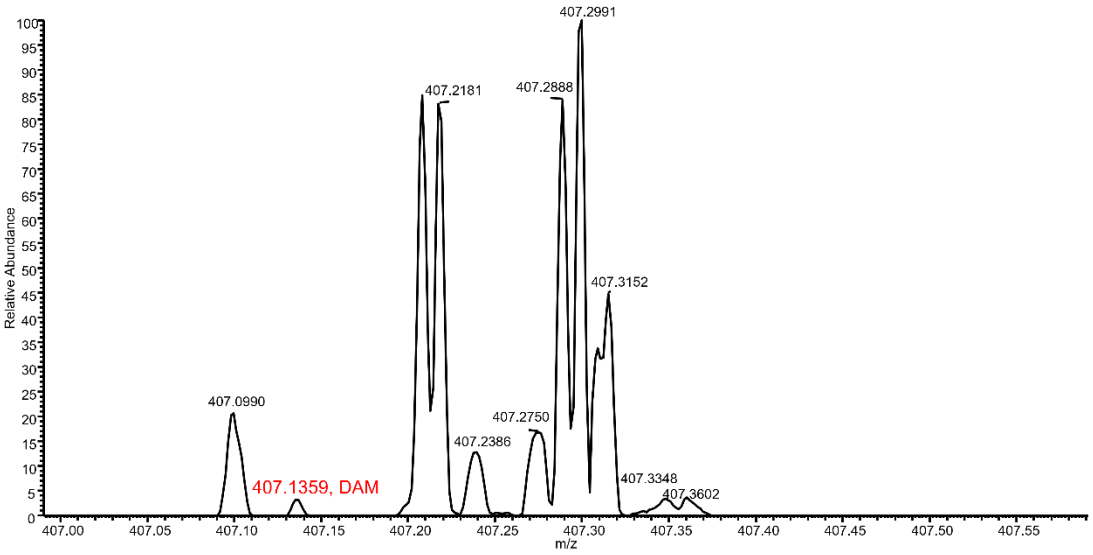

Figure S1. MS1 of DAM and interfering ions.

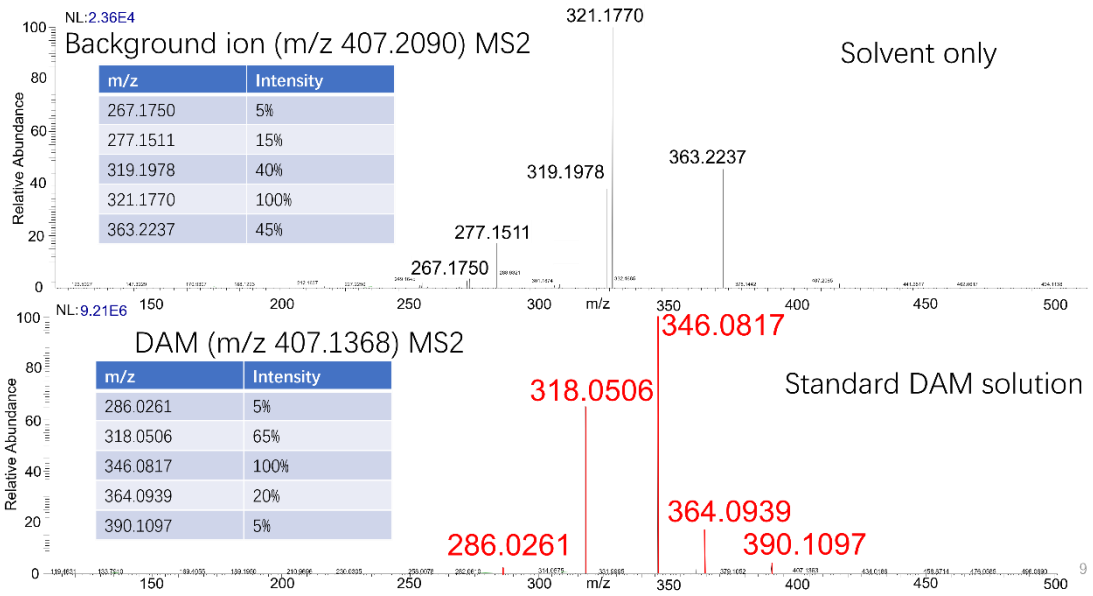

m/z	Intensity
267.1750	5%
277.1511	15%
319.1978	40%
321.1770	100%
363.2237	45%

m/z	Intensity
286.0261	5%
318.0506	65%
346.0817	100%
364.0939	20%
390.1097	5%

Figure S2. MS/MS of interference ions (upper) and DAM solution (lower).

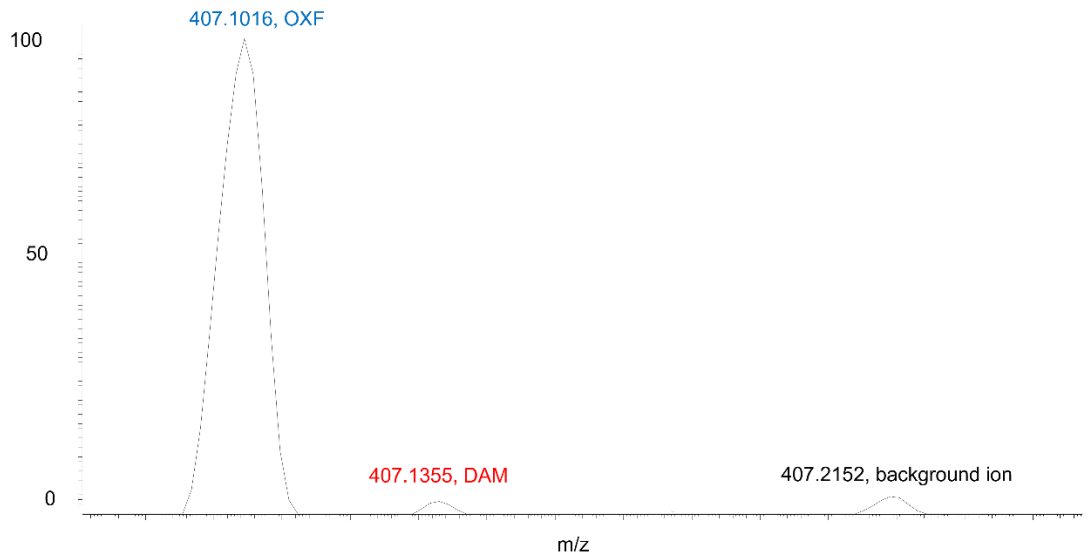

Figure S3. Mass spectrum of DAM and its internal standard (OXF).

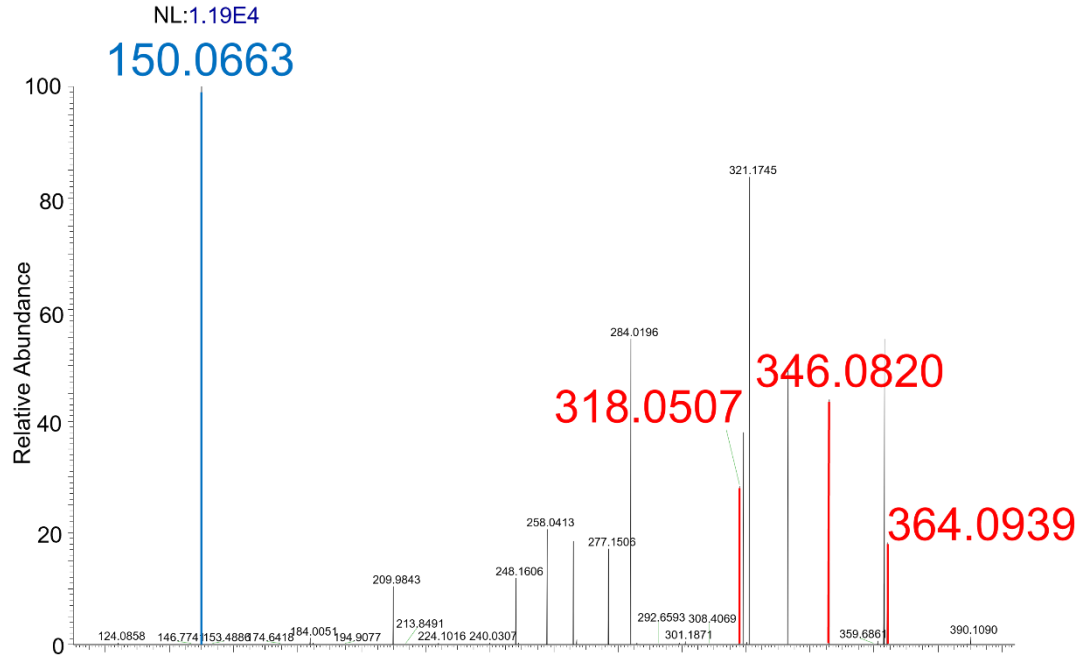

Figure S4. MS/MS of co-isolated $[DAM+H]^+$ (m/z 407.1325) and $[OXF+H]^+$ (m/z 407.1020). Fragment ions of $[DAM+H]^+$ and $[OXF+H]^+$ are highlighted in blue and red, respectively.

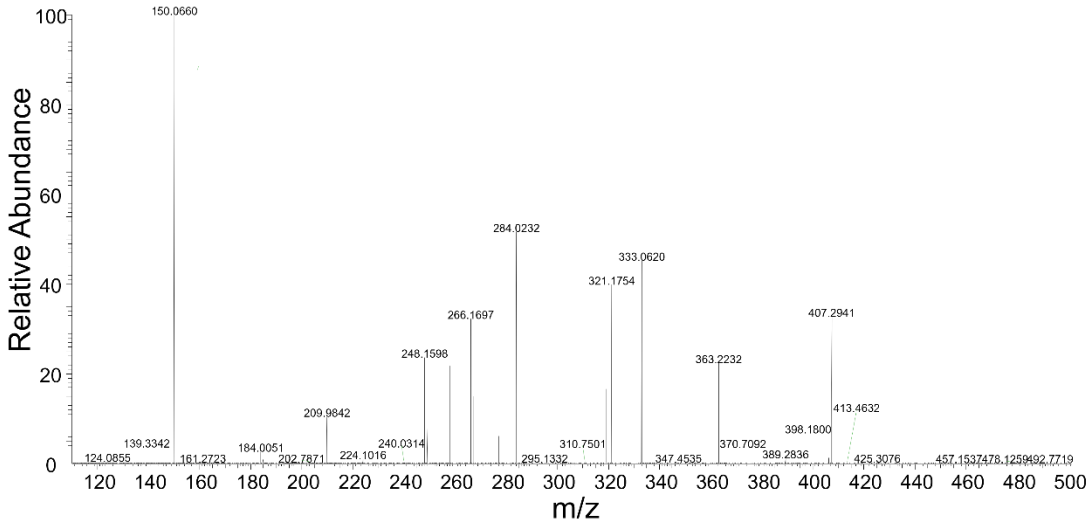

Figure S5. MS/MS of standard OXF solution.

Chapter 3.

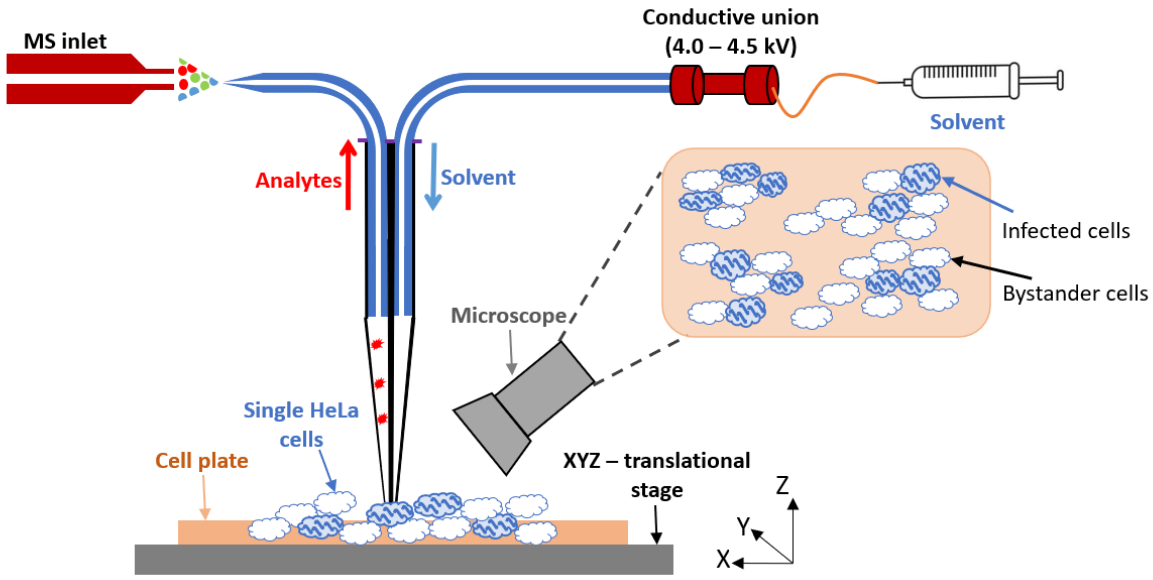

Figure S1. The schematic of the working mechanisms of the Single-probe SCMS experimental set-up.

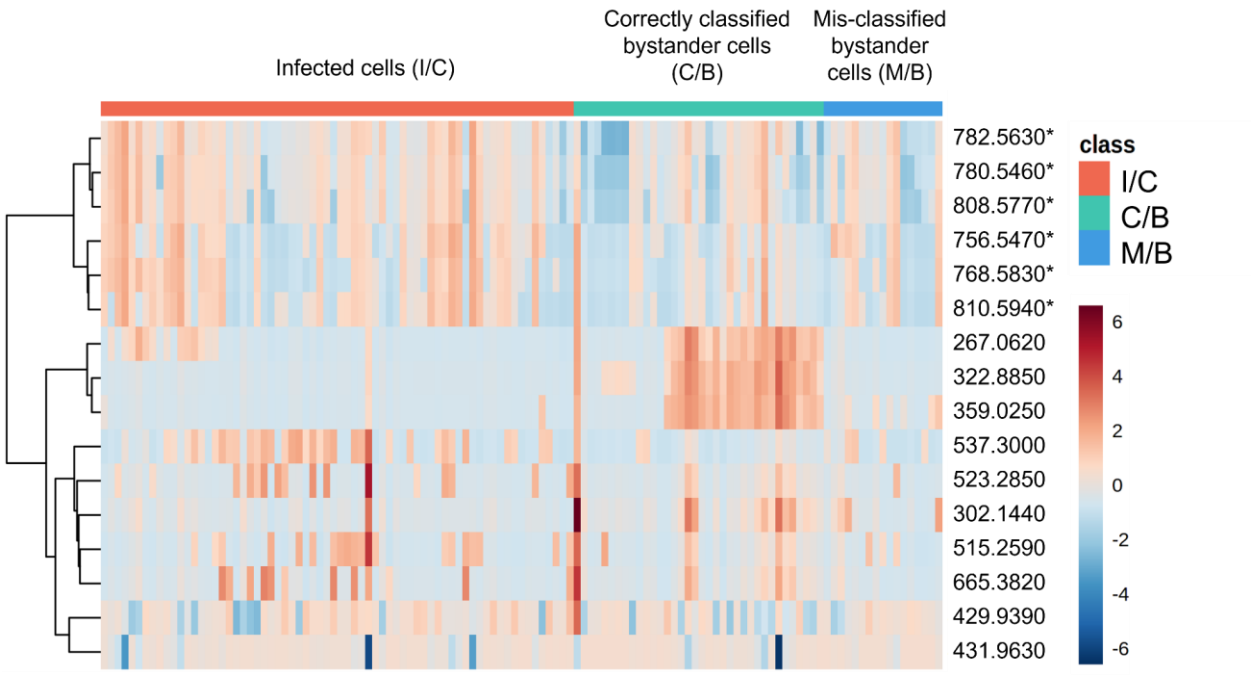

Figure S2: Hierarchical Clustering of metabolite features differing between infected cells (I/C), correctly classified bystander cells (C/B) and mis-classified bystander cells (M/B). The annotated features are marked (*).

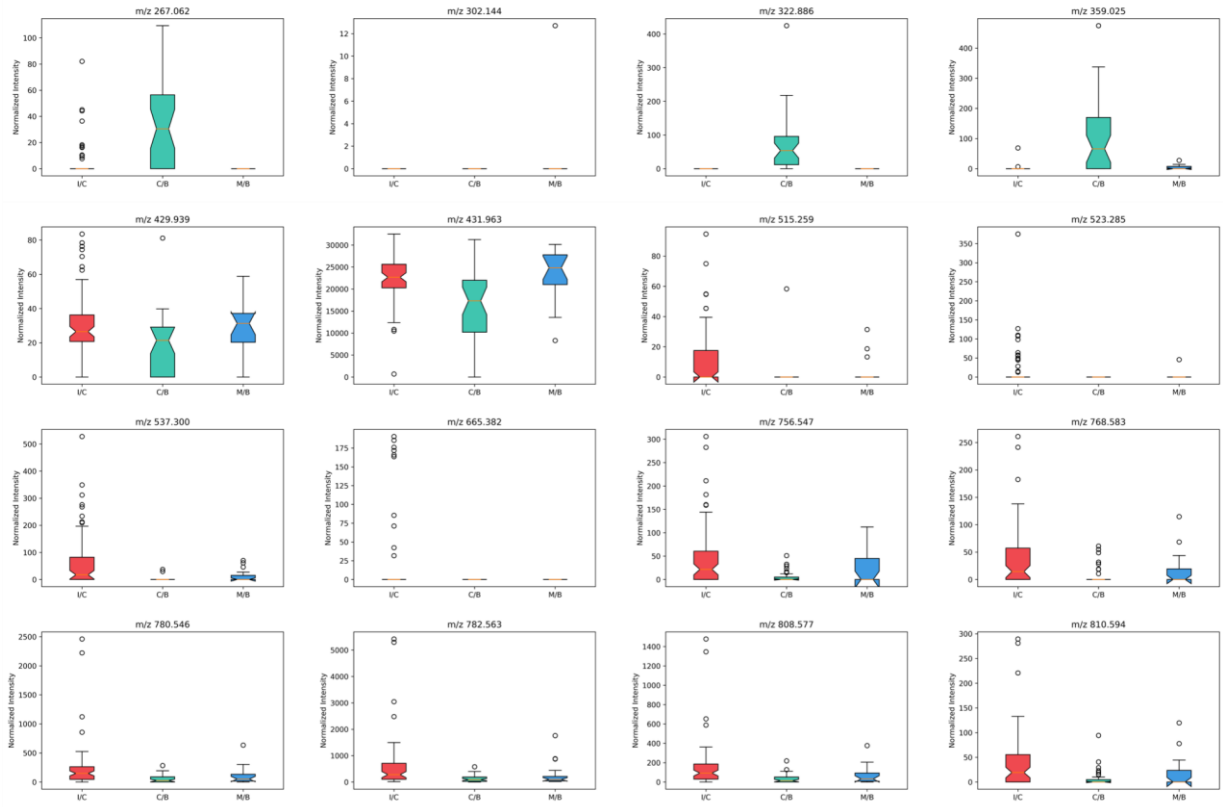

Figure S3. Box plots for 16 metabolites showed comparable behavior in infected cells (I/C) and in mis-classified bystander cells (M/B), as determined by ANOVA test with an adjusted p-value ≤ 0.05.

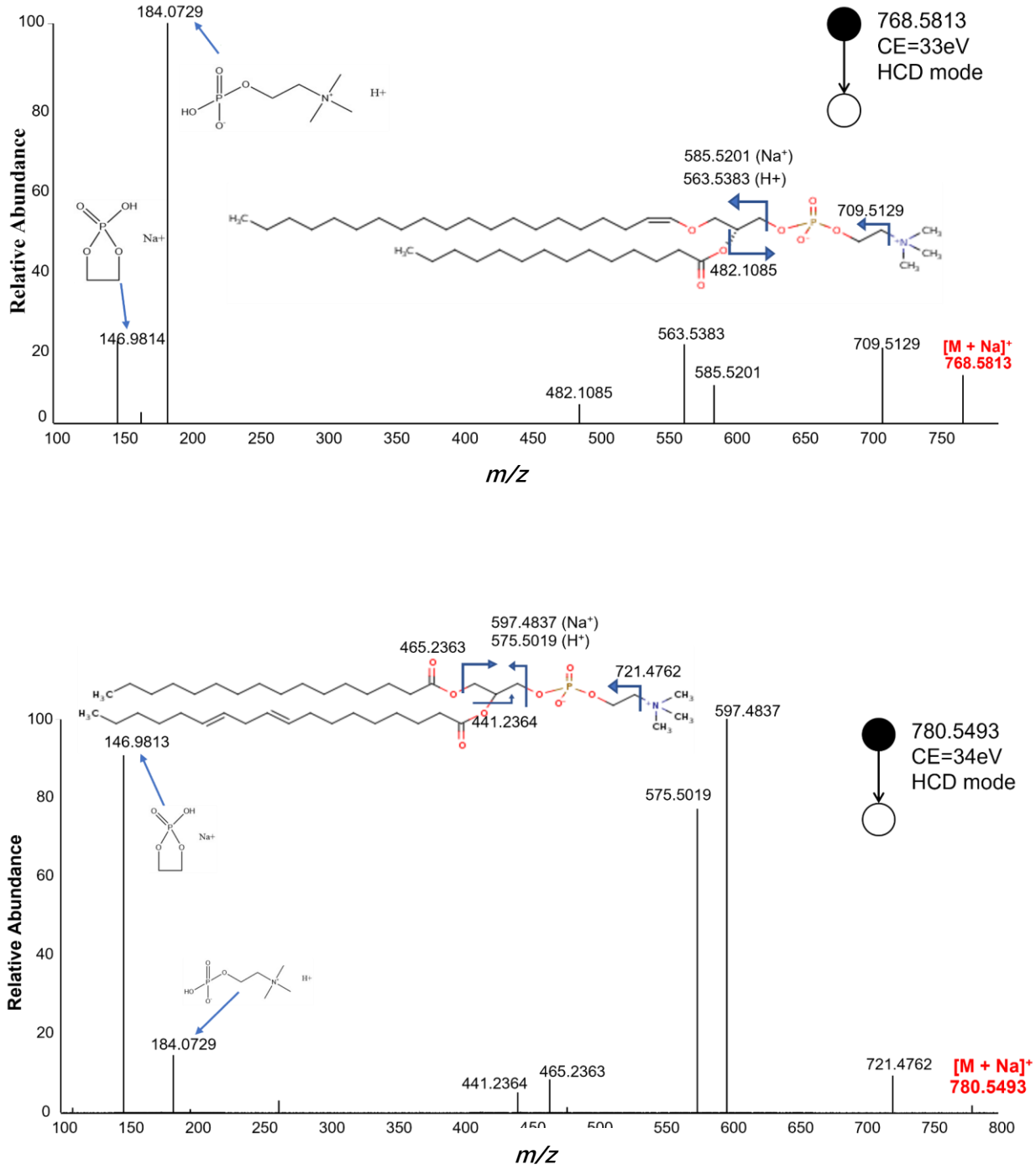

Figure S4. Annotated MS/MS spectra of $[PC(P\text{-}20:0/14:0)+Na]^+$ at *m/z* 768.5813 (upper panel) and $[PC(16:0/18:2)+Na]^+$ at *m/z* 780.5493 (lower panel), acquired from individual HeLa cells. CE: collision energy.

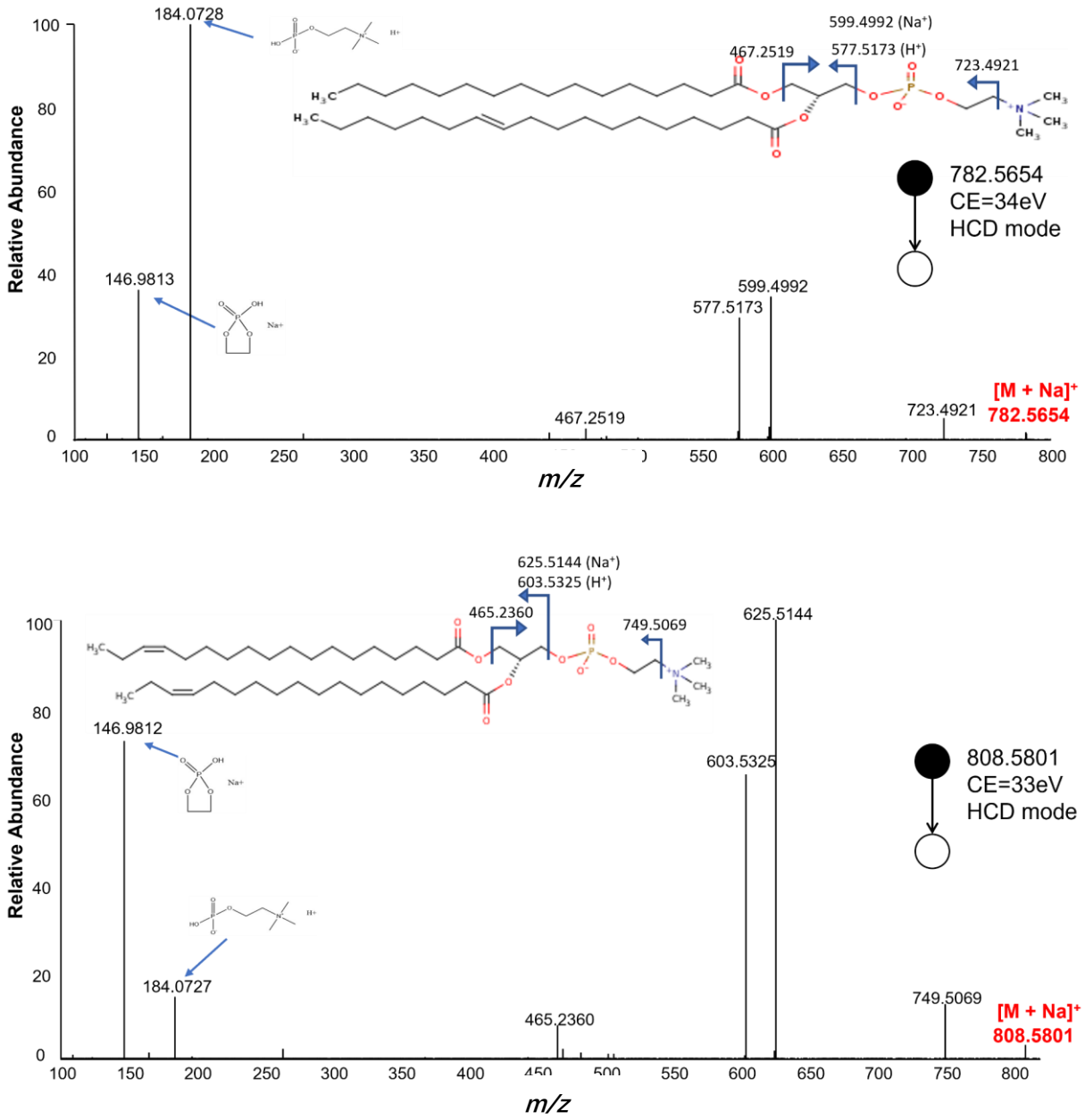

Figure S5. Annotated MS/MS spectra of [PC(16:0/18:1)+Na]$^+$ at *m/z* 782.5654 (upper panel) and [PC(18:1/18:1)+Na]$^+$ at *m/z* 808.5801 (lower panel), acquired from individual HeLa cells. CE: collision energy.

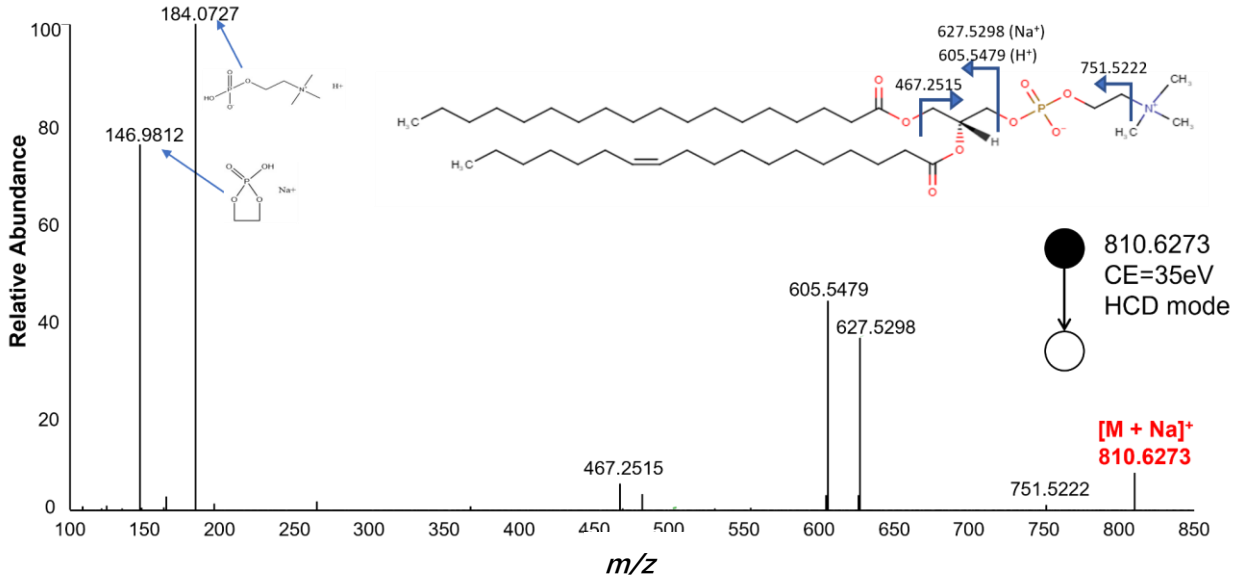

Figure S6. Annotated MS/MS spectrum of $[PC(18:0/18:1)+Na]^+$ at *m/z* 810.6273 from individual HeLa cells. CE: collision energy.

Chapter 4.

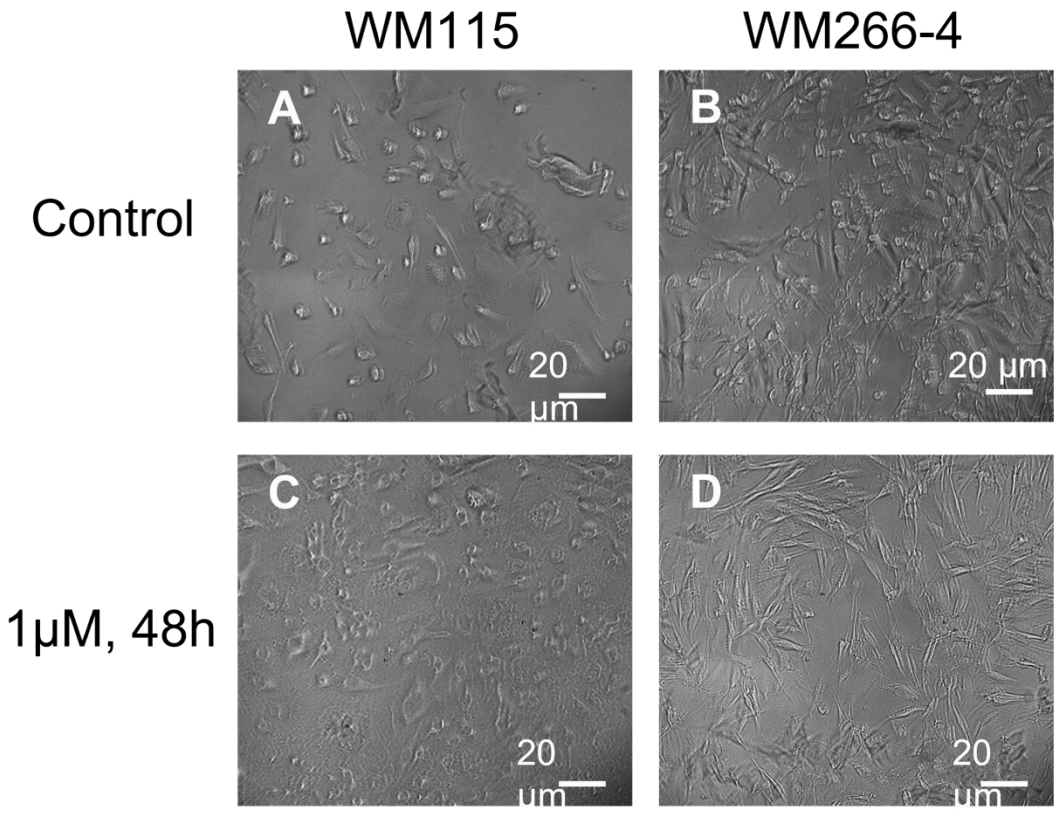

Figure S1. Photos of WM115 (A and C) and WM266-4 (B and D) cells before (A and B) and after treatment (C and D) (1 μM for 48 h).

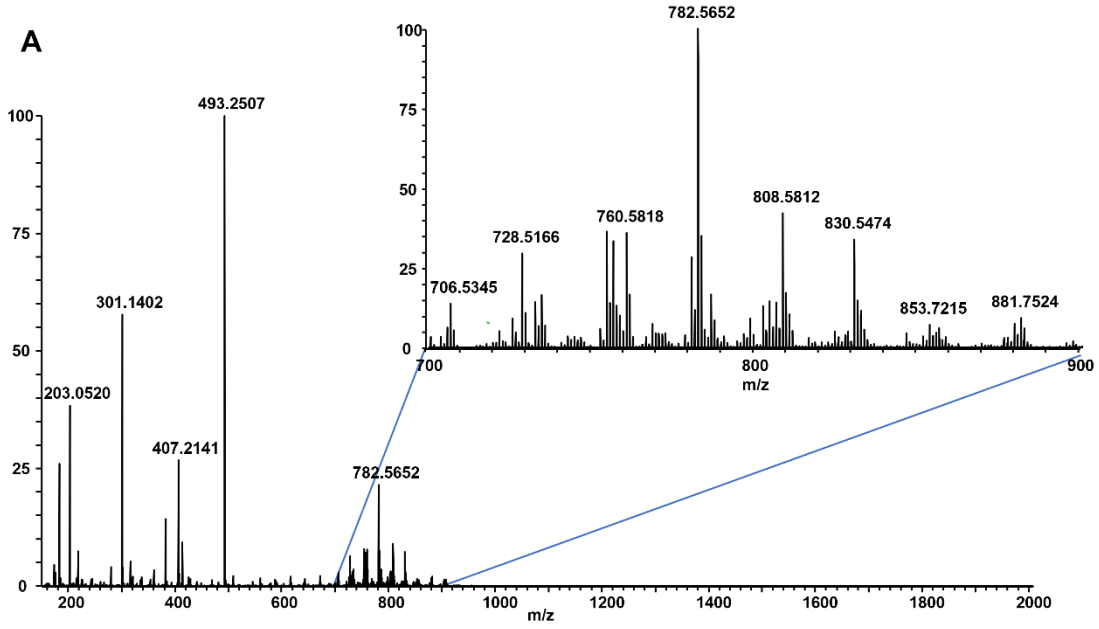
A
493.2507
301.1402
203.0520
407.2141
782.5652
782.5652
808.5812
760.5818
830.5474
728.5166
706.5345
853.7215
881.7524
m/z
m/z

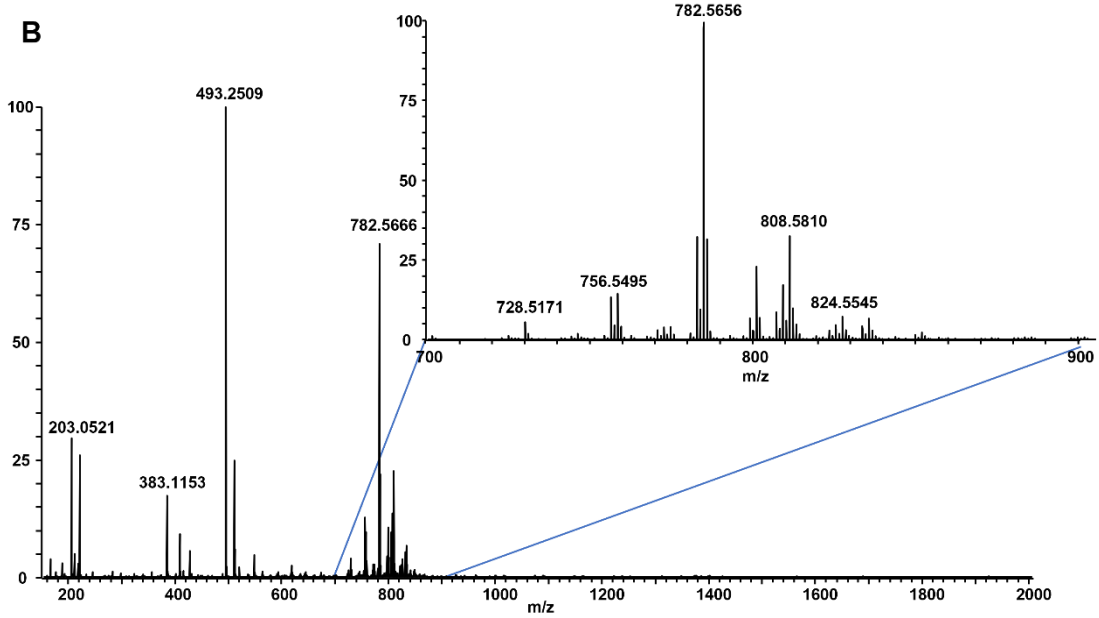
B
493.2509
203.0521
383.1153
782.5656
782.5666
808.5810
756.5495
728.5171
824.5545
m/z
m/z

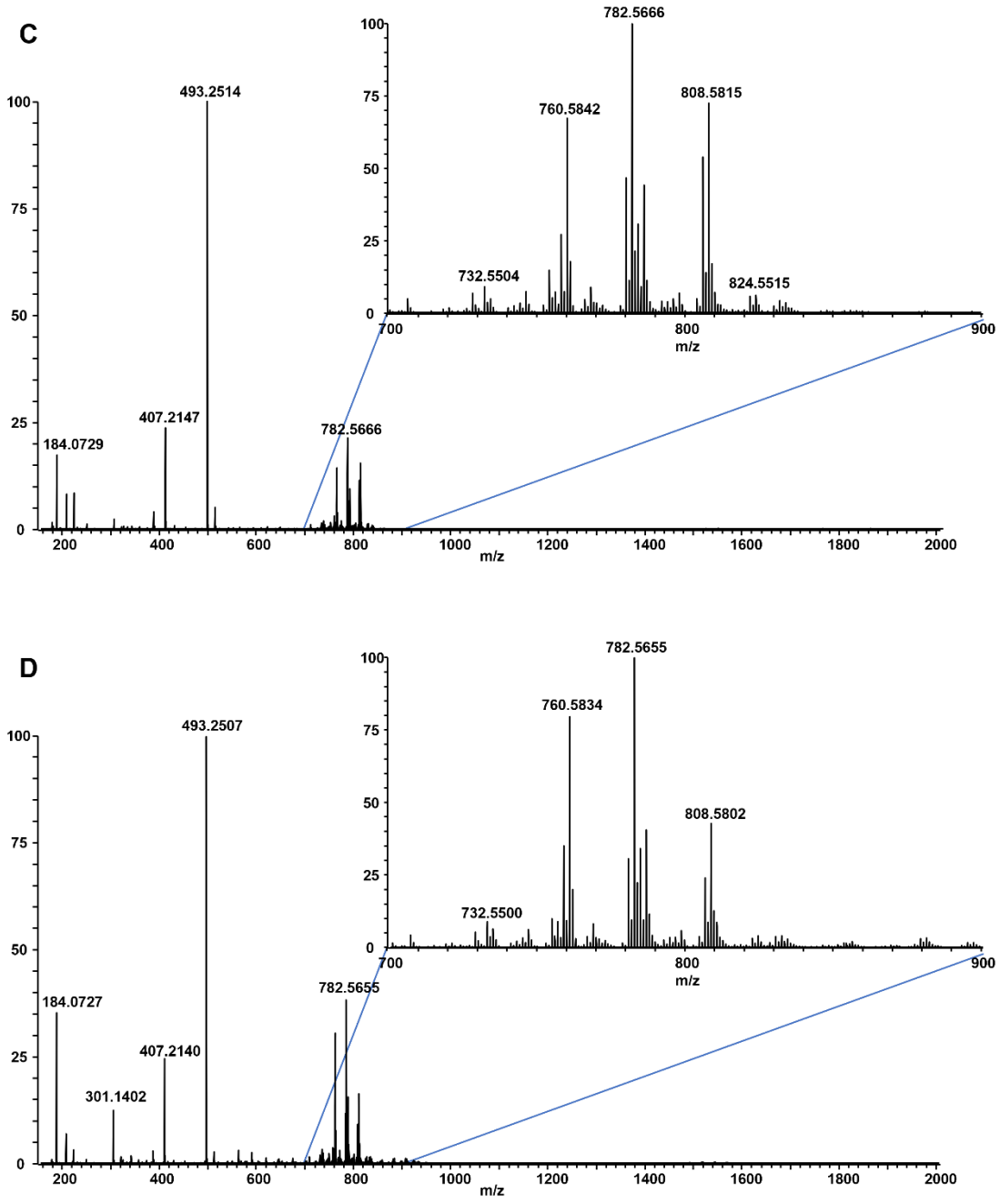

Figure S2. Representative mass spectra of single WM115 (A-B) and WM266-4 (C-D) cells before (A and C) and after treatment (B and D) (1 μM for 48 h). The zoomed-in mass spectra illustrate *m/z* regions with abundant cellular species. Major lipid species including PC 34:1 and PC 36:2 are present in both cell lines before and after treatment with different relative intensity.

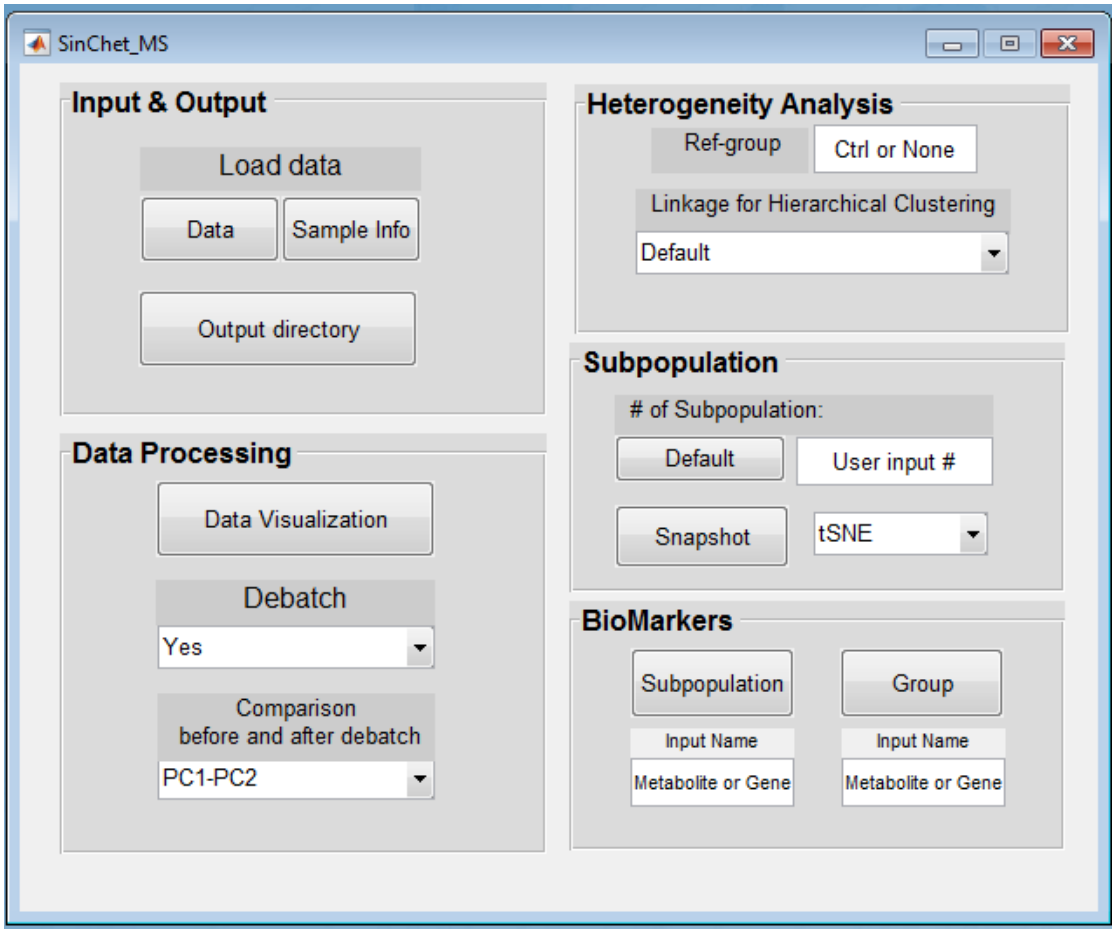

Figure S3. The main Graphic User Interface (GUI) of the SinCHet-MS software package. It integrates functions of debatching, determination and visualization of cell subpopulations and prioritization of subpopulational biomarkers.

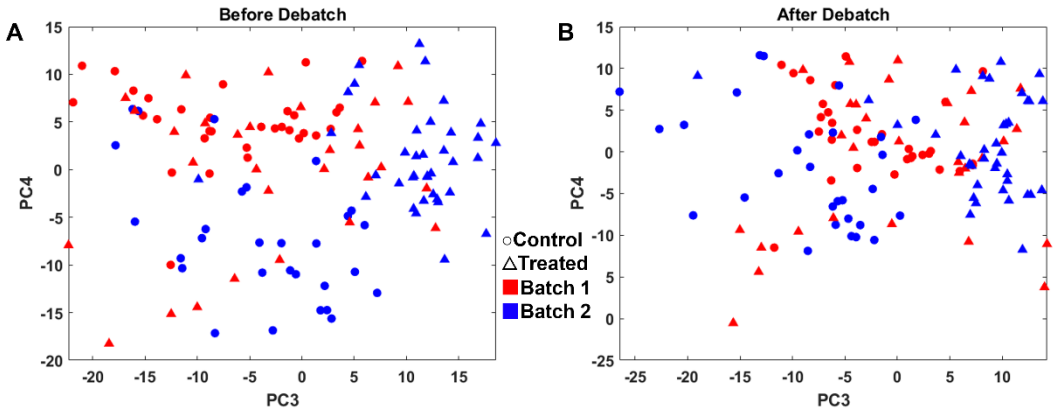

Figure S4. PCA score plots of WM266-4 cells (A) before and (B) after debatching in the PC3 and PC4 dimensions. The shapes of the symbol represent control (○) and treatment (Δ), and the colors of the symbol represent batch 1 (■) and batch 2 (■).

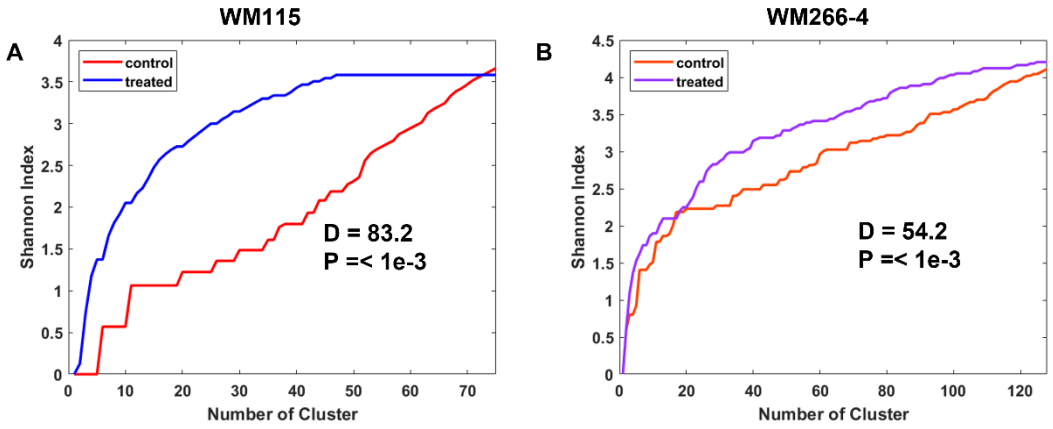

Figure S5. Change of cell heterogeneity before and after drug treatment for the (A) WM115 and (B) WM266-4 cell lines using d-statistics.

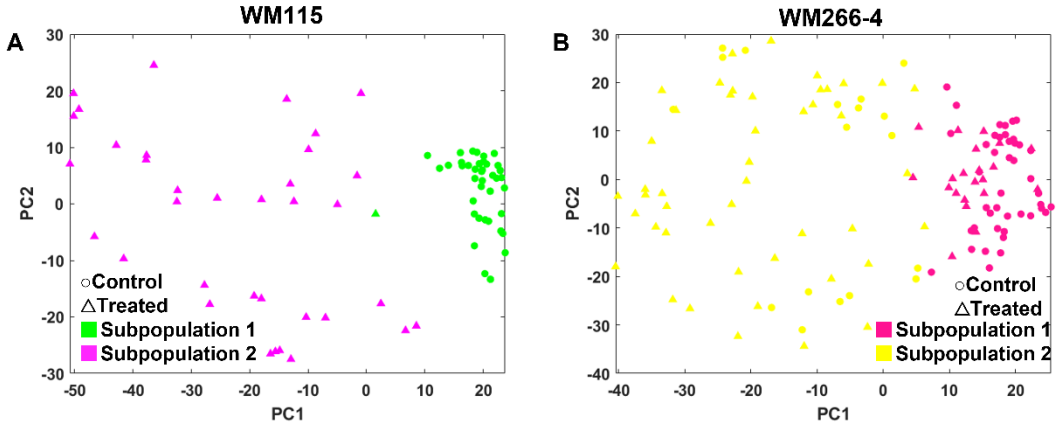

Figure S6. PCA score plots of (A) WM115 and (B) WM266-4 cells classified by subpopulations. The shapes of the symbol represent control (○) and treatment (△), and the colors of the symbol represent batch 1 (■) and batch 2 (■).

A

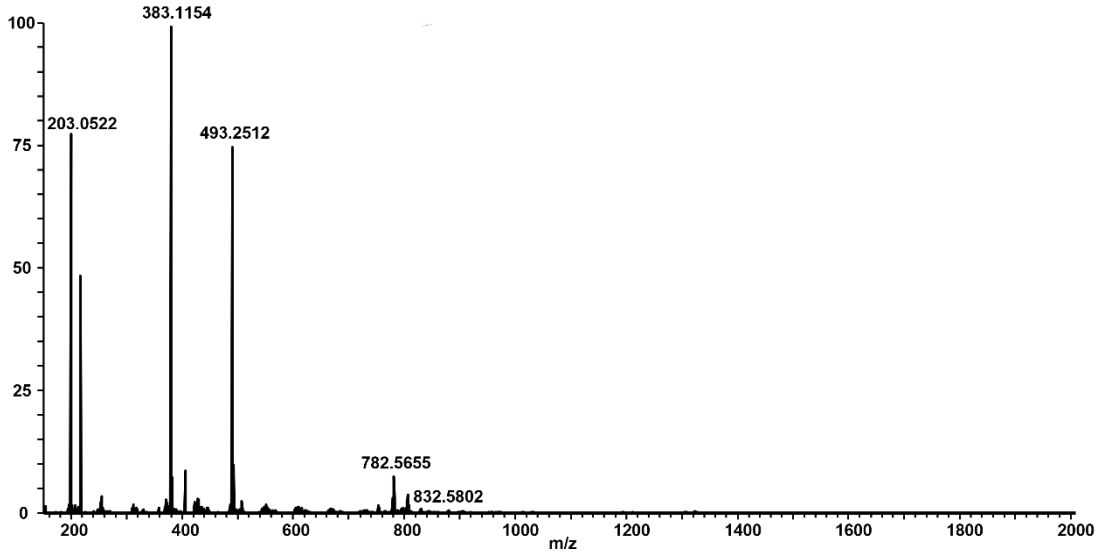
383.1154
203.0522
493.2512
782.5655
832.5802
100
75
50
25
0
200
400
600
800
1000
1200
1400
1600
1800
2000
m/z

B

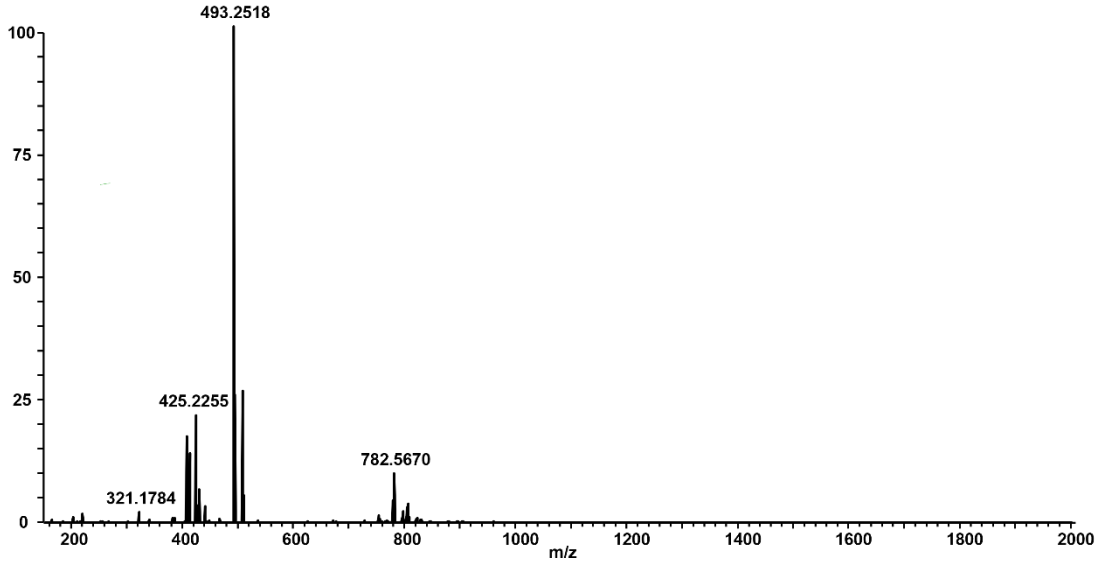
493.2518
425.2255
782.5670
321.1784
100
75
50
25
0
200
400
600
800
1000
1200
1400
1600
1800
2000
m/z

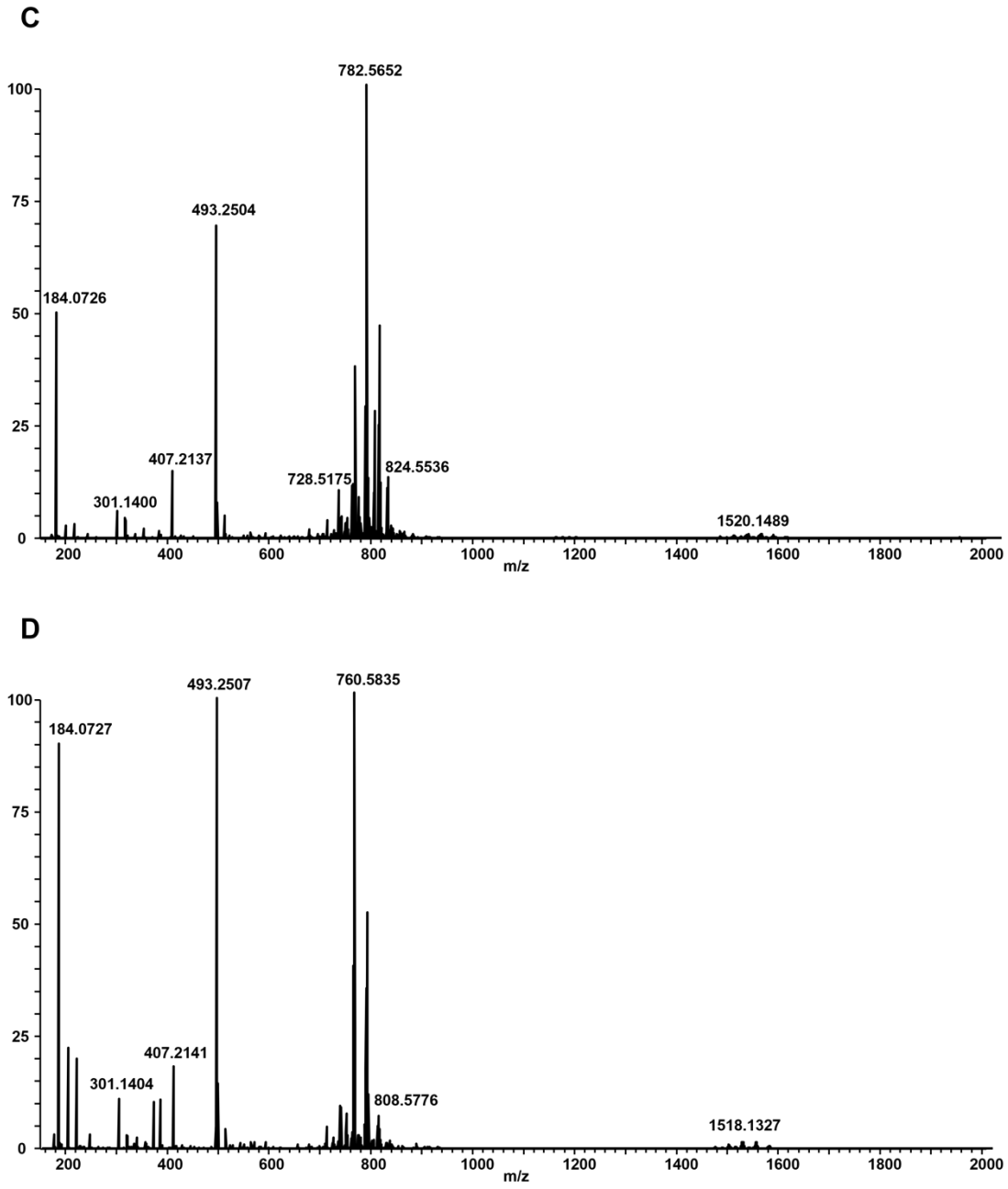

Figure S7. Representative mass spectra of single WM115 (A-B) and WM266-4 (C-D) cells with different subpopulation. (A) Subpopulation 1 of WM115; (B) Subpopulation 2 of WM115; (C) Subpopulation 1 of WM266-4; (D) Subpopulation 2 of WM266-4. Major lipid species including PC 34:1 and PC 36:2 are present in both cell lines before and after treatment with different relative intensity.

B. Tables

Chapter 2.

Table S1. Calibration curve of DAM major fragments

Ions	Regression functions	R square values
Summary	Y = 141.37X + 0.0809	0.9914
318.05	Y = 37.36X + 0.0329	0.9939
346.08	Y = 78.15X + 0.0412	0.9933
364.09	Y = 25.86X + 0.0068	0.9495

Chapter 3.

Table S2. Parameters of the Thermo Fisher Q-Exactive Plus hybrid quadrupole orbitrap mass spectrometer used for Full MS/dd-MS^2 analysis.

Properties of Full MS/dd-MS^2	
General	
Runtime	0 to 12.5 min
Polarity	Positive
Default Charge	1
Inclusion	-
Exclusion	On
Full MS	
Resolution	70,000
AGC target	1 x 10^6
Scan range	70 to 1050 *m/z*
Maximum IT	246 ms
dd-MS^2	
Resolution	17,500
AGC target	2 x 10^5

Maximum IT	54 ms
Loop count	5
TopN	5
Isolation window	1.0 *m/z*
Fixed mass	-
(N)CE/stepped	NCE: 20, 40, 60
dd Settings	
Minimum AGC	8.00e3
Peptide match	Preferred
Exclude isotopes	on
Dynamic exclusion	10.0 s
ESI Ion Source	
ID	HESI
Sheath gas flow rate	35
Auxiliary gas flow rate	10
Sweep gas flow rate	0
Spray voltage	3.80 kV
S-lens RF level	50 V
Capillary temperature	320 ℃
Auxiliary gas temperature	350 ℃

Table S3. GNPS parameters used for annotation.

GNPS Search Single Spectrum	
Search Options	
Find Related Datasets	Do it
Select Databases to Search	All
Parent Mass Tolerance	0.02 Da

Ion Tolerance	0.02 Da
Min Matched Peaks	4
Score Threshold	0.7
Advanced Search Options	
Library Class	Bronze
Search Analogs	Do Search
Search Unclustered Data	Don’t Search
Top Hit Per spectrum	5
Maximum Analog Search Mass Difference	500.0
Advanced Filtering Options	
Filter StdDev Intensity	0.0
Minimum Peak Intensity	0.0
Min Peak Int	0.0
Filter Precursor Window	Filter
Filter Library	Filter Library
Filter peaks in 50 Da Window	Filter

Table S4. Metabolites differing between cell groups as determined by ANOVA (p-value <0.05, FDR-corrected)

m/z	Annotation	p value	FDR-corrected p value
267.0620	N/A	1.66E-10	4.34E-09
302.1440	N/A	0.001722	0.011115
322.885	N/A	2.01E-27	5.66E-24
359.0250	N/A	6.65E-16	3.99E-14
429.9390	N/A	0.001033	0.007073
431.9630	N/A	0.000185	0.001564
515.2590	N/A	0.005041	0.026922
523.2850	N/A	0.00346	0.019204
537.3000	N/A	1.60E-06	2.15E-05
665.3820	N/A	0.010602	0.048378
756.5470	PC(34:3) or LPC(34:4) or PC(O-34:4) (Library match to 1-Oleoyl-2-palmitoyl-sn-glycero-3-phosphocholine (PC 34:1)) (*)	0.000168	0.001429
768.583	$[PC(P\text{-}20:0/14:0)+Na]^+$ (**)	0.000742	0.005306
780.5460	$[PC(16:0/18:2)+Na]^+$ (**)	2.59E-07	4.06E-06
782.5630	$[PC(16:0/18:1)+Na]^+$ (**)	9.58E-08	1.63E-06
808.5770	$[PC(18:1/18:1)+Na]^+$ (**)	2.57E-06	3.31E-05
810.5940	$[PC(18:0/18:1)+Na]^+$ (**)	0.000114	0.001031

(*)*Features were annotated by GNPS (cosine score = 0.92; number of shared peaks = 5; mass difference to library reference =4.03) and supported by the annotated spectrum in Figure 4b.*

(**) *Features were annotated manually and supported by the annotated spectra in the Figure S4-S6.*

N/A: Metabolites were not annotatable.

Chapter 4.

Table S1. Summary of the groups of cells used in the SCMS experiments.

Cell Lines	Batch	Treatment Condition*	Analyzed Cells
WM115	1	Control	13
		Treatment	18
	2	Control	26
		Treatment	18
WM266-4	3	Control	32
		Treatment	30
	4	Control	29
		Treatment	37

* 1 μM Vemurafenib was used treat cells for 48 h in the treatment groups.

Table S2. Subpopulational biomarkers between subpopulation 1 and 2 in WM115.

m/z	*RSD*	Identification	PPM	$P_{post\ hoc}$*
189.987	128.1056			0.03309
192.039	123.7538			0.012697
203.052	103.7025			5.50E-05
225.034	129.3706			0.01681
296.065	150.745			9.37E-05
341.012	176.1595			0.000441
354.077	128.0285			0.040612
383.115	137.969			0.000359
405.097	173.8225			0.008092
589.478	83.80356			9.45E-08
605.452	116.7758			8.01E-10
615.493	76.47161			8.92E-07
617.509	73.18834			5.66E-06
631.467	108.898			8.01E-10
633.483	93.51578			9.28E-10
641.509	84.88917			0.000501
643.524	75.0312	$[DG(36:2) + Na]^+$ †	4	0.000169
657.483	116.3986			8.01E-10
659.498	98.13423			9.15E-10
700.486	95.96191			8.01E-10
721.554	186.793			0.000521
723.491	74.77151			7.04E-06
726.501	71.44518			8.01E-10
728.518	56.08359	$[PC(30:0) + Na]^+$ †	2	1.70E-06
740.553	100.734	$[PE(O-35:1) + Na]^+$ †	4	8.01E-10
742.475	109.1735			8.01E-10
742.533	80.06013			8.43E-10
742.569	89.43842			8.43E-10
744.491	79.16645			9.53E-10
752.517	61.77599			1.01E-08
754.534	50.81652	$[PC(32:1) + Na]^+$ †‡	2	1.88E-05
756.549	51.33026			0.000429
766.569	83.4998	$[PE(O-37:2) + Na]^+$ †	4	3.97E-07
768.49	92.68474			8.01E-10
768.549	76.8444			0.00706
768.585	47.3431	$[PE(P-37:0) + Na]^+$ †	3	0.002989
770.507	69.87939			1.01E-08
772.523	70.82742			7.45E-07
776.516	96.64662			8.01E-10

778.533	62.08769	[PC(34:3) + Na]$^+$ †	3	1.23E-07
780.55	50.97458	[PC(34:2) + Na]$^+$ †	1	0.000145
782.566	50.84661	[PC(34:1) + Na]$^+$ †	1	1.05E-05
784.522	111.4313			8.01E-10
788.516	100.5926			0.007988
790.568	66.30461			1.05E-09
794.506	99.14211			8.01E-10
794.564	74.30683			1.43E-06
794.601	130.933			0.000428
796.523	64.26495	[PC(34:2) + K]$^+$ †	2	2.51E-08
796.58	76.08471			8.81E-07
798.539	76.09119			4.37E-09
804.549	51.08599	[PC(36:4) + Na]$^+$ †	2	0.00061
806.565	55.84285			0.010579
808.582	49.38926	[PC(36:2) + Na]$^+$ †‡	0	0.008852
810.597	46.10142	[PC(36:1) + Na]$^+$ †	1	0.00692
816.585	61.71127			5.00E-07
818.601	102.5192			8.01E-10
820.522	75.10244	[PE(39:4) + K]$^+$ †	4	9.79E-10
822.539	70.32211	[PC(36:3) + K]$^+$ †	2	7.34E-09
824.554	66.77384	[PC(36:2) + K]$^+$ †	3	4.27E-08
825.691	73.80641			1.50E-07
826.571	101.7181			8.01E-10
828.71	89.96173			3.93E-09
830.565	62.75414			2.83E-05
832.58	53.71502	[PC(38:4) + Na]$^+$ †	3	0.001517
834.597	77.88288	[PC(38:3) + Na]$^+$ †	1	1.08E-09
836.613	114.3903			0.000186
841.665	100.8033			8.01E-10
843.681	93.34589			9.53E-10
846.539	79.29715			8.01E-10
848.554	82.36365			8.01E-10
851.707	69.3612			8.12E-06
853.722	50.85418	[TG(48:6) + H]$^+$ ‡	4	0.002183
856.741	73.06928			4.73E-07
858.596	85.44335			5.34E-09
867.681	90.26346			8.01E-10
869.697	80.84171			4.88E-09
871.713	92.1332			1.95E-09
877.722	71.98826			0.003149
879.738	53.06125			0.043587
881.754	49.77383			0.01081
893.696	85.14766			1.61E-09
895.712	73.01709			1.22E-07

897.728	75.97223			1.25E-07
899.744	124.2535			8.01E-10
909.786	101.0202			0.001135
919.713	87.96139			4.77E-08
921.728	71.15654			5.35E-07
923.744	74.74833			1.09E-07
925.76	112.0745			8.01E-10
947.744	114.6453			3.02E-09

*FDR adjusted *p*-value from *post hoc* pairwise comparison between subpopulation 1 and 2 under a familywise error rate.

†Biomarker identified at the population level.

‡Biomarker identified at the single cell level.

PC = phosphatidylcholine, PE = phosphatidylethanolamine, DG = diglyceride, TG = triglyceride.

Table S3. Subpopulational biomarkers between subpopulation 1 and 2 in WM266-4.

m/z	*RSD*	Identification	PPM	$P_{post\ hoc}$*
174.013	159.4572			0.00298
176.065	184.2156			0.001055
184.073	54.73049			2.97E-10
189.987	159.1209			0.030178
203.052	163.2219			0.000611
219.026	134.2137			0.036753
226.95	134.136			0.045047
354.076	219.6756			0.005098
383.115	202.9088			0.001485
650.434	111.3089			1.44E-07
672.416	130.9384			0.005258
678.501	99.25205			2.97E-10
692.553	88.21998			3.05E-10
703.573	159.5482			4.07E-08
704.516	77.16659			2.97E-10
706.534	80.57585	$[PC(30:0) + H]^+$ †	5	2.97E-10
708.538	107.4086			2.97E-10
718.568	74.11582			2.97E-10
720.547	90.48607			3.37E-10
720.586	105.4016			2.97E-10
725.55	207.105			0.000322
730.531	90.67068			4.43E-09
730.544	102.242			2.97E-10
731.599	131.3111			1.97E-05
732.55	76.242	$[PE(35:1) + H]^+$ †‡	5	2.97E-10
734.566	80.08571			2.97E-10

742.566	106.06			0.01014
744.546	117.12			4.40E-10
744.584	73.40015			2.97E-10
746.562	65.493			3.80E-10
746.579	86.20477			2.97E-10
746.602	82.15653			2.97E-10
748.616	101.1125			3.05E-10
758.566	63.44769	$[PE(37:2) + H]^+$ †	4	2.97E-10
760.582	65.28295	$[PC(34:1) + H]^+$ †	4	2.97E-10
762.584	66.62915			8.37E-08
762.596	78.46355			1.17E-08
770.599	54.68057			2.97E-10
772.577	83.68257			2.97E-10
772.615	71.29696			3.02E-10
774.593	84.97327			2.97E-10
774.631	96.38335			2.97E-10
784.582	74.77287			2.97E-10
786.597	67.40736	$[PE(39:2) + H]^+$ †	4	2.97E-10
794.612	116.6464			1.35E-06
796.614	69.19304			2.97E-10
811.661	141.1078			0.000206
812.609	106.9853			1.00E-06
813.677	151.3288			0.001812
814.625	91.72509			2.97E-10
830.545	132.5015			0.00117
834.593	103.2547	$[PC(38:3) + Na]^+$ †	6	0.032411
1464.086	120.3208			2.97E-10
1466.101	112.6823			2.97E-10
1478.138	125.9171			2.97E-10
1480.153	131.1825			2.97E-10
1490.102	109.0322			2.97E-10
1492.117	101.9152			2.97E-10
1504.153	120.7291			2.97E-10
1506.168	119.1866			2.97E-10
1516.117	104.9038			2.97E-10
1518.132	99.1318			2.97E-10
1520.147	104.2193			2.97E-10
1542.133	104.062			5.47E-10
1544.148	101.6704			2.97E-10
1546.163	106.3662			2.97E-10
1570.164	119.6729			2.97E-10

*FDR adjusted *p*-value from *post hoc* pairwise comparison between subpopulation 1 and 2 under a familywise error rate.

†Biomarker identified at the population level.

‡Biomarker identified at the single cell level.

PC = phosphatidylcholine, PE = phosphatidylethanolamine, DG = diglyceride, TG = triglyceride.